Early Cretaceous continental arc magmatism in the Wakhan Corridor, South Pamir: mantle evolution and geodynamic processes during flat subduction of the Neo-Tethys oceanic slab

Fan Yang[1, 2], Jiyuan Yin [2*], Wenjiao Xiao [3], Mike Fowler [4], Andrew C. Kerr [5], Zaili Tao [2], Wen Chen [2], Yuelong Chen[1]

[1] School of Earth Sciences and Resources, China University of Geosciences, Beijing, 100083, China

[2] Institute of Geology, Chinese Academy of Geological Sciences, Beijing 100037, China

[3] Xinjiang Institute of Ecology and Geography, Chinese Academy of Sciences, Urumqi, 830011, China

[4] School of the Environment, Geography and Geosciences, University of Portsmouth, Burnaby Building, Burnaby Road, Portsmouth PO1 3QL, UK

[5] School of Earth and Environmental Sciences, Cardiff University, Cardiff, Wales CF10 3AT, United Kingdom

***Corresponding authors:**

Email: yinjiyuan1983@163.com (J. Yin)

ABSTRACT

The petrogenesis of continental arc magmas provide critical insights into thermal evolution and geodynamics of the continental lithosphere and crust-mantle interaction and deep dynamic processes. In this study, we report new zircon U-Pb ages along with isotopic and elemental whole-rock geochemistry, mineral chemistry and Hf-O isotope data, for Kalaqigu diorites and monzogranites in the Chinese Wakhan Corridor, South Pamir. Zircon U-Pb dating indicates that the Kalaqigu pluton was emplaced in the Early Cretaceous (ca. 108–106 Ma). The diorites are geochemically characterized by low SiO_2 (51.9–54.5 wt.%) and CaO (7.7–9.4 wt.%) contents, but high MgO (5.3–8.3 wt.%), Al_2O_3 (12.8–16.8 wt.%) and TiO_2 (0.6–1.1 wt.%) contents as well as high $Mg^{\#}$ (56–65) values, and so are similar to high-Mg diorites. They are enriched in large ion lithophile elements (LILEs, e.g., K, Sr and Ba) and light rare earth elements (LREEs), while depleted in high field strength elements (HFSEs, i.e., Nb, Ta, Zr and Hf). Combined with negative $\varepsilon_{Nd}(t)$ (-6.9 to -14.0), $\varepsilon_{Hf}(t)$ (-9.9 to -12.2) and high $(^{87}Sr/^{86}Sr)_i$ (0.7075–0.7086) ratios, these observations indicate they originated from an enriched lithospheric mantle source. High $\delta^{18}O_{zrn}$ (7.49–9.01‰) values in conjunction with relatively high $^{207}Pb/^{206}Pb$ and $^{208}Pb/^{206}Pb$ ratios suggest that the source was modified by subducted sediment-derived melts. Variable Cr contents (54–117 ppm) are likely controlled by minor fractionation of olivine and orthopyroxene. The monzogranites show high SiO_2 contents (69.2–72.0 wt.%), low Rb/Sr (0.4–0.6), $(K_2O+Na_2O)/CaO$ (2.6–4.8) and FeO^T/MgO ratios (2.6–3.2). They contain diagnostic cordierite and show strongly-peraluminous characteristics (A/CNK > 1.1) with high $\delta^{18}O_{zrn}$ (7.82–8.85‰) values, compatible with typical S-type granites. Their abundant inherited zircons, with age populations similar to those of detrital zircons from regional Early Paleozoic metasedimentary rocks, indicate they were derived from partial melting of ancient metasedimentary rocks. Phase equilibrium modelling is consistent with biotite-dehydration melting of metagreywacke, probably at ~750 ℃ and ~6.0 kbar indicated by the biotite chemistry. A south-to-north magmatic migration based on regional geochronology suggests that northward flat-slab subduction of the Neo-Tethys oceanic slab played an important role in the generation of these

widespread Early Cretaceous continental arc magmatic rocks. However, the granitoids were generated earlier than the mantle-derived mafic rocks, which suggests that crustal melting occurred during the early stage of subduction. The subsequent flat subduction resulted in continuous metasomatism by subducted sediments. Contemporaneous regional compression primarily occurred far north of the subduction zone (i.e., North and Central Pamir), inducing deformation as well as crustal shortening. With the flare-up of continental arc magmatism in South Pamir, crustal shortening moved southward. These processes, combined with addition of voluminous mantle-derived magmas, played an important role in crustal thickening in the Pamir during the Early Cretaceous.

INTRODUCTION

Andean-type continental arcs, where the oceanic crust subducts beneath an active continental margin, serve as ideal natural laboratories for studying destructive plate margin processes and the geodynamic evolution of the Earth's crust and mantle (e.g., Rudnick and Gao, 2003; Davidson and Arculus, 2006; Jagoutz and Schmidt, 2012). Consequently, the formation and evolution of Andean-type continental arcs is a topic of considerable interest in earth sciences (e.g., Ducea et al., 2015; Suo et al., 2019; Qin et al., 2022). As a result of the subduction of oceanic slabs, continental arcs generally have undergone intense mantle metasomatism and crust-mantle interaction, resulting in arc-related igneous suites ranging in compositions from mafic to felsic (e.g., Dhuime et al., 2012; Ducea et al., 2015; Cashman et al., 2017; Tang et al., 2019; Xiao et al., 2022). A major focus is the spatiotemporal and petrogenetic connections between the high-Mg basic to intermediate rocks generated from a modified mantle and the coeval felsic granitoids (Castro, 2019). For instance, I-type granites within "Cordilleran" batholiths can represent fractionated liquids from intermediate magma systems of broadly high-Mg andesitic composition (e.g., Castro et al., 2010), while sanukitoid magmas can act as water donors that trigger extensive melting of the lower crust to also generate granitoids, for example from "Cimmerian" batholiths of Iberia (e.g., Pereira et al., 2015). Subduction processes within continental arc systems are invariably complicated, and may include flat-slab subduction (e.g., Zhang et al., 2022), slab rollback (e.g., Ma et al., 2013; Lei et al., 2023) or oceanic ridge subduction (e.g., Zhu et al., 2019; Ma et al., 2022). The geochemical characteristics of contemporaneous subduction-related magmatism (Rudnick and Gao, 2003; Zhu et al., 2019; Qi et al., 2023) reflect this range of processes (e.g., Gianni and Luján, 2021; Ma et al., 2023). Therefore, ancient subduction-related arc magmatism contains key information for understanding the characteristics of subduction.

The South Pamir experienced northward subduction of the Neo-Tethys Ocean from the Shyok suture (e.g., Schwab et al., 2004; Faisal et al., 2016; Chapman et al., 2018a), and is regarded as a preeminent natural laboratory for studying oceanic subduction geodynamics and Andean-style orogenesis. Subduction-related rocks in South Pamir are important components (e.g., Faisal et al., 2016; Aminov et al., 2017; Zhang et al., 2022), and led to the formation of a typical continental arc (e.g., Schwab et al., 2004). The Wakhan Corridor (located within Karakorum Batholith, South Pamir) preserves complete continental arc-related magmatic sequence, including mafic igneous rocks (e.g., basalt, andesite, diorite) with granitoids (e.g., granodiorite and monzogranite) (Jiang et al., 2014; Li et al., 2016; Liu et al., 2019; Zhang et al., 2022). Their field relations, age distribution, petrology and geochemistry provided valuable information for understanding Neo-Tethys subduction. Based on the distance (ca. 200 km) from the Shyok suture to the South Pamir batholith, as well as the Early Cretaceous active shortening of the Pamir (Robinson, 2015), Cretaceous low-angle flat subduction of the Neo-Tethys oceanic slab has been proposed (e.g., Chapman et al., 2018a; Zhang et al., 2022). Although many studies have been devoted to the magmatic rocks of the Wakhan Corridor, their origin is still controversial. In particular, the processes of mantle metasomatism derived from Neo-Tethys slab subduction are still unclear, as is the petrogenesis and evolution of related crust-derived magmas.

In this paper, we present new U-Pb geochronological, geochemical, and Sr-Nd-Pb-Hf-O isotope data from the Cretaceous diorites and monzogranites of the Kalaqigu pluton, east of Wakhan Corridor. Our primary focus is to investigate their petrogenesis and elucidate their tectonic setting. By integrating the new results with existing data from the Wakhan Corridor, we aim to further constrain the geodynamic processes of Neo-Tethys subduction during the Cretaceous and contribute to the global understanding of continental arc magmatism.

GEOLOGICAL SETTING AND SAMPLING

Geological Setting

The Pamir, which borders the Tianshan, Tarim Basin and Tibetan Plateau, has undergone prolonged processes of accretion, collision, and suturing during the Early Paleozoic-Mesozoic (Fig. 1a; e.g., Tapponnier et al., 1981; Robinson et al., 2012; Robinson, 2015). The Cenozoic collision between the Indian and Asian continents resulted in further deformation, structural overprinting, and tectonic uplift of Pamir, forming its remarkable present-day configuration (e.g., Yin and Harrison, 2000; Liu et al., 2017; Rutte et al., 2017). Geologically, the Pamir region can be divided into three tectonic units, from north to south: North Pamir, Central Pamir and South Pamir, separated by Paleozoic and Mesozoic sutures (Fig. 1b; Burtman and Molnar, 1993; Angiolini et al., 2013; Robinson, 2015). The North Pamir represents a Paleozoic accretionary complex (Schwab et al., 2004; Robinson et al., 2012), while the Central Pamir and South Pamir are believed to have rifted from the northern margin of Gondwana during the Late Carboniferous to Early Permian (Burtman and Molnar, 1993; Angiolini et al., 2013; Robinson, 2015).

The North Pamir contains abundant Paleozoic and Permo-Triassic magmatic rocks (Fig. 1b; Chapman et al., 2018a), while Central Pamir hosts mainly Cenozoic plutons, with a few of Cretaceous age (Fig. 1b; Robinson, 2015; Chapman et al., 2018a; Ma et al., 2023). The South Pamir can be further divided into southwest Pamir and Karakoram terrane, separated by a system of Cenozoic extensional detachments (Fig. 1b; Schwab et al., 2004; Schmidt et al., 2011; Angiolini et al., 2013). The southwest Pamir, which continues into the Hindu Kush mountain range, consists of Precambrian basement domes and records a complex history of later magmatism spanning from the Early Paleozoic to the present day (Schmidt et al., 2011; Faisal et al., 2016; Soret et al., 2019). In the southeast Pamir, Permian to Cretaceous sedimentary sequences dominate, accompanied by highly deformed and metamorphosed Precambrian basement (Zanchetta et al., 2018; Zhang et al., 2018; Imrecke et al., 2019). In addition to this, widespread Early Cretaceous magmatic rocks are observed in the South Pamir. This magmatic suite is dominated by S-type and I-type granitoids in addition to a small amount of intermediate-silicic volcanic rocks (e.g., Faisal et al., 2016; Aminov et al., 2017; Ma et al., 2023), with a notable high-flux magmatic event occurring between 110 and 105 Ma (Fig. 1b; Schwab et al., 2004; Heuberger et al., 2007; Chapman et al., 2018a). These Cretaceous magmatic rocks provide important insights into Mesozoic subduction of the Neo-Tethys Ocean and the crust-mantle interaction (Ravikant et al., 2009; Zhang et al., 2022). To the south, the Kohistan-Ladakh Arc, situated between the Shyok Suture (SSZ) and the Indus-Tsangpo Suture Zone (ITSZ), developed during the Mesozoic above a north-dipping subduction zone within the Neo-Tethys Ocean (Fig. 1b; Schwab et al., 2004; Ravikant et al., 2009; Jagoutz and Schmidt, 2012; Chapman et al., 2018a).

The diorites and monzogranites investigated in this study are exposed in the Kalaqigu pluton located in the Chinese Wakhan Corridor, which is part of the South Pamir (Figs. 1b–1c). The basement of the Wakhan Corridor comprises the Archean (ca. 2.5 Ga) Mazar complex. This was intruded by ca. 840 Ma granites and 500–490 Ma mafic rocks as well as Early Cretaceous mafic-to-acidic intrusions (Ji et al., 2011; Li et al., 2016; Zhang et al., 2018; Zhang et al., 2022). As a result of Neo-Tethys oceanic subduction, these Cretaceous magmatic rocks have formed complete volcanic sequences related to arc activity, creating an east-west trending magmatic belt along the Wakhan Corridor (Li et al., 2016; Liu et al., 2020; Zhang et al., 2022). Jiang et al. (2014) first reported the granodiorite and monzogranites of the Kalaqigu pluton and suggested that they were generated by partial melting of metasedimentary basement. They also reported that a mafic basalt-andesite sequence with enriched Nd isotope compositions (-5.9 to -9.6) (Zhang et al., 2022) and dioritic enclaves with $\varepsilon_{Nd}(t)$ of ca. -4.74 (Liu et al., 2020) erupted at 104-98 Ma in the west of the studied area. These originated from metasomatized sub-continental lithospheric mantle and underwent variable assimilation fractional crystallization. I-type granitoids generated by crust-mantle interaction are also reported from the Wakhan Corridor (Liu et al., 2020). Additionally, in the northwest of the Wakhan Corridor, the contemporaneous (110–92 Ma) Teshiktash-Beik volcanic basin consists of grey and reddish lavas, tuffaceous lavas, and dacitic tuff breccias (Fig. 1b; Aminov et al., 2017). To the north, S-type granites were emplaced in the Taxkorgan pluton, in the northeastern part of the continental arc (Fig. 1b; Jiang et al., 2014; Ma et al., 2023).

In the field, the Kalaqigu pluton intrudes Paleozoic and Jurassic strata and is adjacent to the Hongqilapu pluton (Fig. 1c). Granitoids derived from crust-mantle mixing as well as mantle-derived dioritic dikes have also been identified in the Hongqilapu pluton (Jiang et al., 2014; Li et al., 2016).

Sampling and Description

Diorite and monzogranite were collected from the Kalaqigu pluton in the Chinese part of the Wakhan Corridor, Southern Pamir, as indicated in Figure 1c. The diorite exhibites a medium-fine grained subhedral granular structure and is primarily composed of plagioclase (60 vol.%), amphibole (25 vol.%), biotite (10 vol.%), and quartz (1–5 vol.%), with accessory minerals such as apatite and zircon (Figs. 2a–2b). The biotite shows partial replacement by chlorite (Fig. 2b).The monzogranite exhibits a fined-grained or porphyritic texture and is composed of K-feldspar (35 vol.%), plagioclase (30 vol.%), quartz (25 vol.%), biotite (1–5 vol.%), cordierite (1 vol.%) and sillimanite (< 1 vol.%), with minor amounts of apatite and zircon within the matrix (Figs. 2c–2d). Partially enclosed K-feldspar gains contain small biotite inclusions (Figs. 2c–2d). Metasomatic worm-like structures can be observed at the contacts between plagioclase and K-feldspar and sillimanite appear as small needles predomnantly embedded in the K-feldspar. Cordierite is pseudomorphed by serpentine (Fig. 2d).

ANALYTICAL METHODS

Detailed analytical methods are given in Supplementary File 1 and a short summary is given here. Zircon U-Pb dating using LA-ICP-MS and in-situ zircon Lu-Hf isotopes were analyzed at the Institute of Geology and Geophysics, Chinese Academy of Sciences (IGG CAS). Zircon oxygen isotopes were determined by secondary ion mass spectrometer (SIMS) at the at State Key Laboratory of Isotope Geochemistry (SKLaBIG), Guangzhou Institute of Geochemistry, Chinese Academy of Sciences (GIG CAS). Major elements analyses of amphibole, plagioclase and biotite were carried out using JEOL JXA-8100 Electron Probe Micro Analyzer (EPMA) at IGG CAS. Major element contents were determined by X-ray fluorescence spectrometer (XRF) on fused glass beads at SKLaBIG, GIG CAS. Trace element analyses were determined using a Perkin-Elmer ELAN-DRC-e inductively coupled plasma mass spectrometer at the State Key Laboratory of Ore Deposit Geochemistry (SKLOG). Whole-rock Sr-Nd-Pb isotopes were determined using a MC-ICP-MS at SKLaBIG, GIG CAS.

RESULTS

Zircons were separated from two samples for LA-ICP-MS zircon U-Pb dating. Whole-rock major and trace elements and Sr-Nd-Pb isotopes, zircon U-Pb-Hf-O isotopic compositions as well as analysis of mineral compositions are provided in the Supplementary Table 1-5.

Zircon U-Pb Ages

All zircon crystals from Kalaqigu diorite and monzogranite are generally transparent and colorless, with length/width ratios ranging from 4:1 to 1:1 (Fig. 3). They exhibit well-developed concentric oscillatory zoning in cathodoluminescence (CL) images (Fig. 3) and high Th/U ratios (typically > 0.2; Supplementary Table 1), indicating a magmatic origin (Belousova et al., 2002). A few zircon grains from the monzogranite display a clear core-rim structure in CL images (Fig. 3d). Eighteen analytical spots from the diorite yielded concordant $^{206}Pb/^{238}U$ ages ranging from 103 to 109 Ma, with a weighted mean age of 105.9 ± 0.3 Ma (MSWD = 0.93) (Fig. 3a). Dating of monzogranite was conducted on the zircon rims and cores (Figs. 3b–3d).

The zircon rims yield $^{206}Pb/^{238}U$ ages ranging from 106 to 120 Ma, with weighted mean ages of 108.4 ± 0.4 Ma (n = 7, MSWD = 0.59) (Fig. 3b). These ages indicate that Kalaqigu pluton was emplaced during the Early Cretaceous (108–105 Ma). Ages for the inherited zircon cores from the monzogranite exhibit a wide range, from 1032 to 334 Ma (Supplementary Table 1; Figs. 3c–3d).

Mineral Chemistry

Amphibole is the dominant mafic mineral in the Kalaqigu diorites but is absent from the monzogranite. Based on the classification by Leake et al. (1997), these belong to the calcic subgroup (Ca_B = 1.83–1.92 and $(Na + K)_A$ = 0.33–0.59) with high $Mg^{\#}$ values (52–62). Amphibole phenocrysts from WK1616 that yield $(Na + K)_A < 0.5$ based on amphibole classification diagrams classify as magnesio-hornblende (Fig. 4a, Leake et al., 1997; Hawthorne and Oberti, 2007). The amphibole phenocrysts with higher content of alkaline elements ($(Na + K)_A \geq 0.5$) classify as magnesio-hastingsite ($^{VI}Al < Fe^{3+}$) and pargasite ($^{VI}Al > Fe^{3+}$) (Fig. 4b). Only one amphibole has a high content of Si (> 6.5) and classifies as edenite (Fig. 4b). To estimate the temperature and pressure of amphibole crystallization, we used the formulas from Ridolfi et al. (2010) and the empirical geobarometer from Krawczynski et al. (2012). Calculated temperatures and pressures for these amphibole grains range from 771–907 °C and 3.26–7.43 kbar with average of 849 °C and 5.16 kbar, respectively (Supplementary Table 2). We also calculated the H_2O_{melt} contents (5.19–6.86 wt.%) and oxygen fugacity ($\triangle$FMQ = 0.45–1.89) using the formulas from Ridolfi et al. (2010).

Biotite from the diorites is mainly Mg-biotite, with relatively high concentrations of SiO_2 (37.3–37.4 wt.%), MgO (12.2–12.5 wt.%) and $Mg^{\#}$ (55), as well as low Al_2O_3 (14.1–14.5 wt.%), FeO^T (17.8–18.0 wt.%) and TiO_2 (3.73–3.85 wt.%) (Fig. 4c, Supplementary Table 2). In the monzogranite, biotite is Fe-biotite with lower SiO_2 (34.4–35.4 wt.%), MgO (6.66–7.37 wt.%) and $Mg^{\#}$ (36–40), as well as high Al_2O_3 (18.5–19.2 wt.%), FeO^T (20.0–21.2 wt.%) and TiO_2 (3.65–4.02 wt.%) (Fig. 4c, Supplementary Table 2) than the biotite in the diorites. Calculated temperature and pressure values of biotite from diorites show a range of 770–783 °C and 4.56–5.32

kbar, whereas those of biotite from monzogranites have a range of 746–772 °C and 5.50–6.42 kbar (Li and Zhang, 2022; Supplementary Table 2), representing the crystallization T and P of biotites.

Representative plagioclase grains were analyzed from core to rim (Figs. 4b–4c). For diorite (WK1616), plagioclase grains typically show a decrease in modal anorthite (An) from core to rim (Fig. 4d; Supplementary Table 2). These grains generally have a core of $An_{80-85}Ab_{15-20}Or_{0-1}$ and a rim of $An_{45-50}Ab_{45-55}Or_{1-2}$. This indicates that plagioclase crystallized from bytownite, through labradorite to andesine from early to later stages (Fig. 4d). Plagioclase compositions in monzogranite (WK1617) vary between An_{22}–An_{35} and classify as oligoclase-andesine (Fig. 4d).

Major and Trace Element Geochemistry

Diorites

The diorites are characterized by low SiO_2 (51.9–54.5 wt.%) (Fig. 5a), high MgO (5.4–8.3 wt.%), and $Fe_2O_3^T$ (8.1–9.5 wt.%) contents with high $Mg^{\#}$ (56–65) values. They have relatively high alkalis ($K_2O + Na_2O$ = 4.31–5.35 wt.%) and K_2O/Na_2O (0.9–1.3) ratios, showing high-K calc-alkaline to shoshonite (Fig. 5b) and potassic features (Fig. 5c). In addition, they exhibit high Al_2O_3 (12.8–16.8 wt.%) and CaO (7.73–9.35 wt.%) contents, plotting in metaluminous field (A/CNK = 0.6–0.8).

On chondrite-normalized rare earth element (REE) diagrams (Fig. 6a), the diorites show sub-parallel light-REE enriched patterns with relatively flat heavy REEs ($(La/Yb)_N$ = 6.4–12.1; $(Gd/Yb)_N$ = 1.7–2.3), with weak negative Eu anomalies [Eu/Eu* $(\mathrm{Eu_N}/\sqrt[2]{\mathrm{Sm_N} \times \mathrm{Gd_N}})$ = 0.77–0.88]. On a primitive mantle normalized diagram, they are enriched in LILEs (K, Sr and Ba) but depleted in HFSEs and show negative Nb, Ta, P, Zr, Hf, and Ti anomalies (Fig. 6b). The diorite samples are characterized by high Sr (365–607 ppm) and Y (20.9–25.8 ppm) contents with low Sr/Y (17–27) ratios. In addition, they have high Cr (54.6–117.2 ppm), Co (18.6–33.7 ppm), and Ni (7.84–34.6 ppm) contents.

Monzogranites

The monzogranites have relatively silicic compositions (SiO_2 = 69.2–72.0 wt.%) (Fig. 5a). They are characterized by low $Fe_2O_3^T$ (1.8–2.9 wt.%), MgO (0.6–1.0 wt.%; $Mg^{\#}$ = 36–40), CaO (1.6–2.6 wt.%), as well as high Al_2O_3 (14.4–16.2 wt.%) and alkalis (K_2O + Na_2O = 6.8–7.7 wt.%) contents. They show calc-alkaline to high-K calc-alkaline (Fig. 5b), potassic (Fig. 5c) and peraluminous (A/CNK = 1.15–1.23) features (Fig. 5d).

The monzogranites show steeply fractionated REE patterns (Fig. 6c), with marked enrichment in LREEs and steep HREEs ($(La/Yb)_N$ = 41.4–60.7; $(Gd/Yb)_N$ = 6.0–7.2), plus moderate negative Eu anomalies (Eu/Eu* = 0.67–0.83). On a primitive mantle normalized diagram, they also show enrichment in LILEs (such as Th, Rb, U, and K) relative to HFSEs and LREEs, with negative Ba, Nb, Ta, Sr, P, and Ti anomalies (Fig. 6d). The monzogranite samples have relatively low Sr (205–293 ppm) and Y contents (9.1–10.2 ppm) with Sr/Y ratios of 24 to 30. In addition, they exhibit low Cr (2.17–2.91 ppm), Co (1.68–2.87 ppm), and Ni (0.83–1.47 ppm) contents.

Whole-rock Sr-Nd-Pb Isotopes

Initial Sr-Nd-Pb isotopic values were calculated at the relevant crystallization age (106 or 108 Ma). The Kalaqigu diorites have initial $^{87}Sr/^{86}Sr$ isotopic ratios of 0.7075 to 0.7086 and $\varepsilon_{Nd}(t)$ values of -5.97 to -7.18 with old Nd model ages (T_{DM} = ca. 1491–1592 Ga) (Fig. 7a). The studied monzogranites exhibit $\varepsilon_{Nd}(t)$ values (-12.3 to -12.5) with two-stage model ages of 1909 to 1921 Ma and initial $^{87}Sr/^{86}Sr$ isotopic ratios (0.7154–0.7158), but these differ significantly from those of the diorites (Fig. 7a). The diorites and monzogranites have similar $(^{206}Pb/^{204}Pb)_i$ ratios (18.64–18.68 in diorites and 18.66–18.67 in monzogranites) but different $(^{207}Pb/^{204}Pb)_i$ (15.70–15.71 and 15.757–15.758, respectively) and $(^{206}Pb/^{204}Pb)_i$ ratios (39.02–39.12 and 39.14–39.16, respectively) relative to the Northern Hemisphere Reference Line (NHRL) (Figs. 7b–7c).

Zircon Hf-O Isotopic Compositions

The zircons from the Kalaqigu diorites (WK1616) have negative $\varepsilon_{Hf}(t)$ values ranging from -9.9 to -12.2 (-10.9 on average) and old T_{DM2} (1.79–1.93 Ga and 1.85 Ga on average) ages (Supplementary Table 4). The Kalaqigu diorites (WK1616) and monzogranites (WK1617) have similar $\delta^{18}O$ values (i.e., 7.49–9.01‰ and 7.82–8.85‰, respectively; Supplementary Table 5), which are higher than those (5.3 ± 0.6‰, 2SD) of igneous-origin zircons in equilibrium with mantle-derived magmas (Fig. 8; Valley, 2003).

DISCUSSION

Geochemical Affinities

The Kalaqigu diorites exhibit high MgO, Al_2O_3 and TiO_2 contents, but low FeO^T/MgO ratios (1.0–1.4) and CaO contents, thus showing geochemical affinities to high-Mg andesites (HMAs; Tatsumi, 2001). In addition, they have low Sr (365–607 ppm), Y (20.9–25.8 ppm) and Yb contents (1.9–2.5 ppm) with low Sr/Y (17–27) and $(La/Yb)_N$ ratios (11–15), which are compositionally analogous to those of sanukite from the Setouchi Volcanic Belt (Figs. 9a–9b; Yogodzinski et al., 1994; Shimoda et al., 1998; Tatsumi, 2001). Their high $Mg^{\#}$ values and Cr contents also suggest that they are sanukitic HMAs (Kamei et al., 2004; Martin et al., 2005).

Granites are often categorized as S-, I-, or A-types (Chappell and White, 1974; Loiselle and Wones, 1979; Whalen et al., 1987). The monzogranites from the Kalaqigu pluton are hornblende-free and characterized by high SiO_2, low Rb/Sr, $(K_2O+Na_2O)/CaO$ (2.6–4.8) and FeO^T/MgO ratios (2.6–3.2), implying that they are unfractionated granites (Chappell and White, 1974, 1992). They have low 10000 × Ga/Al ratios (2.1–2.6) and (Zr + Nb + Ce + Y) contents (199–257) and low zircon saturation temperatures (761–824°C), which are distinct from those of A-type granites (Figs. 9c–9d; Whalen et al., 1987). Their A/CNK values are higher than 1.1 (Fig. 5d), and they contain diagnostic peraluminous minerals such as cordierite (Fig. 2d; Barbarin, 1999). The U-Pb ages of inherited zircon cores from the monzogranite show large variations (Fig. 3c), consistent with typical S-type granitoids (Gao et al., 2016). In addition, they have initial $^{87}Sr/^{86}Sr$ ratios of 0.7154 to 0.7158 and low $\varepsilon_{Nd}(t)$ values of -12.3 to -12.4 (Figs. 7a–7b). These geochemical features strongly indicate that these monzogranites are unfractionated, high-K, S-type granites.

Petrogenesis and Magma Sources

Diorites

AFC effect

As mentioned above, the Kalaqigu diorites show affinities with HMAs. These high-Mg diorites have low SiO_2 contents and high $Mg^{\#}$ values (Fig. 10a) with variable Cr and Ni contents, indicating they are derived from a mantle source. For mantle-derived melts, wall-rock assimilation and shallow-level fractional crystallization are inevitable during transport and emplacement (DePaolo, 1981). Crustal assimilation is likely to cause an increase in $(^{87}Sr/^{86}Sr)_i$ and a decrease in $\varepsilon_{Nd}(t)$ as well as Nb/La and Nb/Th ratios. This is because the continental crust is typically characterized by low $\varepsilon_{Nd}(t)$ values, low Nb/La and Nb/Th ratios, but high $(^{87}Sr/^{86}Sr)_i$ ratios relative to those of the mantle (Rudnick and Fountain, 1995). However, these high-Mg diorites show virtually identical Sr-Nd isotopic compositions (Fig. 7a) and limited variations in Nb/La (0.31–0.42) and Nb/Th (0.64–2.51) ratios as well as zircon $\varepsilon_{Hf}(t)$ values (-12.2 ~ -9.9). These observations suggest that they have undergone limited crustal assimilation.

These high-Mg diorites however, have generally low but variable compatible element contents, such as V, Cr and Ni, indicating some fractionation of mafic minerals. The positive correlation between MgO and $Fe_2O_3^T$ and CaO as well as negative correlation between MgO and Al_2O_3 suggests fractionation of olivine/pyroxene/spinel in a lower magma chamber (Figs. 10b-10d). The negative correlation of MgO and TiO_2 suggests there is no fractionation of Fe-Ti oxides (Fig. 10f). Absence of Eu, Sr and Ba anomalies also suggests that feldspar was probably not a fractioning phase (Figs. 6a–6b). These fractional crystallization trends are consistent with models derived from Rhyolite-MELTS using a pressure of 5.16 kbar and water content of 5.84 wt.% (Supplementary Table 2), as well as a range of oxygen fugacity

(△QFM +1, +2 and +3) (Figs. 10b–10f). The models support minor fractionation of olivine + orthopyroxene +/- clinopyroxene/spinel during magma evolution.

Magma Evolution

Several petrogenetic models have been proposed for the formation of HMAs, including (1) partial melting of a subducted oceanic crust with assimilation of mantle peridotites (Yogodzinski et al., 1994; Kelemen, 1995); (2) partial melting of delaminated mafic crust at mantle depths (Chen et al., 2013); (3) direct partial melting of hydrous mantle (Hirose, 1997; Wood and Turner, 2009; Mitchell and Grove, 2015); (4) interaction of fluids/melts derived from subducted slabs and/or sediments with the overlying mantle wedge (Shimoda et al., 1998; Tatsumi, 2001, 2006).

In general, HMAs generated by models one and two are similar to adakitic and bajaitic HMAs because their trace element characteristics, such as high Sr/Y ratios, absence of Eu anomalies and depletion in HREEs (Kelemen, 1995; Kelemen et al., 2004; Chen et al., 2013), reflect the melting residue of oceanic slab or lower crust. However, the Kalaqigu high-Mg diorites have low Sr/Y ratios (Fig. 9b) with only slight negative Eu anomalies (Fig. 6a) and they are enriched in LREEs with limited depletion in HREEs (Fig. 6b). Coupled with their high Al_2O_3 (12.8–16.8 wt.%), Sc contents (24.5–30.0 ppm) and low Y (20.9–25.8 ppm) and Yb (1.9–2.5 ppm), this geochemical signature suggests a garnet-free source region (Defant and Drummond, 1990; Hoskin and Schaltegger, 2003; Macpherson et al., 2006). Further, it is thought that the crust of South Pamir did not significantly delaminate during the Early Cretaceous (Soret et al., 2019), therefore this also rules out the second model. Accordingly, and given the following observations, we consider that these high-Mg diorites to represent the products of interaction between subducted sedimentary melts and hydrous mantle:

(1) The Kalaqigu high-Mg diorites have low $\varepsilon_{Hf}(t)$ values (-12.2 to -9.91) that are lower than those of HMA formed by direct melting of hydrous mantle (Wood and Turner, 2009). Their enriched Sr-Nd-Pb isotopic compositions are also inconsistent with simple partial melting of a mantle source (Fig. 7).

(2) They have significant depletions in Nb (Nb/La = 0.3–0.4), Ta, Ti, Zr and Hf (Fig. 6b), the quintessential signature of subduction-related rocks (e.g., Defant and Drummond, 1990; Hawkesworth et al. 1997a). Associated high LILEs (e.g., Rb, Sr and Ba; Supplementary Table 3), and high LREEs (Fig. 6a) require enrichment of the mantle source before partial melting. Both these elemental characteristics are likely to be related to subduction of Neo-Tethys oceanic lithosphere (e.g., Ravikant et al., 2009; Liu et al., 2020; Zhang et al., 2022).

(3) The moderate Rb/Ba and Rb/Sr ratios of these high-Mg diorites plot along the mixing trend between basalt and a calculated pelite-derived melt (Fig. 11a), indicating that their magma source was most likely a mixture between basalt and sedimentary rocks. The samples also display a positive correlation between Th/La and Th/Sm (Fig. 11b), consistent with simple binary mixing (i.e., between DMM and GLOSS).

(4) Subduction fluids generally carry LILEs (e.g., Rb, Sr and Ba) and other fluid-mobile trace elements (e.g., U and Pb) into the mantle wedge (Hawkesworth et al., 1997a, b). However, the Kalaqigu high-Mg diorites show low Ba/La (17–32), Ba/Th (51–167), Sr/Th (39–120) and U/Th (0.2–0.4) ratios, indicating that their source was not significantly metasomatized solely by a fluid component (Figs. 11c–11d; Hawkesworth et al., 1997a; Turner et al., 1997). In contrast, addition of sediment is likely to increase La/Sm and Th/Yb (Hanyu et al., 2006; Tatsumi, 2006; Labanieh et al., 2012). All samples yield $(La/Sm)_N$ ratios of 2.4–3.4 and Th/Yb ratios of 1.6–6.5, consistent with the addition of subducted sediments (Figs. 11c–11d), but their partial melting is indicated by higher Th/La and Th/Sm ratios than those in the GLOSS (Fig. 11b). The indicative model curve suggests that the degree of partial melting of GLOSS is ~4%, and the proportion of GLOSS melt in the high-Mg diorites is ~10% (Fig. 11b).

(5) The Sr-Nd-Pb isotopic compositions of the diorites plot within or close to the GLOSS field, also consistent with a subduction-related enrichment (Fig. 7). The diorites also have zircon $\delta^{18}O$ values which are markedly higher than that of the depleted mantle (Fig. 8a), likely inherited from their sedimentary source components

(Valley, 2003; Workman et al., 2005).

To summarize, we infer that the Kalaqigu high-Mg diorites were generated by partial melting of enriched mantle modified by subducted sediment-derived melts.

Mantle Source and Magma Evolution

As mentioned above, the Kalaqigu high-Mg diorites originated from a metasomatized mantle modified by subducted sediments. When high-pressure silicate liquids from the subducted crust are out of equilibrium with the overlying mantle rocks, they will interact with the mantle, resulting in hybrid silicate-carbonate melt compositions (Sekine and Wyllie, 1982; Wyllie and Sekine, 1982; Ionov et al., 1997). These hybrid melts may be consumed by reaction with the overlying mantle rocks, creating metasomatized domains (e.g., Sekine and Wyllie, 1982; Wyllie and Sekine, 1982). The reactions of carbonate-rich melts with overlying peridotite would produce lherzolites and harzburgites (e.g., Lambart et al., 2012). In general, these lherzolites and harzburgites would be in equilibrium with an aluminous mineral which changes from plagioclase to spinel to garnet with increasing pressure (Wyllie, 1979; Müntener and Ulmer, 2018).

These diorites are characterized by only small negative Eu anomalies (Fig. 6a) and moderate fractionation of HREE (Fig. 6b), supporting the absence of plagioclase and garnet as residual phases. Instead, the patterns are consistent with the presence of spinel in the mantle source (Guo et al., 2006). As shown in Figure 12a, Dy/Yb and La/Yb systematics also indicate that the diorites need an enriched mantle source for spinel-harzburgite mantle partial melting. In addition, their high K_2O contents (2.1–3.0 wt.%; Fig. 5b) imply that K-rich phases including phlogopite and/or K-rich amphibole as residual phases occur in the mantle source. However, these diorites have low Rb/Sr (0.1–0.3) and Ba/Rb (4.4–11.0) ratios that suggests the presence of residual phlogopite (Fig. 12b; Furman and Graham, 1999). Phlogopite is a common metasomatic volatile-bearing K-rich phase (e.g., Sekine and Wyllie, 1982; Wyllie and Sekine, 1982) and its consumption usually results in high K_2O contents. Therefore, we propose that the Kalaqigu high-Mg diorites were generated from a phlogopite-bearing spinel-harzburgite mantle and have undergone fractionation of olivine, orthopyroxene and spinel within a lower magma chamber, which is similar to the petrogenesis of sanukitic HMAs (Tatsumi, 2001; Wang et al., 2008).

Petrography demonstrates that amphibole occurs as inclusions in feldspar (Fig. 2a), indicating amphibole was an early crystallizing phase. Biotite and quartz occur as late interstitial crystallizing phases. Thus, the inferred sequence of crystallization is amphibole → plagioclase → biotite + quartz. A previous experimental study has shown that high H_2O contents (> 3%) would suppress plagioclase and lead to earlier crystallization of amphibole (Müntener et al., 2001). Plagioclase crystallization later than amphibole indicates that the primitive parental melts may have had high water contents. This is also supported by the frequent presence of hydrous minerals (amphibole and biotite), high H_2O_{melt} and oxygen fugacity values calculated by amphibole compositions (Supplementary Table 2). Mantle hybridization by influx of sediments and/or partial melts derived from them can directly form pargasitic amphibole (Mandler and Grove 2016). Such amphibole can be stable over a wide range of mantle pressures up to 4 GPa and temperatures of about 1000–1100 °C (Mandler and Grove 2016). In subduction zones, the downgoing slab commonly undergoes multistage dehydration and melting, which continuously releases fluids and melts to metasomatize the mantle wedge (Sekine and Wyllie, 1982; Wyllie and Sekine, 1982). The initial fluids generated by dehydration progressively evolve and are accommodated in the fugitive aqueous phases during heating and solidification of the magma (Wyllie and Sekine, 1982). Thus, the mantle source region may have been metasomatized by fluids prior to the generation of these diorites. This is consistent with the proposal that sanukitic magmas may contain important amounts of dissolved water (Castro, 2020).

As mentioned above, Early Cretaceous magmatic rocks are widely distributed in Chinese Wakhan Corridor (Jiang et al., 2014; Li et al., 2016; Zhang et al., 2022). Among them, mantle-derived magmatic rocks, including basalt-andesite (ca. 100–98 Ma; Zhang et al., 2022) and diorite (ca. 104–100 Ma; Li et al., 2016; Liu et al., 2020), crystallized marginally later than high-Mg diorites in this paper (ca. 106 Ma). Despite this, they exhibit similar Sr-Nd isotopic compositions (Fig. 7a) and are also thought to have been generated from an enriched hydrous mantle source (Liu et al., 2020; Zhang et al., 2022). However, as shown on Fig. 11, the mantle source region of these younger rocks requires more sediment input (i.e., subducted sediments and/or sediments from overlying crust; Li et al., 2016; Liu et al., 2020). Given the similar mantle sources (i.e., phlogopite-bearing spinel-harzburgite mantle; Figs. 12a–12b) over ca. 10 Ma, the metasomatism most likely occurred at a stable depth (<100 km; Wyllie, 1979; Klemme and O'Neill, 2000). During this period (ca. 106–98 Ma), the interaction between partial melts of subducted sediments as well as crustal materials and mantle wedge persisted below the Chinese Wakhan Corridor and led to a relatively uniform, stable enriched mantle source.

Monzogranites

Origin of the inherited zircons

The Kalaqigu S-type monzogranites contain inherited zircon cores with ages of 334–1032 Ma (Figs. 3c–3d). Several alternative mechanisms can explain how these inherited zircons became incorporated into the Early Cretaceous monzogranites. They could potentially be captured from the crustal country rocks during emplacement of granitic magmas. However, there is no obvious evidence of crustal assimilation because no xenoliths of the country rocks have been observed in the studied S-type monzogranites. In addition, whole-rock Sr-Nd isotopes of these monzogranites show relatively limited variations (Fig. 7) and do not change with increasing SiO_2 contents. It is thus unlikely that these inherited zircons were captured from the local continental crust, rather were inherited from crustal sources.

The monzogranites have high $\delta^{18}O$ values of 7.82 to 8.85‰ (Fig. 8b), which are significantly higher than those of igneous zircons from lower crust-derived magmas (5‰–7.5‰; Valley et al., 2005), but close to those of sedimentary rocks ($\delta^{18}O$ > 8 ‰; Valley et al., 2005). In addition, their inherited zircon cores show variable U-Pb ages that are consistent with the ages of detrital zircons in southeastern Pamir (Fig. 3c; Imrecke et al., 2019). Therefore, the geochemical characteristics indicate that the studied S-type monzogranites were most likely generated by melting of Early Paleozoic sedimentary rocks (Imrecke et al., 2019).

Melting mechanism and characteristics of the magma source

As mentioned above, the Kalaqigu monzogranites have unfractionated S-type granites affinities, with high SiO_2 contents, low $Mg^{\#}$ values (Fig. 10a), as well as negative $\varepsilon_{Nd}(t)$ (-12.3 to -12.5). Combined with their peraluminous geochemical signature (Fig. 5d), these characteristics are consistent with a metasedimentary source. In general, the geochemical characteristics of S-type granites are controlled not only by the properties of metasedimentary rocks in the source area, but also by both the extent and mechanism of melting (Patiño Douce and Harris, 1998; Patiño Douce, 1999; Hopkinson et al., 2017). On the one hand, the crustal metasedimentary source can be divided into clay-rich metapelite, and clay-poor metagraywacke (e.g., Sylvester, 1998). The Kalaqigu S-type samples exhibit higher CaO/Na_2O ratios (0.49–0.63) relative to melts derived from metapelite (CaO/Na_2O ratios < 0.5; Jung and Pfänder, 2007). In addition, they have low Rb/Sr and Rb/Ba ratios, suggesting they were derived mainly from clay-poor metagreywacke-derived melts rather than metapelite-derived melts (Fig. 11a; Whalen et al., 1987; Sylvester, 1998). Their geochemical features are also more similar to experimental melts of metagraywacke than that of metapelite (Figs. 13a–13e). In addition to the Chinese Wakhan Corridor, coeval (ca. 119-108 Ma) S-type granites of the Taxkorgan pluton were intruded north of the studied area (Fig. 1b; Jiang et al., 2014; Li et al., 2019; Ma et al., 2023). However, these are characterized by variable CaO/Na_2O (0.21–0.53), Rb/Sr (0.93–3.55) and Rb/Ba (0.32–2.47) ratios (Supplementary Table 3), indicating different source characteristics (i.e., metagreywacke or metapelite-derived melts; Fig. 11a and Figs. 13a–13e). The zircon $\varepsilon_{Hf}(t)$ values of the Taxkorgan samples show a variation of ~4.5 epsilon units (-10 in Jiang et al., 2014 and -14.5 in Li et al., 2019), also indicating that their supracrustal sources were heterogeneous. In summary, we interpret the Kalaqigu S-type monzogranites to be the products of partial melting of metagreywacke, while the Taxkorgan S-type rocks were formed by either metagreywacke or metapelite-derived melts, due to the differences between crustal composition of the Central Pamir and South Pamir (Imrecke et al., 2019).

In addition, water distribution during the melting process also plays an important role in the generation of S-type granites (e.g., Sylvester, 1998; Clemens and Stevens, 2012). Partial melting of metagreywackes can generally be divided into H_2O-fluxed melting and dehydration reactions of hydrous minerals such as muscovite or biotite (Conrad et al., 1988; Montel and Vielzeuf, 1997; Patiño Douce and Harris, 1998). Several observations suggest that the Kalaqigu S-type monzogranites were generated by biotite dehydration melting under water-absent conditions. Firstly, plagioclase dissolves easily in the melt under water-present conditions, which leads to higher Ca and Na contents as well as positive Eu anomalies (Patiño Douce and Harris, 1998; García-Arias et al., 2015). However, these monzogranites have relatively low CaO contents (1.6–2.6 wt.%) and high K_2O/Na_2O ratios (0.6–1.3), distinct from H_2O-fluxed melting of metagreywackes (CaO = 1.4–3.9 wt.%, K_2O/Na_2O = 0.3–1.0, Conrad et al., 1988). Furthermore, they exhibit negative Eu anomalies (Eu/Eu* = 0.67–0.83; Fig. 6c), indicating the existence of residual plagioclase. Secondly, negative correlation between Rb/Sr ratios and Sr but positive correlation with Ba contents are consistent with fluid-absent biotite dehydration melting (Figs. 13e–13f; Inger and Harris, 1993). Similarly, low CaO contents (0.8–1.7 wt.%), high K_2O/Na_2O ratios (1.0–1.5), as well as negative Eu anomalies of Taxkorgan S-type granites (Eu/Eu* = 0.4–0.6; Supplementary Table 3) also suggest they were generated by dehydration melting.

Accordingly, we used a metagreywacke sample from Vielzeuf and Montel (1994) for phase equilibrium modeling to determine the pressure-temperature (P-T) conditions during anatexis (Fig. 14a). Phase equilibrium modeling used the GeoPS software tool (http://www.geology.ren/; Xiang and Connolly, 2022). The contents of biotite and H_2O_{Bt} (H_2O in biotite) decrease with the rising temperature, indicating that anatexis was most likely a result of biotite-dehydration melting reaction (Fig. 14b). This is consistent with peritectic cordierite and K-feldspar with biotite inclusions (Figs. 2c–2d), as cordierite and K-feldspar modes increase at the expense of biotite during prograde melting (Fig. 14c). Therefore, the Kalaqigu S-type monzogranites were probably generated by biotite-dehydration melting from metagreywacke.

Estimating P–T conditions is essential to constrain not only the melting mechanism, but also the nature of magma source and process of magma crystallization. According to our phase equilibrium modeling (Figs. 14b–14c), the reaction biotite + plagioclase + quartz = orthopyroxene + garnet (under high pressure)/cordierite (under low pressure) + K-feldspar + melt occurs during the fluid-absent partial melting of metagreywacke, consistent with previous studies (Thompson, 1982; Clemens, 1984; Vielzeuf and Montel, 1994). The formation of garnet and its existence as a residual phase in the source area are also accordance with the geochemical features of these monzogranites (particularly REE fractionation; Fig. 6c).

As the biotite occurs as late interstitial crystallizing phase, the pressures (5.5–6.4 kbar, with an average of 6.0 kbar) and temperatures (746–772 ℃, with an average of 757 ℃) of the biotites represent minimum estimates (Fig. 14a), corresponding to the magma pressure and temperature during late-stage crystallization. The disappearance of biotite represents the completion of biotite-dehydration melting (Vielzeuf and Montel, 1994), which suggests that crystallization began at ~850 ℃ and >6 kbar. The calculated and estimated pressure-temperature results are also in agreement with the inferred range of pressure conditions based on experimental phase relations (Fig. 14a). Under these P-T conditions, the inferred sequence of crystallization is likely to be K-feldspar → plagioclase → cordierite → biotite + quartz. This interpretation is supported by the petrological observation that K-feldspar occurs as phenocrysts and biotite occurs as inclusions in the K-feldspar and cordierite (Fig. 2c). In brief, we consider that the magma of Kalaqigu S-type monzogranites formed at pressures > 6 kbar, corresponding to lower crustal conditions.

Tectonic Implications

Onset of Andean-type Continental Arc

It has been proposed that there are two arcs in South Pamir, namely the

Kohistan-Ladakh intra-oceanic arc and the continental arc subducted northward along the SSZ in the South Pamir-Karakorum (Zanchi et al., 2000; Zanchi and Gaetani, 2011; Chapman et al., 2018a). The Early Cretaceous high-Mg diorites, and the mantle-derived volcanic rocks in the Wakhan Corridor, show enrichment in LILEs and depletion in Nb, Ta and HFSEs, suggesting an arc affinity (Figs. 6 and Fig. 15a; Ji et al., 2016; Liu et al., 2020; Zhang et al., 2022). These units have geochemical signature of continental arc magmatic rocks, as determined on Nb/Yb versus Th/Yb and Ti/V versus Th/Nb diagrams (Figs. 15b–15c; Shervais, 2022). Previous studies suggested that the Neo-Tethys oceanic lithosphere subducted northward along the SSZ beneath the Karakoram terrane (Fraser et al., 2001; Bouilhol et al., 2013; Kumar et al., 2017; Chapman et al., 2018a). This resulted in a combination of continental arc magmatism in the South Pamir and the development of the thrust belt in the North Pamir and Central Pamir (Robinson et al., 2004; Imrecke et al., 2019; Li et al., 2022; Villarreal et al., 2023), forming an Andean style orogenic belt, similar to the western North American Cordillera (Dickinson et al., 1978; Gutscher et al., 2000; Axen et al., 2018). Thus, it is reasonable to deduce that the Early Cretaceous intrusive rocks have similar Andean-type continental arc-related fingerprints and have developed along the Neo-Tethys oceanic subduction zone.

Our new zircon U–Pb data combined with previously published data show that there were two episodes of Early Cretaceous continental arc magmatism in the Wakhan Corridor (Fig. 15d). In the first stage (ca. 115-102 Ma with ca. 105 Ma as a high-flux event), extensive crustal remelting and crust-mantle interaction formed continental arc-related magmatic rocks (Fig. 15d). Following this episode (ca. 107-98 Ma), a relatively small volume of mantle-derived rocks formed in the South Pamir-Karakorum (Figs. 15d and 16a). In the Early Cretaceous, the Neo-Tethys oceanic lithosphere may have undergone low-angle to flat subduction beneath the South Pamir-Karakoram (e.g., Fraser et al., 2001; Bouilhol et al., 2013; Kumar et al., 2017; Chapman et al., 2018a). This is further supported by the magmatic migration from the Wakhan Corridor to the northwest Teshiktash-Beik (Fig.15d; Aminov et al., 2017; Ma et al., 2023). During this period, the subduction of the oceanic slab produced fluids at sub-arc depths, which induced melting of mantle wedge, interaction with overlying Pamir crust as well as the remelting of the ancient lower crust (Fig. 16a). In this scenario, a series of granitoids at ca. 105 Ma as a high-flux event formed arc-related magmatic rocks (Figs. 15d and 16a). Following this period, mantle-derived basalt-andesite as well as the studied high-Mg diorites in the Wakhan Corridor resulted from interaction between slab melts (i.e., sedimentary melts) and the mantle (Figs. 15d and 16b). We propose that subducted sediments played an important role in the formation of the mantle-derived magmatic rocks in the Wakhan Corridor during the Early Cretaceous (Figs. 7, 8 and 11).

Implications for the Correlation of Early Cretaceous S-type Granites

As mentioned above, contemporaneous S-type granites are also exposed in the Taxkorgan pluton, albeit slightly earlier (ca. 118-108 Ma; Jiang et al., 2014; Li et al., 2019; Ma et al., 2023) than that in the Wakhan Corridor (Figs. 15c and 16a). They also exhibit typical subduction-related continental arc geochemistry (Figs. 15b-15c; Jiang et al., 2014; Li et al., 2019) and have the geochemical characteristics of syn-collisional granite (Fig. 15a; Pearce et al., 1984). Based on the temporal-spatial evolution of Cretaceous arc magmatism in the Pamir, it is likely that the Taxkorgan S-type granites were generated in a collisional setting caused by the northward subduction of the Neo-Tethys oceanic lithosphere (Fig. 16a). The north-south difference in crystallization age indicates that the collisional compression caused by subduction occurred slightly earlier than the flare-up of the South Pamir-Karakoram magmas.

Furthermore, the crustal source of the Taxkorgan S-type granites is heterogeneous (i.e., metagreywacke and metapelite; Figs. 11a, 13a-d and 16a). Based on the structural relationships and distribution of rock units Imrecke et al. (2019) suggested that southeast Pamir consists of two distinct structural/lithologic domains: the northern schist and gneiss region and the southern metamorphic sedimentary rocks. Previous studies have shown that low-angle or flat-slab subduction is closely related to upper plate shortening and back-arc deformation (Egawa, 2013; Gianni et al., 2018;

Schellart, 2020). The Cretaceous Neo-Tethys oceanic slab migrated progressively landward from South Pamir-Karakorum to the north beneath the Pamir crust. This resulted in a maximum arc-trench distance of ca. 400 km in the Early Cretaceous (Ma et al., 2023), and caused obvious retroarc shortening (Robinson et al., 2007, 2012), as well as imbrication in the Taxkorgan due to the development of a regionally extensive thrust nappe in the North Pamir (Imrecke et al., 2019). Thus, we interpret that such imbrication along SW-vergent thrust is the main reason for the heterogeneous crustal source of the S-type granites.

Landward arc migration caused by flat-subduction is often accompanied by shortening and thickening events (e.g., Gianni et al., 2018). Research on low-temperature thermochronology, sedimentary petrology and metamorphic petrology show that Early Cretaceous (ca. 140-110 Ma) crustal shortening and thickening appears to be focused along the North Pamir (Robinson et al., 2012; Robinson, 2015; Villarreal et al., 2023). This is manifested in the amphibolite-facies metamorphism at ca. 130-110 Ma (Robinson et al., 2004), broadly coeval exhumation in the hanging wall of thrusts (Robinson et al., 2007; Imrecke et al., 2019; Villarreal et al., 2023), as well as the widespread occurrence of thrust fault movement in the North Pamir (Chapman et al., 2018b; Li et al., 2022; Villarreal et al., 2023). These observations, combined with Taxkorgan syn-collisional granites, suggest the subduction of the Neo-Tethys oceanic slab resulted in compressive deformation primarily occurring far north of the subduction zone during the Early Cretaceous, which also caused a general lack of magmatism in this area (Ma et al., 2023). This compression-dominated environment also resulted in significant crustal thickening in the Pamir during the Early Cretaceous (Li et al., 2022; Ma et al., 2023; Villarreal et al., 2023). Following this period, prograde metamorphism indicates southward migration of crustal shortening and thickening into the Central Pamir and South Pamir have occurred during ca. 110-75 Ma (Chapman et al., 2018b), broadly coeval with the main phase of magmatism in the South Pamir-Karakorum (Fig. 15d).

To summarize, we interpret Early Cretaceous crustal shortening to have resulted from the low-angle and flat-subduction of Neo-Tethys oceanic lithosphere (Fig. 16).

Crustal thickening could have been caused by regional compression (Fig. 16a) as well as addition of mantle-derived magma (Fig. 16b) (Ma et al., 2023). In the Late Cretaceous (<90 Ma), the Neo-Tethys Oceanic slab may have undergone slab roll-back, which resulted in extension-related magmatism in the Pamir (Fig. 16b; Chapman et al., 2018a).

CONCLUSIONS

(1) Zircon LA-ICP-MS U-Pb dating reveals that Kalaqigu high-Mg diorites and S-type monzogranites in the Wakhan Corridor were emplaced in the Early Cretaceous (ca. 108.4–105.9 Ma).

(2) The high-Mg diorites formed from an enriched phlogopite-bearing spinel-lherzolite hydrous mantle source modified by subducted sediment-derived melts, and underwent low-degree fractionation of olivine and orthopyroxene.

(3) The S-type monzogranites were generated by biotite-dehydration melting from metagreywacke under lower crustal conditions.

(4) In the subduction zone beneath the South Pamir, the subducted slab first underwent dehydration and the resultant fluids generated a hydrous mantle source and induced crust-mantle interaction as well as remelting of the lower crust to generate granitoids. The partial melts of subducted sediments then continued to metasomatize the mantle wedge, which generated extensive mantle-derived magmatic rocks.

(5) The northward low-angle flat-subduction of Neo-Tethys oceanic lithosphere had subducted and migrated inland underneath the Pamir continent, leading to significant Early Cretaceous continental-arc magmatism, inducing crust-mantle interaction beneath the South Pamir and resulting in crustal shortening and thickening in the Pamir.

ACKONWLEDGMENTS

We thank Science Editor Brad Singer and Associate Editor Lu Wang for their editorial help and constructive comments. We are grateful to two anonymous reviewers, whose insightful and constructive reviews greatly improve this manuscript.

We also appreciate the assistance of Xiaoping Xia, Zexian Cui and Yueheng Yang in zircon U-Pb-Hf-O isotope analyses and Xiaohong Mao in the mineralogical analysis. This study was financially supported by the second Tibet Plateau Scientific Expedition and Research Program (STEP), Grant No. 2019QZKK0802), the National Key Research and Development Project (Nos. 2022YFC2903302 and 2019YFA0708601), National Natural Science Foundation of China (Nos. 3231101056, 41830216 and 42127801), the China Geological Survey (Grant no. DD20230213) and the Outlay Research Fund of Institute of Geology, Chinese Academy of Geological Sciences (Grant no. J2207). This is a contribution to IGCP 662.

REFERENCES CITED

Aminov, J., Ding, L., Mamadjonov, Y., Dupont-Nivet, G., Aminov, J., Zhang, L.Y., Yoqubov, S., Aminov, J., and Abdulov, S., 2017, Pamir Plateau formation and crustal thickening before the India-Asia collision inferred from dating and petrology of the 110–92Ma Southern Pamir volcanic sequence: Gondwana Research, v. 51, p. 310-326, https://doi.org/10.1016/j.gr.2017.08.003.

Angiolini, L., Zanchi, A., Zanchetta, S., Nicora, A., and Vezzoli, G., 2013, The Cimmerian geopuzzle: new data from South Pamir: Terra Nova, v. 25, p. 352-360, https://doi.org/10.1111/ter.12042.

Axen, G.J., Van Wijk, J.W., and Currie, C.A., 2018, Basal continental mantle lithosphere displaced by flat-slab subduction: Nature Geoscience, v. 11, p. 961-964, https://doi.org/10.1038/s41561-018-0263-9.

Barbarin, B., 1996, Genesis of the two main types of peraluminous granitoids: Geology, v. 24, p. 295-298, https://doi.org/10.1130/0091-7613(1996)024<0295:GOTTMT>2.3.CO;2.

Barbarin, B., 1999, A review of the relationships between granitoid types, their origins and their geodynamic environments: Lithos, v. 46, p. 605-626, https://doi.org/10.1016/S0024-4937(98)00085-1.

Belousova, E., Griffin, W., O'Reilly, S.Y., and Fisher, N., 2002, Igneous zircon: trace element composition as an indicator of source rock type: Contributions to

Mineralogy and Petrology, v. 143, p. 602-622, https://doi.org/10.1007/s00410-002-0364-7.

Bouilhol, P., Jagoutz, O., Hanchar, J.M., and Dudas, F.O., 2013, Dating the India–Eurasia collision through arc magmatic records: Earth and Planetary Science Letters, v. 366, p. 163-175, https://doi.org/10.1016/j.epsl.2013.01.023.

Burtman, V.S., and Molnar, P., 1993, Geological and geophysical evidence for deep subduction of continental crust beneath the Pamir: Geological Society of America Special Papers, 281 p, https://doi.org/10.1130/SPE281-p1.

Cashman, K.V., Sparks, R.S.J., and Blundy, J.D., 2017, Vertically extensive and unstable magmatic systems: A unified view of igneous processes: Science, v. 355, p. eaag3055, https://doi.org/10.1126/science.aag3055.

Castro, A., 2020, The dual origin of I-type granites: the contribution from experiments, in Janoušek, V., Bonin, B., Collins, W.J., Farina, F., and Bowden, P., eds., Post-Archean Granitic Rocks: Petrogenetic Processes and Tectonic Environments, 491*491, Geological Society of London, p. 0, https://doi.org/10.1144/SP491-2018-110.

Chapman, J.B., Scoggin, S.H., Kapp, P., Carrapa, B., Ducea, M.N., Worthington, J., Oimahmadov, I., and Gadoev, M., 2018a, Mesozoic to Cenozoic magmatic history of the Pamir: Earth and Planetary Science Letters, v. 482, p. 181-192, https://doi.org/10.1016/j.epsl.2017.10.041.

Chapman, J.B., Robinson, A.C., Carrapa, B., Villarreal, D., Worthington, J., DeCelles, P.G., Kapp, P., Gadoev, M., Oimahmadov, I., and Gehrels, G., 2018b, Cretaceous shortening and exhumation history of the South Pamir terrane: Lithosphere, v. 10, p. 494-511, https://doi.org/10.1130/L691.1.

Chappell, B.W., and White, A.J.R., 1974, Two contrasting granite types: Pacific Geology, v. 8, p. 173-174.

Chappell, B.W., and White, A.J.R., 1992, I- and S-type granites in the Lachlan Fold Belt: Transactions of the Royal Society of Edinburgh, v. 83, p. 1-26, https://doi.org/10.1017/S0263593300007720.

Chen, B., Jahn, B., and Suzuki, K., 2012, Petrological and Nd-Sr-Os isotopic constraints on the origin of high-Mg adakitic rocks from the North China Craton: Tectonic implications: Geology, v. 41, p. 91-94, https://doi.org/10.1130/G33472.1.

Clemens, J.D., 1984, Water contents of silicic to intermediate magmas: Lithos, v. 17, p. 273-287, https://doi.org/10.1016/0024-4937(84)90025-2.

Clemens, J.D., and Stevens, G., 2012, What controls chemical variation in granitic magmas? Lithos, v. 134-135, p. 317-329, https://doi.org/10.1016/j.lithos.2012.01.001.

Conrad, W.K., Nicholls, I.A., and Wall, V.J., 1988, Water-saturated and -undersaturated melting of metaluminous and peraluminous crustal compositions at 10 kb: Evidence for the origin of silicic magmas in the Taupo Volcanic Zone, New Zealand, and Other Occurrences: Journal of Petrology, v. 29, p. 765-803, https://doi.org/10.1093/petrology/29.4.765.

Davidson, J.P., and Arculus, R.J., 2006, The significance of Phanerozoic arc magmatism in generating continental crust, in Brown, M., & Rushmer, T., (eds.) Evolution and Differentiation of the Continental Crust: New York, Cambridge University Press, p. 135-151.

Deer, W.A.F., Howie, R.A., and Zussman, J., 2013, An Introduction to the Rock-Forming Minerals, Mineralogical Society of Great Britain and Ireland, https://doi.org/10.1180/DHZ.

Defant, M.J., and Drummond, M.S., 1990, Derivation of some modern arc magmas by melting of young subducted lithosphere: Nature, 347, p. 662-665, https://doi.org/10.1038/347662a0.

DePaolo, D.J., 1981, Trace element and isotopic effects of combined wallrock assimilation and fractional crystallization: Earth and Planetary Science Letters, v. 53, p. 189-202, https://doi.org/10.1016/0012-821X(81)90153-9.

Dhuime, B., Hawkesworth, C.J., Cawood, P.A., and Storey, C.D., 2012, A change in the geodynamics of continental growth 3 billion years ago: Science, v. 335, p. 1334-1336, https://doi.org/10.1126/science.1216066.

Dickinson, W.R., Snyder, W.S., and Matthews, V., 1978, Plate tectonics of the

Laramide orogeny: Matthews, v. 3, p. 355-366, https://doi.org/10.1130/mem151-p355.

Ducea, M.N., Saleeby, J.B., and Bergantz, G., 2015, The architecture, chemistry, and evolution of continental magmatic arcs: Annual Review Earth and Planetary Sciences, v. 43, p. 299-331, https://doi.org/10.1146/annurev-earth-060614-105049.

Egawa, K., 2013, East Asia-wide flat slab subduction and Jurassic synorogenic basin evolution in West Korea. In Mechanism of Sedimentary Basin Formation Multidisciplinary Approach on Active Plate Margins. In Tech, https://doi.org/10.5772/56770.

Faisal, S., Larson, K.P., King, J., and Cottle, J.M., 2016, Rifting, subduction and collisional records from pluton petrogenesis and geochronology in the Hindu Kush, NW Pakistan: Gondwana Research, v. 35, p. 286-304, https://doi.org/10.1016/j.gr.2015.05.014.

Foster, M.D., 1960, Interpretation of the composition of trioctahedral micas: USGS Professional Paper, v. 354, p. 11-48, https://doi.org/10.3133/pp354B.

Fraser, J.E., Searle, M.P., Parrish, R.R., and Noble, S.R., 2001, Chronology of deformation, metamorphism, and magmatism in the southern Karakoram Mountains: GSA Bulletin, v. 113, p. 1443-1455, https://doi.org/10.1130/0016-7606(2001)113<1443:CODMAM>2.0.CO;2.

Furman, T., and Graham, D., 1999, Erosion of lithospheric mantle beneath the East African Rift system: geochemical evidence from the Kivu volcanic province: Lithos, v. 48, p. 237-262, https://doi.org/10.1016/S0419-0254(99)80014-7.

Gao, P., Zheng, Y.F., and Zhao, Z.F., 2016, Distinction between S-type and peraluminous I-type granites: Zircon versus whole-rock geochemistry: Lithos, v. 258-259, p. 77-91, https://doi.org/10.1016/j.lithos.2016.04.019.

García-Arias, M., Corretgé, L.G., Fernández, C., and Castro, A., 2015, Water-present melting in the middle crust: The case of the Ollo de Sapo gneiss in the Iberian Massif (Spain): Chemical Geology, v. 419, p. 176-191, https://doi.org/10.1016/j.chemgeo.2015.10.040.

Gianni, G.M., Dávila, F.M., Echaurren, A., Fennell, L., Tobal, J., Navarrete, C., Quezada, P., Folguera, A., and Giménez, M., 2018, A geodynamic model linking cretaceous orogeny, arc migration, foreland dynamic subsidence and marine ingression in southern South America: Earth-Science Review, v. 185, p. 437-462, https://doi.org/10.1016/j.earscirev.2018.06.016.

Gianni, G.M., and Luján, S.P., 2021, Geodynamic controls on magmatic arc migration and quiescence: Earth-Science Reviews, v. 218, p. 103676, https://doi.org/10.1016/j.earscirev.2021.103676.

Guo, Z.F., Wilson, M., Liu, J.Q., and Mao, Q., 2006, Post-collisional, potassic and ultrapotassic magmatism of the northern Tibetan Plateau: Constraints on characteristics of the mantle source, geodynamic setting and uplift mechanisms: Journal of Petrology, v. 47, p. 1177-1220, https://doi.org/10.1093/petrology/egl007.

Gutscher, M.A., Spakman, W., Bijwaard, H., and Engdahl, E.R., 2000, Geodynamics of flat subduction: Seismicity and tomographic constraints from the Andean margin: Tectonics, v. 19, p. 814-833, https://doi.org/10.1029/1999tc001152.

Hanyu, T., Tatsumi, Y., Nakai, S., Chang, Q., Miyazaki, T., Sato, K., Tani, K., Shibata, T., and Yoshida, T., 2006, Contribution of slab melting and slab dehydration to magmatism in the NE Japan arc for the last 25 Myr: Constraints from geochemistry: Geochemistry, Geophysics, Geosystems, v. 7, p. Q08002, https://doi.org/10.1029/2005GC001220.

Hart, S.R., 1988, Heterogeneous mantle domains: signatures, genesis and mixing chronologies: Earth and Planetary Science Letters, v. 90, p. 273-296, https://doi.org/10.1016/0012-821X(88)90131-8.

Hawkesworth, C.J., Turner, S.P., McDermott, F., Peate, D.W., and van Calsteren, P., 1997a, U-Th isotopes in arc magmas: implications for element transfer from the subducted crust: Science, v. 276, p. 551-555, https://doi.org/10.1126/science.276.5312.551.

Hawkesworth, C., Turner, S., Peate, D., McDermott, F., and van Calsteren, P., 1997, Elemental U and Th variations in island arc rocks: implications for U-series isotopes: Chemical Geology, v. 139, p. 207-221, https://doi.org/10.1016/S0009-2541(97)00036-3.

Hawthorne, F.C., and Oberti, R., 2007, Classification of the amphiboles: Reviews in Mineralogy and Geochemistry, v. 67, p. 55-88, https://doi.org/10.2138/rmg.2007.67.2.

Heuberger, S., Schaltegger, U., Burg, J., Villa, I., Frank, M., Dawood, H., Hussain, S., and Zanchi, A., 2007, Age and isotopic constraints on magmatism along the Karakoram-Kohistan Suture Zone, NW Pakistan: Evidence for subduction and continued convergence after India-Asia collision: Swiss Journal of Geosciences, v. 100, p. 85-107, https://doi.org/10.1007/s00015-007-1203-7.

Hirose, K., 1997, Melting experiments on lherzolite KLB-1 under hydrous conditions and generation of high-magnesian andesitic melts: Geology, v. 25, p. 42-44, https://doi.org/10.1130/0091-7613(1997)025<0042:MEOLKU>2.3.CO;2.

Hopkinson, T.N., Harris, N.B.W., Warren, C.J., Spencer, C.J., Roberts, N.M.W., Horstwood, M.S.A., Parrish, R.R., and EIMF, 2017, The identification and significance of pure sediment-derived granites: Earth and Planetary Science Letters, v. 467, p. 57-63, https://doi.org/10.1016/j.epsl.2017.03.018.

Hoskin, P.W.O., and Schaltegger, U., 2003, The composition of zircon and igneous and metamorphic petrogenesis: Reviews in Mineralogy and Geochemistry, v. 53, p. 27-62, https://doi.org/10.2113/0530027.

Imrecke, D.B., Robinson, A.C., Owen, L.A., Chen, J., Schoenbohm, L.M., Hedrick, K.A., Lapen, T.J., Li, W., and Yuan, Z., 2019, Mesozoic evolution of the eastern Pamir: Lithosphere, v. 11, p. 560-580, https://doi.org/10.1130/L1017.1.

Inger, S., and Harris, N., 1993, Geochemical constraints on leucogranite magmatism in the Langtang Valley, Nepal Himalaya: Journal of Petrology, v. 34, p. 345-368, https://doi.org/10.1093/petrology/34.2.345.

Ionov, D.A., Griffin, W.L., and O'Reilly, S.Y., 1997, Volatile-bearing minerals and lithophile trace elements in the upper mantle: Chemical Geology, v. 141, p. 153-184, https://doi.org/10.1016/S0009-2541(97)00061-2.

Jagoutz, O., and Schmidt, M.W., 2012, The formation and bulk composition of modern juvenile continental crust: The Kohistan arc: Chemical Geology, v. 298-299, p. 79-96, https://doi.org/10.1016/j.chemgeo.2011.10.022.

Ji, W., Li, R., Chen, S., He, S., Zhao, Z., Bian, X., Zhu, H., Cui, J., and Ren, J., 2011, The discovery of Palaeoproterozoic volcanic rocks in the Bulunkuoler Group from the Tianshuihai Massif in Xinjiang of Northwest China and its geological significance: Science China Earth Sciences, v. 54, p. 61-72, https://doi.org/10.1007/s11430-010-4043-7.

Jiang, Y.H., Liu, Z., Jia, R.Y., Liao, S.Y., Zhao, P., and Zhou, Q., 2014, Origin of Early Cretaceous high-K calc-alkaline granitoids, western Tibet: implications for the evolution of the Tethys in NW China: International Geology Review, v. 56, p. 88-103, https://doi.org/10.1080/01431161.2013.819963.

Jung, S., and Pfänder, J.A., 2007, Source composition and melting temperatures of orogenic granitoids: constraints from CaO/Na_2O, Al_2O_3/TiO_2 and accessory mineral saturation thermometry: European Journal of Mineralogy, v. 19, p. 859-870, https://doi.org/10.1127/0935-1221/2007/0019-1774.

Kamei, A., Owada, M., Nagao, T., and Shiraki, K., 2004, High-Mg diorites derived from sanukitic HMA magmas, Kyushu Island, southwest Japan arc: evidence from clinopyroxene and whole rock compositions: Lithos, v. 75, p. 359-371, https://doi.org/10.1016/j.lithos.2004.03.006.

Kelemen, P.B., 1995, Genesis of high Mg# andesites and the continental crust: Contributions to Mineralogy and Petrology, v. 120, p. 1-19, https://doi.org/10.1007/BF00311004.

Kelemen, P.B., Yogodzinski, G.M., and Scholl, D.W., 2004, Along-strike variation in the Aleutian Island Arc: Genesis of high $Mg^{\#}$ andesite and implications for continental crust, inside the subduction factory, J. Eiler (Ed.), p. 223-276, https://doi.org/10.1029/138GM11.

Klemme, S., and O'Neill, H.S., 2000, The near-solidus transition from garnet lherzolite to spinel lherzolite: Contributions to Mineralogy and Petrology, v. 138, p. 237-248, https://doi.org/10.1007/s004100050560.

Krawczynski, M.J., Grove, T.L., and Behrens, H., 2012, Amphibole stability in primitive arc magmas: effects of temperature, H_2O content, and oxygen fugacity: Contributions to Mineralogy and Petrology, v. 164, p. 317-339, https://doi.org/10.1007/s00410-012-0740-x.

Kumar, S., Bora, S., Sharma, U.K., Yi, K., and Kim, N., 2017, Early Cretaceous subvolcanic calc-alkaline granitoid magmatism in the Nubra-Shyok valley of the Shyok Suture Zone, Ladakh Himalaya, India: Evidence from geochemistry and U–Pb SHRIMP zircon geochronology: Lithos, v. 277, p. 33-50, https://doi.org/10.1016/j.lithos.2016.11.019.

Labanieh, S., Chauvel, C., Germa, A., and Quidelleur, X., 2012, Martinique: a clear case for sediment melting and slab dehydration as a function of distance to the trench: Journal of Petrology, v. 53, p. 2441-2464, https://doi.org/10.1093/petrology/egs055.

Lambart, S., Laporte, D., Provost, A., and Schiano, P., 2012, Fate of pyroxenite-derived melts in the peridotitic mantle: thermodynamic and experimental constraints: Journal of Petrology, v. 53, p. 451-476, https://doi.org/10.1093/petrology/egr068.

Le Maitre, R.W., 1989, A classification of Igneous Rock and Glossary of Terms. 2nd Edition: Blackwell Science Publication, Oxford, 193p.

Leake, B.E., Woolley, A.R., Arps, C.E.S., Birch, W.D., Gilbert, M.C., Grice, J.D., Hawthorne, F.C., Kato, A., Kisch, H.J., Krivovichev, V.G., Linthout, K., Laird, J., Mandarino, J.A., Maresch, W.V., Nickel, E.H., Rock, N.M.S., Schumacher, J.C., Smith, D.C., Stephenson, N.C.N., Ungaretti, L., Whittaker, E.J.W., and Youzhi, G., 1997, Nomenclature of amphiboles; Report of the Subcommittee on Amphiboles of the International Mineralogical Association, Commission on New Minerals and Mineral Names: American Mineralogist, v. 82, p. 1019-1037.

Lei, C.Y., Wang, L.Q., Tang, J.X., Li, W., Gao, T., and Yuan, H.Y., 2023, Origin of Qushenla formation volcanic rocks in the Nawucuo Area, Northern Tibet, and constraints on the subduction polarity of the Bangong-Nujiang Tethys Ocean: Journal of Earth Science, v. 34, p. 467-486, https://doi.org/10.1007/s12583-020-1076-5.

Li, J.Y., Niu, Y.L., Hu, Y., Chen, S., Zhang, Y., Duan, M., and Sun, P., 2016, Origin of the late Early Cretaceous granodiorite and associated dioritic dikes in the Hongqilafu pluton, northwestern Tibetan Plateau: A case for crust–mantle interaction: Lithos, v. 260, p. 300-314, https://doi.org/10.1016/j.lithos.2016.05.028.

Li, R.H., Peng, B., Zhao, C.S., Yu, M., Song, L.S., and Zhang, H., 2019, Origin of Early Creceouscalc-alkaline granite, Taxkorgan: Implications for evolution of Tethys evolution in central Pamir: Journal of Central South University, v. 26, p. 3470-3487, https://doi.org/10.1007/s11771-019-4267-4.

Li, X.Y., and Zhang, C., 2022, Machine learning thermobarometry for biotite-bearing magmas: Journal of Geophysical Research: Solid Earth, v. 127, p. e2022JB024137, https://doi.org/10.1029/2022JB024137.

Li, Y.P., Robinson, A.C., Zucali, M., Gadoev, M., Oimuhammadzoda, I., Lapen, T.J., and Carrapa, B., 2022, Mesozoic Tectonic Evolution in the Kurgovat-Vanch Complex, NW Pamir: Tectonics, v. 41, p. e2021TC007180, https://doi.org/10.1029/2021TC007180.

Liu, D.L., Li, H.B., Sun, Z.M., Cao, Y., Wang, L.Z., Pan, J.W., Han, L., and Ye, X.Z., 2017, Cenozoic episodic uplift and kinematic evolution between the Pamir and Southwestern Tien Shan: Tectonophysics, v. 712-713, p. 438-454, https://doi.org/10.1016/j.tecto.2017.06.009.

Liu, X.Q., Zhang, C.L., Hao, X.S., Zou, H.B., Zhao, H.X., and Ye, X.T., 2020, Early Cretaceous granitoids in the Southern Pamir: Implications for the Meso-Tethys evolution of the Pamir Plateau: Lithos, v. 362-363, p. 105492, https://doi.org/10.1016/j.lithos.2020.105492.

Loiselle, M.C., and Wones, D.R., 1979, Characteristics and origin of anorogenic granites: Geological Society of America Abstracts with Programs, v. 11, p. 468.

Ma, L., Wang, Q., Wyman, D.A., Li, Z.X., Jiang, Z.Q., Yang, J.H., Gou, G.N., and Guo, H.F., 2013, Late Cretaceous (100–89Ma) magnesian charnockites with adakitic affinities in the Milin area, eastern Gangdese: Partial melting of subducted oceanic crust and implications for crustal growth in southern Tibet:

Lithos, v. 175-176, p. 315-332, https://doi.org/10.1016/j.lithos.2013.04.006.

Ma, X., Dan, W., Wang, J., Wang, Q., Tang, G.R., Gadoev, M., Oimahmadov, I., and Tang, G.J., 2023, Cretaceous magmatic migration and flare-up in Pamir–Karakoram: Lithos, v. 454-455, p. 107285, https://doi.org/10.1016/j.lithos.2023.107285.

Ma, Z.J., Chai, F.M., Wang, W., Mao, Q.G., Qi, D.M., and Zhang, X.B., 2022, Petrogenesis of Pingtaishan Compound Massif in the Eastern Tianshan, NW China, and its implications on Late Paleozoic ridge subduction: Earth Science, v. 47, p. 3210-3228, https://doi.org/10.3799/dqkx.2021.213.

Macpherson, C.G., Dreher, S.T., and Thirlwall, M.F., 2006, Adakites without slab melting: High pressure differentiation of island arc magma, Mindanao, the Philippines: Earth and Planetary Science Letters, v. 243, p. 581-593, https://doi.org/10.1016/j.epsl.2005.12.034.

Mandler, B.E., and Grove, T.L., 2016, Controls on the stability and composition of amphibole in the Earth's mantle: Contributions to Mineralogy and Petrology, v. 171, p. 68, http://doi.org/DOI10.1007/s00410–016–1281–5.

Maniar, P.D., and Piccoli, P.M., 1989, Tectonic discrimination of granitoids: Geological Society of America Bulletin, v. 101, p. 635-643, https://doi.org/10.1130/0016-7606(1989)101<0635:TDOG>2.3.CO;2.

Martin, H., Smithies, R.H., Rapp, R., Moyen, J.F., and Champion, D., 2005, An overview of adakite, tonalite–trondhjemite–granodiorite (TTG), and sanukitoid: Relationships and some implications for crustal evolution: Lithos, v. 79, p. 1-24, https://doi.org/10.1016/j.lithos.2004.04.048.

Middlemost, E.A.K., 1994. Naming materials in the magma/igneous rock system: Earth-Science Reviews, v. 37, p. 215–224, https://doi.org/10.1016/0012-8252(94)90029-9.

Mitchell, A.L., and Grove, T.L., 2015, Melting the hydrous, subarc mantle: the origin of primitive andesites: Contributions to Mineralogy and Petrology, v. 170, p. 13, https://doi.org/10.1007/s00410-015-1161-4.

Montel, J., and Vielzeuf, D., 1997, Partial melting of metagreywackes, Part II.

Compositions of minerals and melts: Contributions to Mineralogy and Petrology, v. 128, p. 176-196, https://doi.org/10.1007/s004100050302.

Müntener, O., Kelemen, P.B., and Grove, T.L., 2001, The role of H_2O during crystallization of primitive arc magmas under uppermost mantle conditions and genesis of igneous pyroxenites: an experimental study: Contributions to Mineralogy and Petrology, v. 141, p. 643-658, https://doi.org/10.1007/s004100100266.

Müntener, O., and Ulmer, P., 2018, Arc crust formation and differentiation constrained by experimental petrology: American Journal of Science, v. 318, p. 64-89, https://doi.org/10.2475/01.2018.04.

Patiño Douce, A.E., and Harris, N., 1998, Experimental constraints on Himalayan anatexis: Journal of Petrology, v. 39, p. 689-710, https://doi.org/10.1093/petroj/39.4.689.

Patiño Douce, A.E., 1999, What do experiments tell us about the relative contributions of crust and mantle to the origin of granitic magmas? In: Castro, A., Fernandez, C., Vigneresse, J.L., (Eds.), Understanding granite. Geological Society of London, Special Publications, v. 168, p. 55-75, https://doi.org/10.1144/GSL.SP.1999.168.01.05.

Pearce, J.A., Harris, N.B.W., and Tindle, A.G., 1984, Trace element discrimination diagrams for the tectonic interpretation of granitic rocks: Journal of Petrology, v. 25, no. 4, p. 956-983, https://doi:10.1093/petrology/25.4.956.

Plank, T., and Langmuir, C.H., 1998, The chemical composition of subducting sediment and its consequences for the crust and mantle: Chemical Geology, v. 145, p. 325-394, https://doi.org/10.1016/S0009-2541(97)00150-2.

Plank, T., 2005, Constraints from thorium/lanthanum on sediment recycling at subduction zones and the evolution of the continents: Journal of Petrology, v. 46, p. 921-944, https://doi.org/10.1093/petrology/egi005.

Qi, H., Zhao, J.H., and Johnson, T.E., 2023, The fundamental role of H_2O in the generation of coeval sodic and potassic granitoids at continental arcs: An example from the Yangtze Block, South China: Journal of Petrology, v. 64, p.

egad024, https://doi.org/10.1093/petrology/egad024.

Qin, S.K., Zhang, Z.M., Palin, R.M., Ding, H.X., Dong, X., and Tian, Z.L., 2022, Tectonic burial of sedimentary rocks drives the building of juvenile crust of magmatic arc: Geological Society of America Bulletin, v. 134, p. 3064-3078, https://doi.org/10.1130/B36271.1.

Rapp, R.P., Shimizu, N., Norman, M.D., and Applegate, G.S., 1999, Reaction between slab derived melts and peridotite in the mantle wedge: experimental constraints at 3.8 Gpa: Chemical Geology, v. 160, p. 335–356, https://doi.org/10.1016/S0009-2541(99)00106-0.

Ravikant, V., Wu, F., and Ji, W., 2009, Zircon U–Pb and Hf isotopic constraints on petrogenesis of the Cretaceous–Tertiary granites in eastern Karakoram and Ladakh, India: Lithos, v. 110, p. 153-166, https://doi.org/10.1016/j.lithos.2008.12.013.

Ridolfi, F., Renzulli, A., and Puerini, M., 2010, Stability and chemical equilibrium of amphibole in calc-alkaline magmas: an overview, new thermobarometric formulations and application to subduction-related volcanoes: Contributions to Mineralogy and Petrology, v. 160, p. 45-66, https://doi.org/10.1007/s00410-009-0465-7.

Robinson, A.C., Yin, A., Manning, C.E., Harrison, T.M., Zhang, S., and Wang, X., 2004, Tectonic evolution of the northeastern Pamir: Constraints from the northern portion of the Cenozoic Kongur Shan extensional system, western China: Geological Society of America Bulletin, v. 116, p. 953-973, https://doi.org/10.1130/B25375.1.

Robinson, A.C., Yin, A., Manning, C.E., Harrison, T.M., Zhang, S., and Wang, X., 2007, Cenozoic evolution of the eastern Pamir: Implications for strain-accommodation mechanisms at the western end of the Himalayan-Tibetan orogen: Geological Society of America Bulletin, v. 119, p. 882-896, https://doi.org/10.1130/B25981.1.

Robinson, A.C., Ducea, M., and Lapen, T.J., 2012, Detrital zircon and isotopic constraints on the crustal architecture and tectonic evolution of the northeastern

Pamir: Tectonics, v. 31, p. TC2016, https://doi.org/10.1029/2011TC003013.

Robinson, A.C., 2015, Mesozoic tectonics of the Gondwanan terranes of the Pamir plateau: Journal of Asian Earth Sciences, v. 102, p. 170-179, https://doi.org/10.1016/j.jseaes.2014.09.012.

Rollinson, H.R., 1993, Using geochemical data: Evaluation, presentation, interpretation: Pearson Education Limited, London, 56 p, https://doi.org/10.4324/9781315845548.

Rudnick, R.L., and Fountain, D.M., 1995, Nature and composition of the continental crust: a lower crustal perspective: Reviews of Geophysics, v. 33, p. 267-309, https://doi.org/10.1029/95RG01302.

Rudnick, R.L., and Gao, S., 2003, 3.01 - Composition of the continental crust. In: Holland, H.D., & Turekian, K.K., (eds.) Treatise on Geochemistry. Oxford: Pergamon, p. 1-64, https://doi.org/10.1016/B0-08-043751-6/03016-4.

Rutte, D., Ratschbacher, L., Schneider, S., Stübner, K., Stearns, M.A., Gulzar M.A., and Hacker, B.R., 2017, Building the Pamir-Tibetan Plateau—crustal stacking, extensional collapse, and lateral extrusion in the Central Pamir: 1. Geometry and kinematics: Tectonics, v. 36, p. 342-384, https://doi.org/10.1002/2016TC004293.

Schellart, W.P., 2020, Control of subduction zone age and size on flat slab subduction: Frontiers in Earth Science, v. 8, p. 26, https://doi.org/10.3389/feart.2020.00026.

Schmidt, J., Hacker, B.R., Ratschbacher, L., Stübner, K., Stearns, M., Kylander-Clark, A., Cottle, J.M., Alexander, A., Webb, G., Gehrels, G., and Minaev, V., 2011, Cenozoic deep crust in the Pamir: Earth and Planetary Science Letters, v. 312, p. 411-421, https://doi.org/10.1016/j.epsl.2011.10.034.

Schwab, M., Ratschbacher, L., Siebel, W., McWilliams, M., Minaev, V., Lutkov, V., Chen, F., Stanek, K., Nelson, B., Frisch, W., and Wooden, J.L., 2004, Assembly of the Pamirs: Age and origin of magmatic belts from the southern Tien Shan to the southern Pamirs and their relation to Tibet: Tectonics, v. 23, p. TC4002, https://doi.org/10.1029/2003TC001583.

Sekine, T., and Wyllie, P.J., 1982, Phase relationships in the system $KAlSiO_4$-Mg_2SiO_4-SiO_2-H_2O as a model for hybridization between hydrous siliceous melts and peridotite: Contributions to Mineralogy and Petrology, v. 79, p. 368-374, https://doi.org/10.1007/BF01132066.

Shervais, J.W., 2022, The petrogenesis of modern and ophiolitic lavas reconsidered: Ti-V and Nb-Th: Geoscience Frontiers, v. 13, p. 101319, https://doi.org/10.1016/j.gsf.2021.101319.

Shimoda, G., Tatsumi, Y., Nohda, S., Ishizaka, K., and Jahn, B.M., 1998, Setouchi high-Mg andesites revisited: geochemical evidence for melting of subducting sediments: Earth and Planetary Science Letters, v. 160, p. 479-492, https://doi.org/10.1016/S0012-821X(98)00105-8.

Soret, M., Larson, K.P., Cottle, J.M., Smit, M., Johnson, A., Shrestha, S., Ali, A., and Faisal, S., 2019, Mesozoic to Cenozoic tectono-metamorphic history of the South Pamir–Hindu Kush (Chitral, NW Pakistan): Insights from phase equilibria modelling, and garnet–monazite petrochronology: Journal of Metamorphic Geology, v. 37, p. 633-666, https://doi.org/10.1111/jmg.12479.

Sun, S.S., and McDonough, W.F., 1989, Chemical and isotopic systematics of oceanic basalts: implications for mantle compositions and processes: Geological Society, London, Special Publications, v. 42, p. 313-345, https://doi.org/10.1144/GSL.SP.1989.042.01.19.

Suo, Y.H., Li, S.Z., Jin, C., Zhang, Y., Zhou, J., Li, X.Y., Wang, P.C., Liu, Z., Wang, X.Y., and Somerville, I., 2019, Eastward tectonic migration and transition of the Jurassic-Cretaceous Andean-type continental margin along Southeast China: Earth-Science Review, v. 196, p. 102884, https://doi.org/10.1016/j.earscirev.2019.102884.

Sylvester, P.J., 1998, Post-collisional strongly peraluminous granites: Lithos, v. 45, p. 29-44, https://doi.org/10.1016/S0024-4937(98)00024-3.

Tang, Y.W., Chen, L., Zhao, Z.F., and Zheng, Y.F., 2019, Geochemical evidence for the production of granitoids through reworking of the juvenile mafic arc crust in the Gangdese orogen, southern Tibet: Geological Society of America Bulletin, v. 132, p. 1347-1364, https://doi.org/10.1130/B35304.1.

Tapponnier, P., Mattauer, M., Proust, F., and Cassaigneau, C., 1981, Mesozoic ophiolites, sutures, and large-scale tectonic movements in Afghanistan: Earth and Planetary Science Letters, v. 52, p. 355-371, https://doi.org/10.1016/0012-821X(81)90189-8.

Tatsumi, Y., 2001, Geochemical modeling of partial melting of subducting sediments and subsequent melt-mantle interaction: Generation of high-Mg andesites in the Setouchi volcanic belt, southwest Japan: Geology, v. 29, p. 323-326, https://doi.org/10.1130/0091-7613(2001)029<0323:GMOPMO>2.0.CO;2.

Tatsumi, Y., 2006, High-Mg andesites in the Setouchi volcanic belt, southwestern Japan: Analogy to Archean magmatism and continental crust formation? Annual Review of Earth and Planetary Sciences, v. 34, p. 467-499, https://doi.org/10.1146/annurev.earth.34.031405.125014.

Thompson, A.B., 1982, Dehydration melting of pelitic rocks and the generation of H_2O-undersaturated granitic liquids: American Journal of Science, v. 282, p. 1567-1595, https://doi.org/10.2475/ajs.282.10.1567.

Turner, S., Hawkesworth, C., Rogers, N., Bartlett, J., Worthington, T., Hergt, J., Pearce, J., and Smith, I., 1997, ^{238}U-^{230}Th disequilibria, magma petrogenesis, and flux rates beneath the depleted Tonga-Kermadec island arc: Geochimica et Cosmochimica Acta, v. 61, p. 4855-4884, https://doi.org/10.1016/S0016-7037(97)00281-0.

Valley, J.W., 2003, Oxygen isotopes in zircon: Reviews in Mineralogy and Geochemistry, v. 53, p. 343-385, https://doi.org/10.2113/0530343.

Valley, J.W., Lackey, J.S., Cavosie, A.J., Clechenko, C.C., Spicuzza, M.J., Basei, M.A.S., Bindeman, I.N., Ferreira, V.P., Sial, A.N., King, E.M., Peck, W.H., Sinha, A.K., and Wei, C.S., 2005, 4.4 billion years of crustal maturation: oxygen isotope ratios of magmatic zircon: Contributions to Mineralogy and Petrology, v. 150, p. 561-580, https://doi.org/10.1007/s00410-005-0025-8.

Vielzeuf, D., and Montel, J.M., 1994, Partial melting of metagreywackes. Part I. Fluid-absent experiments and phase relationships: Contributions to Mineralogy and Petrology, v. 117, p. 375-393, https://doi.org/10.1007/BF00307272.

Villarreal, D.P., Robinson, A.C., Chapman, J.B., Carrapa, B., Oimuhammadzoda, I., Gadoev, M., and Li, Y.P., 2023, Early Cretaceous displacement on the Tanymas thrust fault, Northern Pamir, Tajikistan, and regional tectonic implications: Journal of Asian Earth Sciences: X, v. 9, p. 100147, https://doi.org/10.1016/j.jaesx.2023.10014.

Wang, Q., Wyman, D.A., Xu, J., Dong, Y., Vasconcelos, P.M., Pearson, N., Wan, Y., Dong, H., Li, C., Yu, Y., Zhu, T., Feng, X., Zhang, Q., Zi, F., and Chu, Z., 2008., Eocene melting of subducting continental crust and early uplifting of central Tibet: evidence from central-western Qiangtang high-K calc-alkaline andesites, dacites and rhyolites: Earth and Planetary Science Letters, v. 272, p. 158–171, https://doi.org/10.1016/j.epsl.2008.04.034.

Whalen, J.B., Currie, K.L., and Chappell, B.W., 1987, A-type granites: Geochemical characteristics, discrimination and petrogenesis: Contributions to Mineralogy and Petrology, v. 95, p. 407-419, https://doi.org/10.1007/BF00402202.

Wyllie, P.J., 1979, Magmas and volatile components: American Mineralogist, v. 64, p. 469-500.

Wyllie, P.J., and Sekine, T., 1982, The formation of mantle phlogopite in subduction zone hybridization: Contributions to Mineralogy and Petrology, v. 79, p. 375-380, https://doi.org/10.1007/BF01132067.

Wood, B.J., and Turner, S.P., 2009, Origin of primitive high-Mg andesite: Constraints from natural examples and experiments: Earth and Planetary Science Letters, v. 283, p. 59-66, https://doi.org/10.1016/j.epsl.2009.03.032.

Workman, R.K., and Hart, S.R., 2005, Major and trace element composition of the depleted MORB mantle (DMM): Earth and Planetary Science Letters, v. 231, p. 53-72, https://doi.org/10.1016/j.epsl.2004.12.005.

Workman, R.K., Eiler, J.M., Hart, S.R., and Jackson, M.G., 2008, Oxygen isotopes in Samoan lavas: Confirmation of continent recycling: Geology, v. 36, p. 551-554, https://doi.org/10.1130/G24558A.1.

Xiang, H., and Connolly, J.A.D., 2022, GeoPS: An interactive visual computing tool for thermodynamic modelling of phase equilibria: Journal of Metamorphic

Geology, v. 40, p. 243-255, https://doi.org/10.1111/jmg.12626.

Xiao, W.J., Song, D.F., Zhang, J.E., Mao, Q.G., Ao, S.J., Han, C.M., Wan, B., and Zhang, Z.Y., 2022, Anatomy of the structure and evolution of subduction zones and research prospects: Earth Science, v. 47, p. 3073-3106, https://doi.org/10.3799/dqkx.2022.380.

Xu, Y.G., Menzies, M.A., Thirlwall, M.F., and Xie, G.H., 2001, Exotic lithosphere mantle beneath the western Yangtze craton: Petrogenetic links to Tibet using highly magnesian ultrapotassic rocks: Geology, v. 29, p. 863-866, https://doi.org/10.1130/0091-7613(2001)029<0863:ELMBTW>2.0.CO;2.

Yin, A., and Harrison, T.M., 2000, Geologic evolution of the Himalayan-Tibetan Orogen: Annual Review Earth and Planetary Sciences, v. 28, p. 211-280.

Yogodzinski, G.M., Volynets, O.N., Koloskov, A.V., Seliverstov, N.I., and Matvenkov, V.V., 1994, Magnesian Andesites and the Subduction Component in a Strongly Calc-Alkaline Series at Piip Volcano, Far Western Aleutians: Journal of Petrology, v. 35, p. 163-204, https://doi.org/10.1093/petrology/35.1.163.

Zanchetta, S., Worthington, J., Angiolini, L., Leven, E.J., Villa, I.M., and Zanchi, A., 2018, The Bashgumbaz Complex (Tajikistan): Arc obduction in the Cimmerian orogeny of the Pamir: Gondwana Research, v. 57, p. 170-190, https://doi.org/10.1016/j.gr.2018.01.009.

Zanchi, A., Poli, S., Fumagalli, P., Gaetani, M., Khan, M.A., Treloar, P.J., Searle, M.P., and Jan, M.Q., 2000, Mantle exhumation along the Tirich Mir Fault Zone, NW Pakistan: pre-mid-Cretaceous accretion of the Karakoram terrane to the Asian margin, Tectonics of the Nanga Parbat Syntaxis and the Western Himalaya, 170*170, Geological Society of London, p. 0, https://doi.org/10.1144/GSL.SP.2000.170.01.13.

Zanchi, A., and Gaetani, M., 2011, The geology of the Karakoram range, Pakistan: the new 1:100,000 geological map of Central-Western Karakoram: Italian Journal of Geosciences, v. 130, p. 161-262, https://doi.org/10.3301/IJG.2011.09.

Zhang, C.L., Zou, H.B., Ye, X.T., and Chen, X.Y., 2018, A newly identified Precambrian terrane at the Pamir Plateau: The Archean basement and

Neoproterozoic granitic intrusions: Precambrian Research, v. 304, p. 73-87, https://doi.org/10.1016/j.precamres.2017.11.006.

Zhang, C.L., Zou, H.B., and Liu, X.Q., 2022, Cretaceous basalt-andesite sequence in the Southern Pamir: arc—back-arc architecture at the Pamir Plateau genetically related to the northward flat subductions of the Neo-Tethys Ocean: Lithos, v. 422-423, p. 106747, https://doi.org/10.1016/j.lithos.2022.106747.

Zhu, D.C., Wang, Q., Chung, S.L., Cawood, P.A., and Zhao, Z., 2019, Gangdese magmatism in southern Tibet and India–Asia convergence since 120 Ma: Geological Society, London, Special Publications, v. 483, p. 583-604., https://doi.org/10.1144/SP483.14.

Zindler, A., and Hart, S.R., 1986, Chemical geodynamics: Annual Review of Earth and Planetary Sciences, v. 14, p. 493-571, https://doi.org/10.1146/annurev.ea.14.050186.002425.

Figure captions

Figure 1. (a) Regional tectonic map, showing the geographic location of the Pamir (after Burtman and Molnar, 1993; Yin and Harrison, 2000); (b) Simplified tectonic map of the Pamir, showing distribution of tectonic terranes and plutons (Modified from Robinson, 2015; Aminov et al., 2017; Zanchetta et al., 2018); (c) Simplified geological map of Kalaqigu pluton at the Chinese Wakhan Corridor, Southern Pamir. IYSZ–Indus-Tsangpo Suture Zone; KKF–Karakorum Fault; MPT–Main Pamir Thrust; RPSZ–Rushan-Pshart Suture Zone; SSZ–Shyok Suture Zone; TSZ–Tanymas Suture Zone; WTBZ–Wakhan-Tirich Boundary Zone.

Figure 2. Representative thin section photomicrographs of Kalaqigu diorite (a-b) and monzogranite (c-d). Figures (a) and (c) are under cross-polarized light and Figures (b) and (d) are under the plane-polarized light. Amp—amphibole; Bi—biotite; Chl—chlorite; Crd—cordierite; Kfs—K-feldspar; Pl—plagioclase; Q—quartz; Sil—sillimanite.

Figure 3. Concordia diagrams with representative zircon CL images for LA-ICP-MS zircon analyses of Kalaqigu diorite (a) and monzogranite (b). (c) Histogram of U-Pb ages for inherited zircon cores from the studied monzogranite; (d) Representative cathodoluminescence (CL) images of zircon cores from the studied monzogranite. The data sources for detrital zircons of southeastern Pamir are from Imrecke et al. (2019).

Figure 4. (a-b) Classification diagrams for amphiboles (Leake et al., 1997; Hawthorne and Oberti, 2007). (c) Mg vs. (Al^{VI}+Fe^{3+}+Ti) vs. (Fe^{2+}+Mn) ternary diagram for biotite (Foster, 1960). (d) Or–Ab–An classification diagram for plagioclase (modified after Deer et al. 1992). An = anorthite, And = andesine, Ab = albite, By = bytownite, La = labradorite, Ol = oligoclase, Or = orthoclase.

Figure 5. Geochemical classification and major element geochemical features for the Kalaqigu diorites and monzogranites. (a) TAS classification diagram (Middlemost, 1994); (b) K_2O versus Na_2O diagram (Rollinson, 1993); (c) K_2O versus Na_2O diagram (Le Maitre, 1989); (d) A/NK versus A/CNK diagram (Maniar and Piccoli, 1989).

Figure 6. Chondrite-normalized REE patterns (a and c) and primitive mantle-normalized multi-element patterns (b and d) for the Kalaqigu diorites and monzogranites. Chondrite and primitive mantle values are from Sun and Mcdonough (1989).

Figure 7. (a) $\varepsilon_{Nd}(t)$ versus $(^{87}Sr/^{86}Sr)_i$; $(^{207}Pb/^{204}Pb)_i$ (b) and $(^{208}Pb/^{204}Pb)_i$ (c) versus $(^{206}Pb/^{204}Pb)_i$ diagrams for the Kalaqigu diorites and monzogranites. The depleted MORB-source mantle (DMM) shown is from Workman and Hart (2005). The Archean basement is from Ji et al., (2011). Cretaceous basalt-andesite, diorites and

granitoids from the Chinese Wakhan Corridor are shown for comparison (Jiang et al., 2014; Li et al., 2016; Liu et al., 2020; Zhang et al., 2022). The Northern Hemisphere Reference Line (NHRL) is from Hart, (1984). EMI, EMII and GLOSS are from Hart (1988), Zindler and Hart (1986) and Plank and Langmuir (1998), respectively.

Figure 8. Oxygen isotope data for zircon from the Kalaqigu diorite and monzogranites. The mantle values of zircon oxygen isotope (5.3 ± 0.6 ‰, 2SD) are from Valley (2003).

Figure 9. (a) $MgO/(MgO + FeO^T)$ versus TiO_2, and (b) Y versus Sr/Y discrimination diagrams (after Kamei et al., 2004). (c) 10,000 Ga/Al versus Nb, and (d) (Zr + Nb + Ce + Y) versus FeO^T/MgO (Whalen et al., 1987). FG—fractionated M-, I-, and S-type granite; OGT—unfractionated M-, I-, and S-type granite.

Figure 10. (a) $Mg^\#$ versus SiO_2 (after Rapp et al., 1999; Martin et al., 2005); (b-f) Fenner diagrams showing selected major elements variations for the Kalaqigu diorites. The green and blue lines represent crystallization trends defined by major element modelling using Rhyolite-MELTS, divided into olivine + orthopyroxene and clinopyroxene + spinel steps. Diorites samples WK1616-2 with lowest contents of SiO_2 and WK1616-4 with highest MgO have been taken as primary melts (Supplementary Table 3). The model was run at 5.16 kbar with H_2O_{melt} = 5.84 wt.%, calculated from amphibole compositions (Supplementary Table 2).

Figure 11. (a) Rb/Ba versus Rb/Sr, showing geochemical compositions of magma source for the Kalaqigu diorites and monzogranites. The mixing curve between the basalt- and pelite-derived melts is from Sylvester (1998); (b) Th/La versus Th/Sm. N-MORB (normal mid-oceanic-ridge basalt) and OIB (oceanic-island basalt) values are from Sun and McDonough (1989), and the values for average GLOSS are after Plank and Langmuir (1998). The curve shows different mixing ratios between partial melt (4%) of the GLOSS average and N-MORB. The D_{Th} and D_{La} are 0.16 and 1.2,

respectively (Plank, 2005). We use the same D as La for Sm (D_{Sm} = 1.2). (c) Ba/Th versus $(La/Sm)_N$ and (d) Th/Yb versus Ba/La discrimination diagrams for metasomatic agents added to the mantle wedge. Taxkorgan S-type granites in (a) are from Jiang et al. (2014) and Li et al. (2019). Cretaceous mantle-derived magmatic rocks (i.e., basalt-andesite and diorite) with MgO > 3% from Chinese Wakhan Corridor are shown for comparison (Li et al., 2016; Liu et al., 2020; Zhang et al., 2022). Data of sanukitic HMAs in Figures (c) and (d) are from Hanyu et al. (2006) and Tatsumi (2006).

Figure 12. Dy/Yb versus La/Yb (a) and Rb/Sr versus Ba/Rb (b) diagrams. All the mantle models in (a) are from Xu et al. (2001). Amphibole and phlogopite arrows in (b) refer to these as residual phases in the source region (Furman and Graham, 1999). Cretaceous mantle-derived magmatic rocks are those shown in Fig. 11.

Figure 13. Plots of Al_2O_3 + MgO + FeO^T + TiO_2 versus Al_2O_3/(MgO+ FeO^T + TiO_2) (a); Na_2O + K_2O + FeO^T + MgO + TiO_2 versus (Na_2O + K_2O)/(FeO^T + MgO + TiO_2) (b); Na_2O/K_2O versus FeO^T (c) and CaO + FeO^T + MgO + TiO_2 versus CaO/(FeO^T + MgO + TiO_2) (d) (a–d are after Patiño Douce, 1999). (e–f) Plots of Rb/Sr ratios versus Sr (ppm) and Ba (ppm), respectively (after Inger and Harris, 1993). Taxkorgan S-type granites in (a–d) are shown in Fig. 13.

Figure 14. (a) Pressure-temperature (P-T) pseudosection calculated for metagreywacke from Vielzeuf and Montel. (1994). Yellow circle represents P-T conditions calculated from biotite compositions (Li and Zhang, 2022; Supplementary Table 2). Bi—biotite; Crd—cordierite; Gt—garnet; Ilm—ilmenite; Kfs—K-feldspar; Ms—muscovite; Opx—orthopyroxene; Pl—plagioclase; q—quartz; ru—rutile; sill—sillimanite. (b–c) Isomodes of biotite, plagioclase, H_2O_{Bt}, garnet, cordierite and K-feldspar in different intervals, indicating growth of garnet, cordierite and K-feldspar at the expense of biotite and plagioclase during melting as P-T increases.

Figure 15. (a) Rb versus (Y + Nb) diagrams (after Pearce et al., 1984); (b) Th/Yb versus Nb/Yb and (c) Th/Nb versus Ti/V diagrams (after Shervais, 2022); (d) Histogram of zircon U-Pb ages. VAG—volcanic arc granites; syn-COLG—syn-collisional granites; WPG—within-plate granites; ORG—ocean-ridge granites. Cretaceous mantle-derived magmatic rocks and granitoids are shown in Figs. 11. Cretaceous granitoids from the Chinese Wakhan Corridor in (b-c) are also shown for comparison (Jiang et al., 2014; Li et al., 2016; Liu et al., 2020). Taxkorgan S-type granites are from Jiang et al. (2014), Li et al. (2019) and Ma et al. (2023). Teshiktash-Beik volcanic rocks, northwest of Chinese Wakhan Corridor, are from Aminov et al. (2017).

Figure 16. Schematic diagram showing the Cretaceous multi-stage and multi-source processes for the architecture of the continental arc of the South Pamir. (a) Northward low-angle and flat-slab subduction of the Neo-Tethys oceanic lithosphere resulted in the generation of Cretaceous granitoids. (b) Continuous flat-slab subduction of the Neo-Tethys oceanic lithosphere prompted sedimentary melts to metasomatize the mantle, produced mantle-derived magmatic rocks. The figures also show Early Cretaceous crustal shortening and thickening events in the Central Pamir and South Pamir. The Neo-Tethys oceanic slab may undergo slab roll-back in the Late Cretaceous (<90 Ma) (Chapman et al., 2018a).

Figure 1

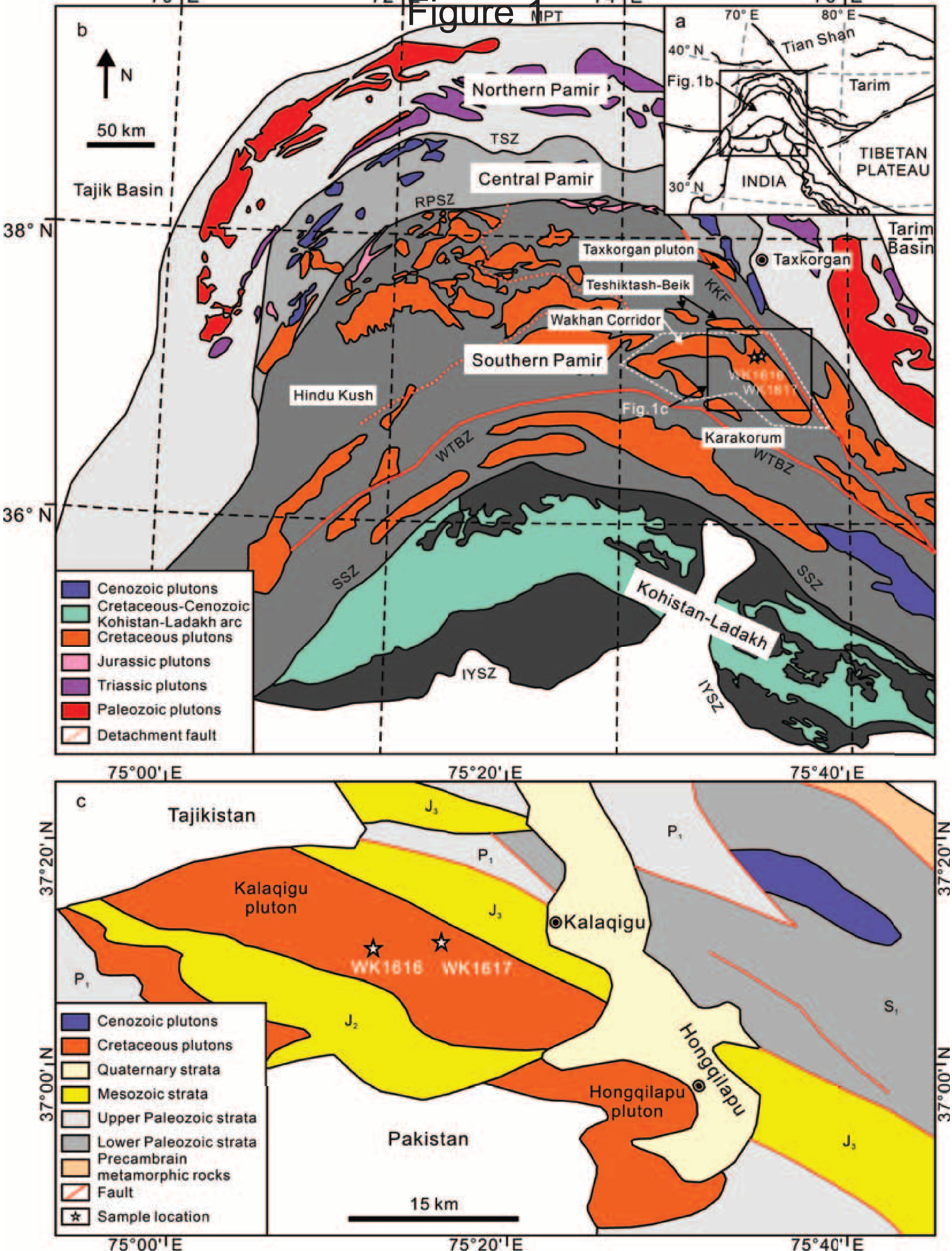

b
N
50 km
Northern Pamir
Central Pamir
Southern Pamir
Tajik Basin
MPT
TSZ
RPSZ
Taxkorgan pluton
Teshiktash-Beik
Wakhan Corridor
Taxkorgan
KKF
Tarim Basin
Hindu Kush
WK1616
WK1617
Fig.1c
Karakorum
WTBZ
SSZ
IYSZ
Kohistan-Ladakh
38° N
36° N
70° E
72° E
74° E
76° E
a
Tian Shan
Fig.1b
Tarim
TIBETAN PLATEAU
INDIA
40° N
30° N
80° E
Cenozoic plutons
Cretaceous-Cenozoic Kohistan-Ladakh arc
Cretaceous plutons
Jurassic plutons
Triassic plutons
Paleozoic plutons
Detachment fault
c
75°00' E
75°20' E
75°40' E
37°20' N
37°00' N
Tajikistan
Pakistan
Kalaqigu pluton
Kalaqigu
Hongqilapu pluton
Hongqilapu
WK1616
WK1617
15 km
Cenozoic plutons
Cretaceous plutons
Quaternary strata
Mesozoic strata
Upper Paleozoic strata
Lower Paleozoic strata
Precambrain metamorphic rocks
Fault
Sample location

Figure 2

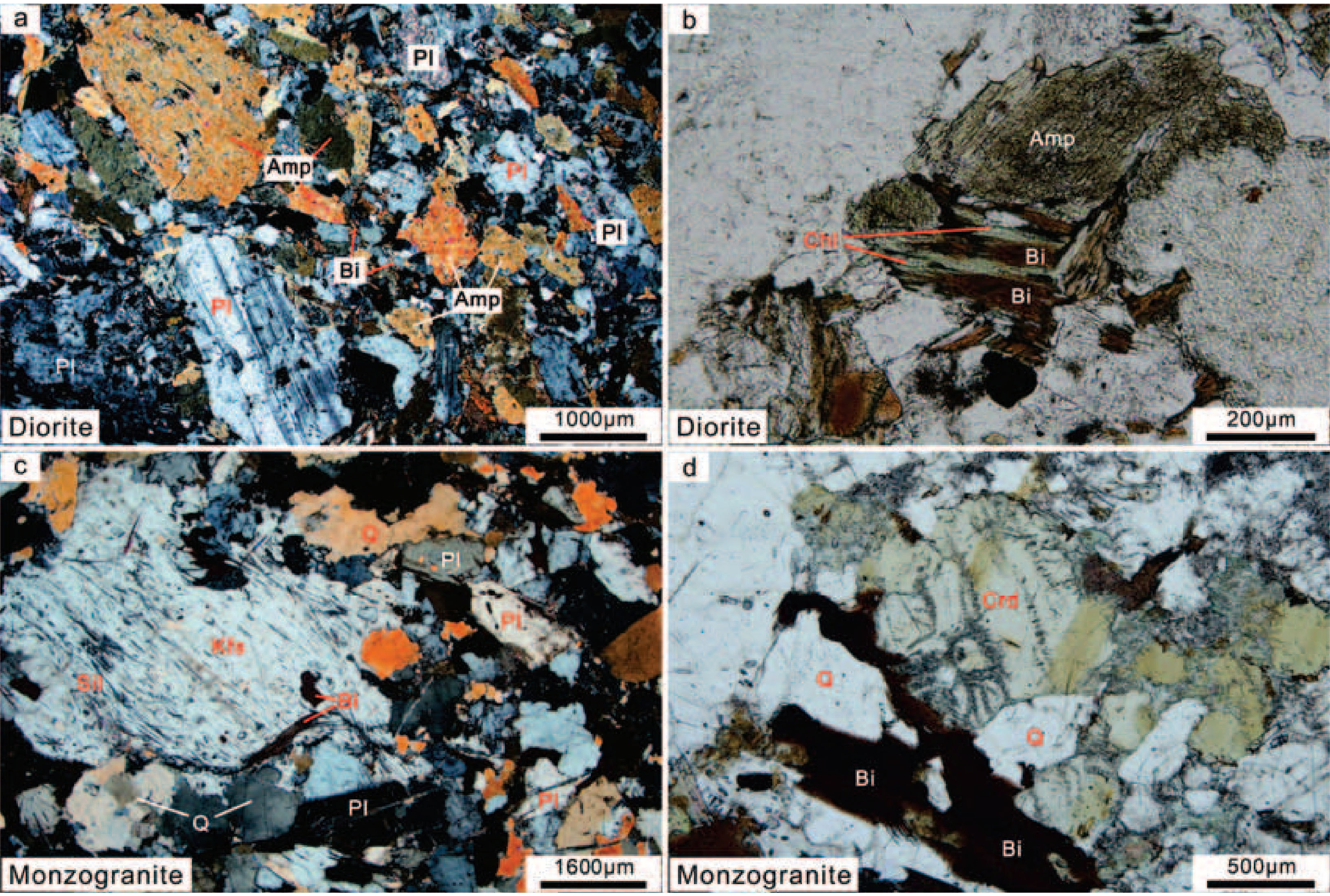

a
Pl
Amp
Pl
Pl
Bi
Amp
Pl
Pl
Diorite
1000μm
b
Amp
Chl
Bi
Bi
Diorite
200μm
c
Q
Pl
Pl
Kfs
Sil
Bi
Q
Pl
Pl
Monzogranite
1600μm
d
Crd
Q
Q
Bi
Bi
Monzogranite
500μm

Figure 3

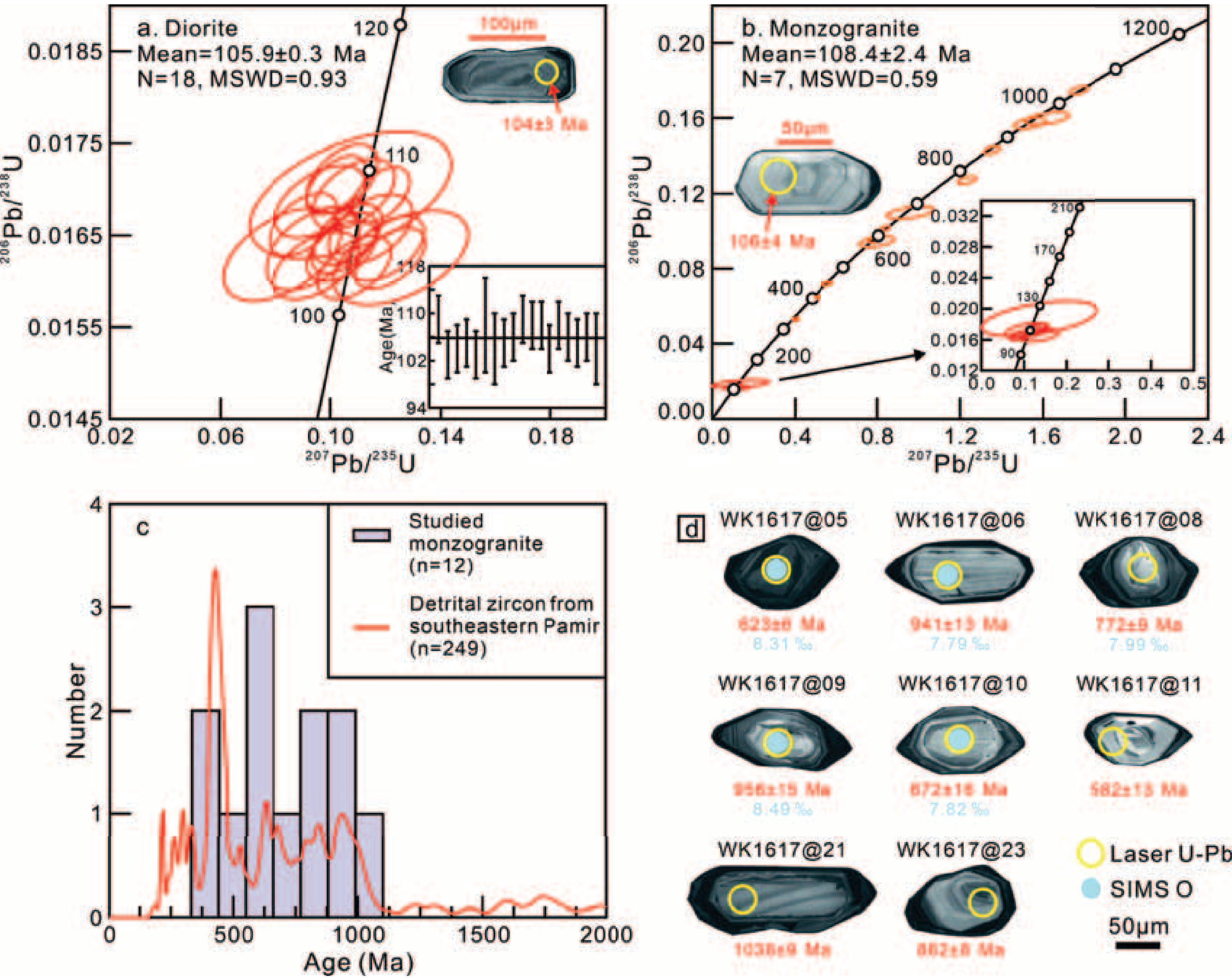
a. Diorite
Mean=105.9±0.3 Ma
N=18, MSWD=0.93
100μm
104±3 Ma
Age(Ma)
$^{206}Pb/^{238}U$
$^{207}Pb/^{235}U$
b. Monzogranite
Mean=108.4±2.4 Ma
N=7, MSWD=0.59
50μm
106±4 Ma
c
Studied monzogranite (n=12)
Detrital zircon from southeastern Pamir (n=249)
Number
Age (Ma)
d
WK1617@05
623±6 Ma
8.31 ‰
WK1617@06
941±13 Ma
7.79 ‰
WK1617@08
772±9 Ma
7.99 ‰
WK1617@09
956±15 Ma
8.49 ‰
WK1617@10
672±16 Ma
7.82 ‰
WK1617@11
582±13 Ma
WK1617@21
1038±9 Ma
WK1617@23
862±8 Ma
Laser U-Pb
SIMS O
50μm

Figure 4

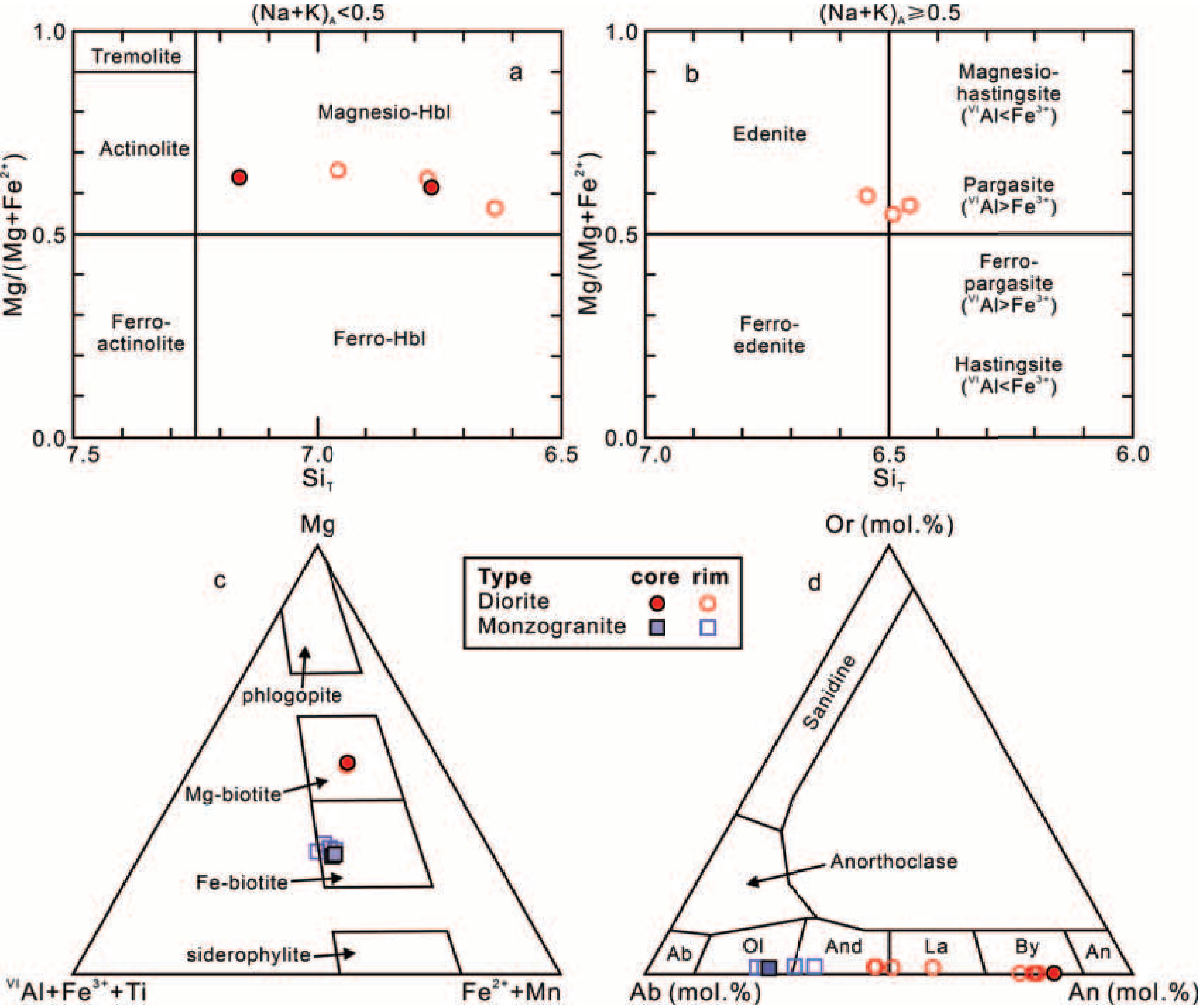

(Na+K)A<0.5
a
Tremolite
Actinolite
Magnesio-Hbl
Ferro-actinolite
Ferro-Hbl
Mg/(Mg+Fe2+)
SiT
1.0
0.5
0.0
7.5
7.0
6.5
(Na+K)A≥0.5
b
Edenite
Magnesio-hastingsite (VIAl<Fe3+)
Pargasite (VIAl>Fe3+)
Ferro-pargasite (VIAl>Fe3+)
Ferro-edenite
Hastingsite (VIAl<Fe3+)
6.0
Mg
c
phlogopite
Mg-biotite
Fe-biotite
siderophylite
VIAl+Fe3++Ti
Fe2++Mn
Type core rim
Diorite
Monzogranite
Or (mol.%)
d
Sanidine
Anorthoclase
Ab
Ol
And
La
By
An
Ab (mol.%)
An (mol.%)

Figure 5

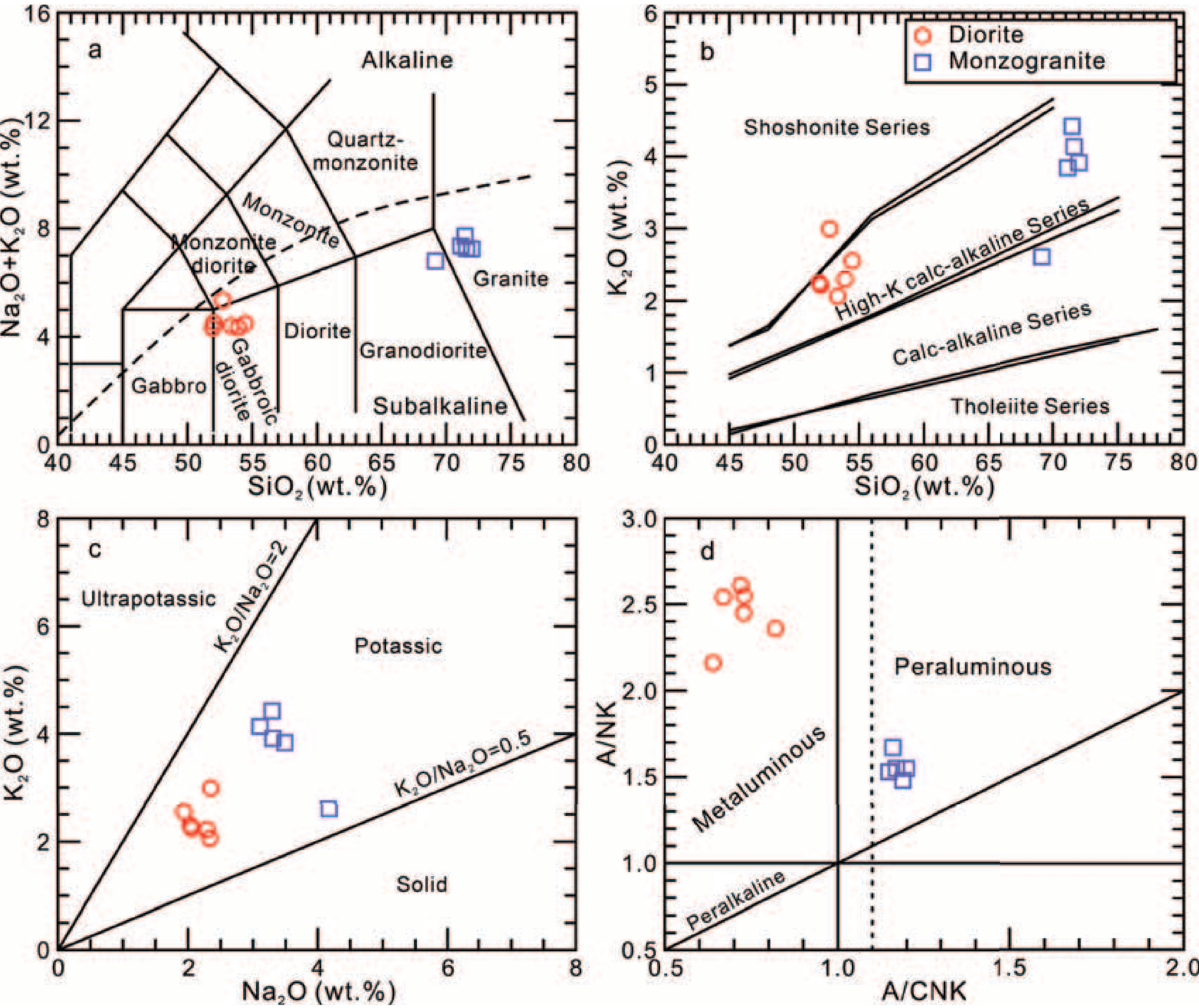

a
Alkaline
Quartz-monzonite
Monzonite
Monzonite diorite
Diorite
Granodiorite
Granite
Gabbro
Gabbroic diorite
Subalkaline
Na2O+K2O (wt.%)
SiO2 (wt.%)
b
Diorite
Monzogranite
Shoshonite Series
High-K calc-alkaline Series
Calc-alkaline Series
Tholeiite Series
K2O (wt.%)
SiO2 (wt.%)
c
Ultrapotassic
K2O/Na2O=2
Potassic
K2O/Na2O=0.5
Solid
K2O (wt.%)
Na2O (wt.%)
d
Peraluminous
Metaluminous
Peralkaline
A/NK
A/CNK

Figure 6

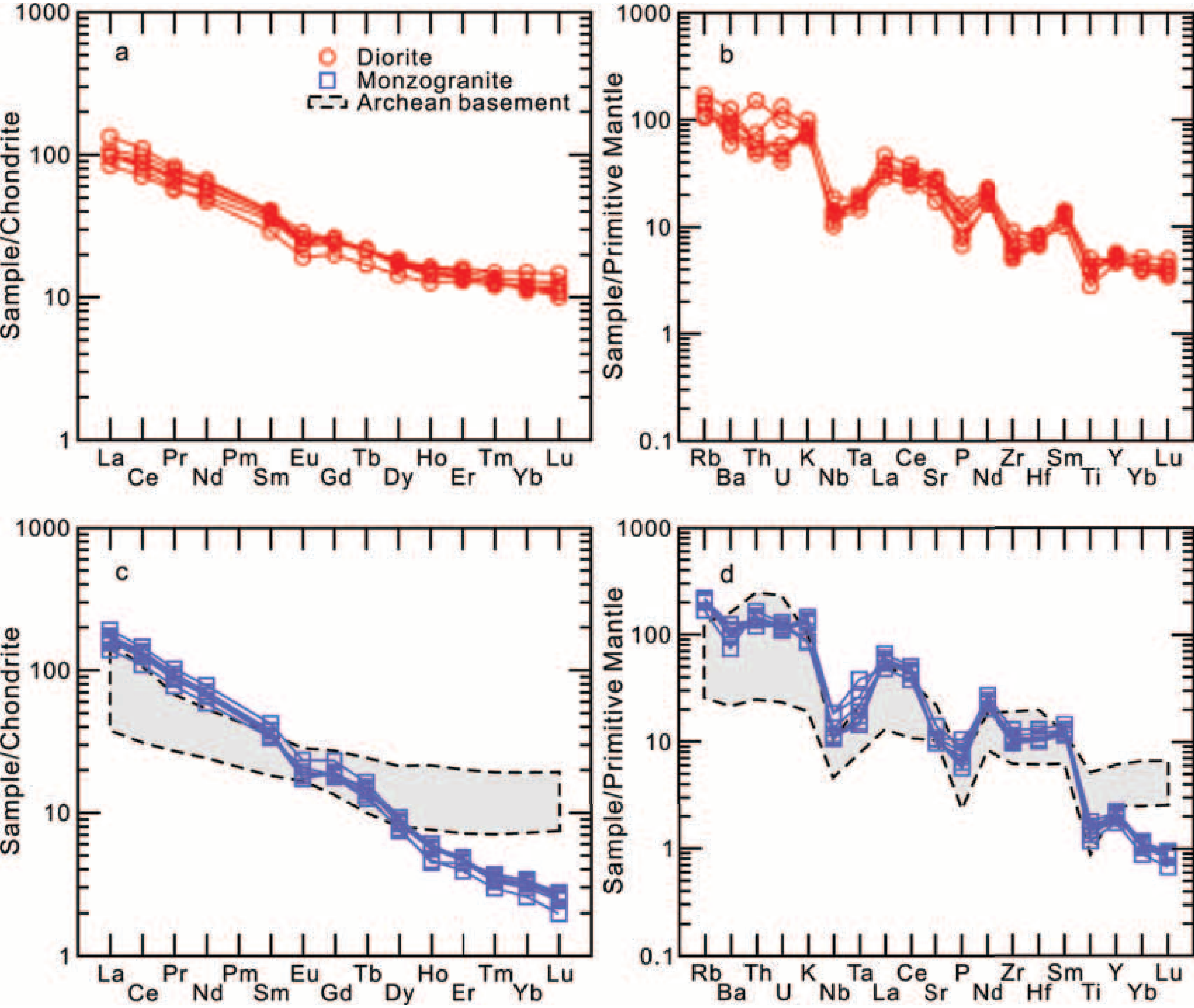

a
Diorite
Monzogranite
Archean basement
Sample/Chondrite
1000
100
10
1
La
Ce
Pr
Nd
Pm
Sm
Eu
Gd
Tb
Dy
Ho
Er
Tm
Yb
Lu
b
Sample/Primitive Mantle
1000
100
10
1
0.1
Rb
Ba
Th
U
K
Nb
Ta
La
Ce
Sr
P
Nd
Zr
Hf
Sm
Ti
Y
Yb
Lu
c
d

Figure 7

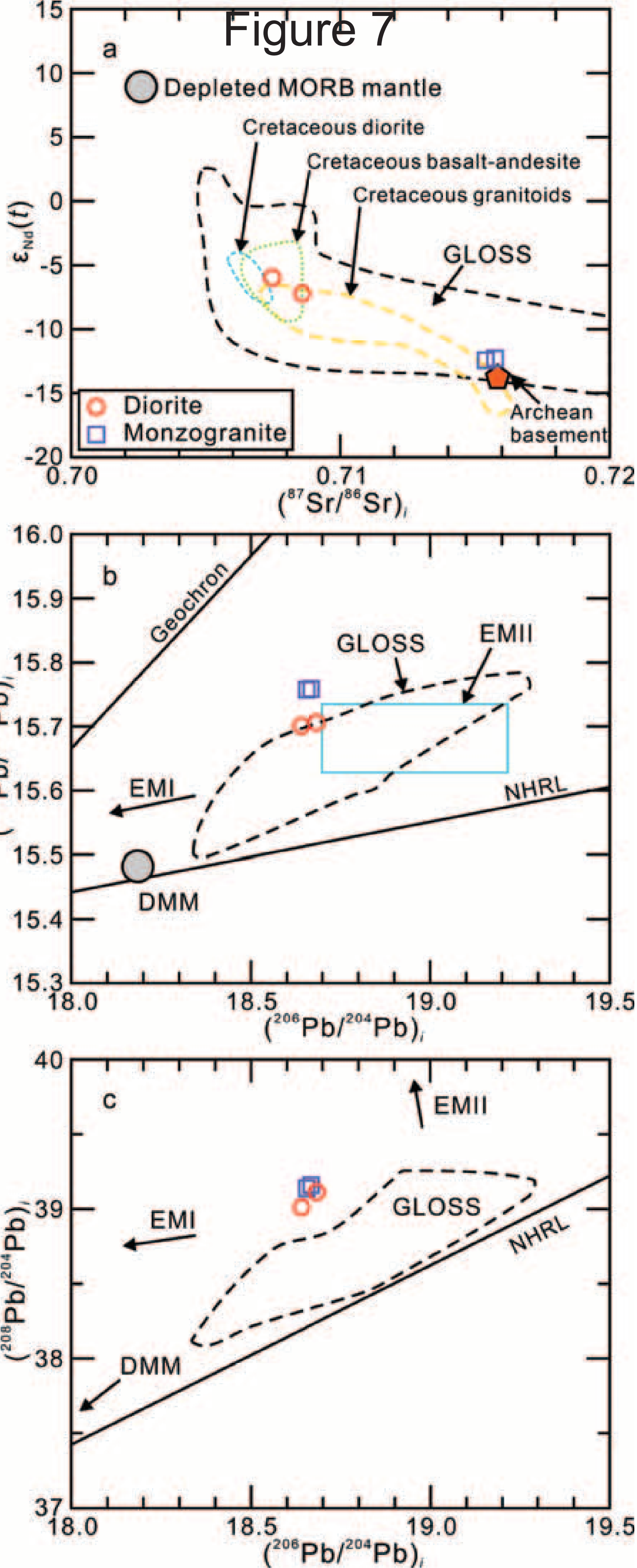

a
Depleted MORB mantle
Cretaceous diorite
Cretaceous basalt-andesite
Cretaceous granitoids
GLOSS
Archean basement
Diorite
Monzogranite
$\varepsilon_{Nd}(t)$
$(^{87}Sr/^{86}Sr)_i$
b
Geochron
GLOSS
EMII
EMI
NHRL
DMM
$(^{207}Pb/^{204}Pb)_i$
$(^{206}Pb/^{204}Pb)_i$
c
EMII
EMI
GLOSS
NHRL
DMM
$(^{208}Pb/^{204}Pb)_i$
$(^{206}Pb/^{204}Pb)_i$

Figure 8

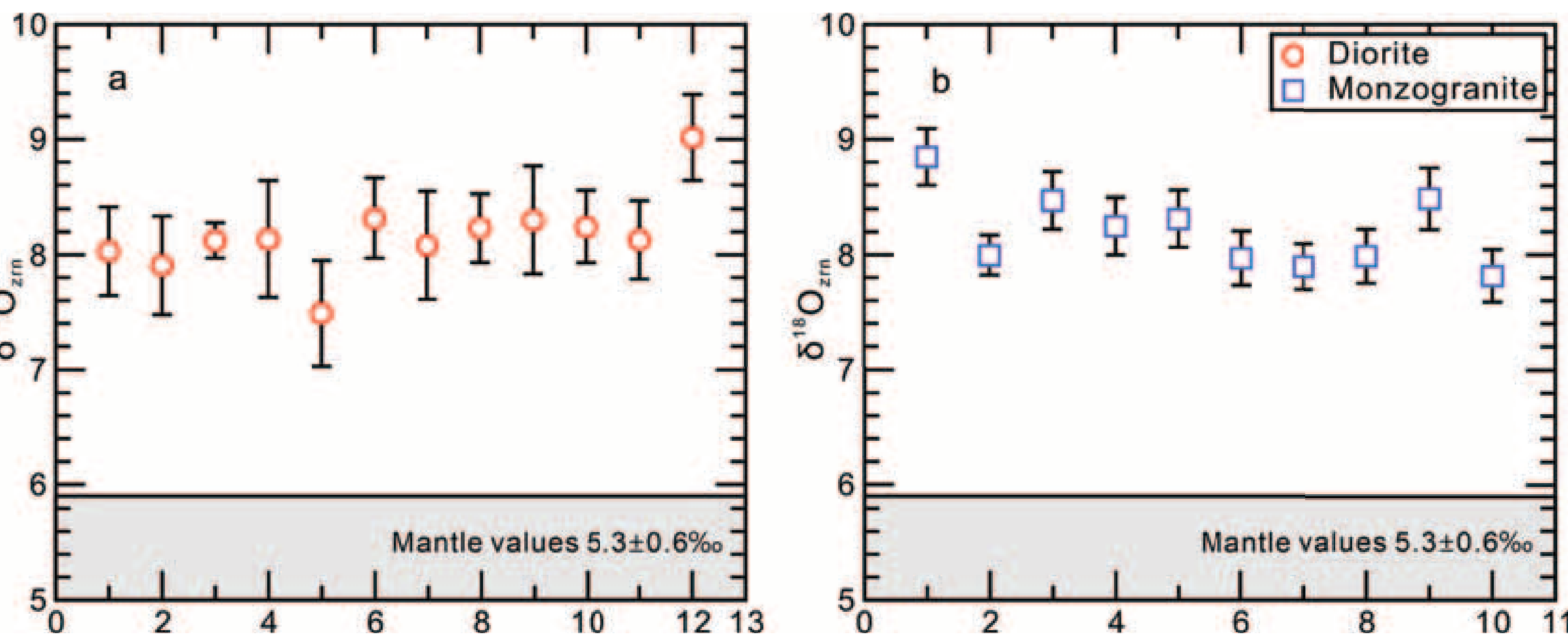
a
b
Diorite
Monzogranite
$\delta^{18}O_{zrn}$
Mantle values 5.3±0.6‰
10
9
8
7
6
5
0
2
4
6
8
10
12
13
11

Figure 9

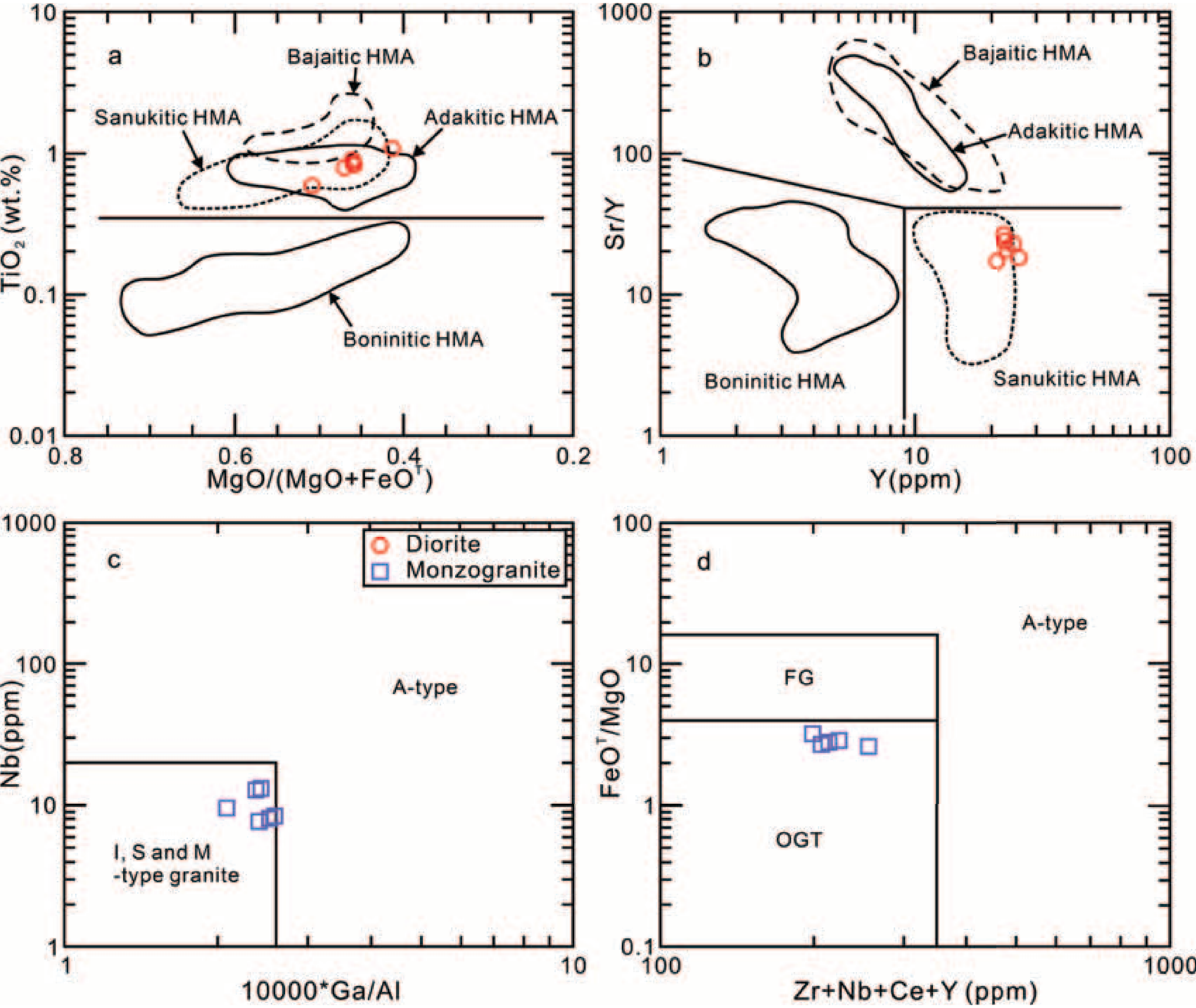

a
Bajaitic HMA
Sanukitic HMA
Adakitic HMA
Boninitic HMA
TiO2 (wt.%)
MgO/(MgO+FeO^T)
b
Bajaitic HMA
Adakitic HMA
Boninitic HMA
Sanukitic HMA
Sr/Y
Y(ppm)
c
Diorite
Monzogranite
A-type
I, S and M
-type granite
Nb(ppm)
10000*Ga/Al
d
A-type
FG
OGT
FeO^T/MgO
Zr+Nb+Ce+Y (ppm)

Figure 10

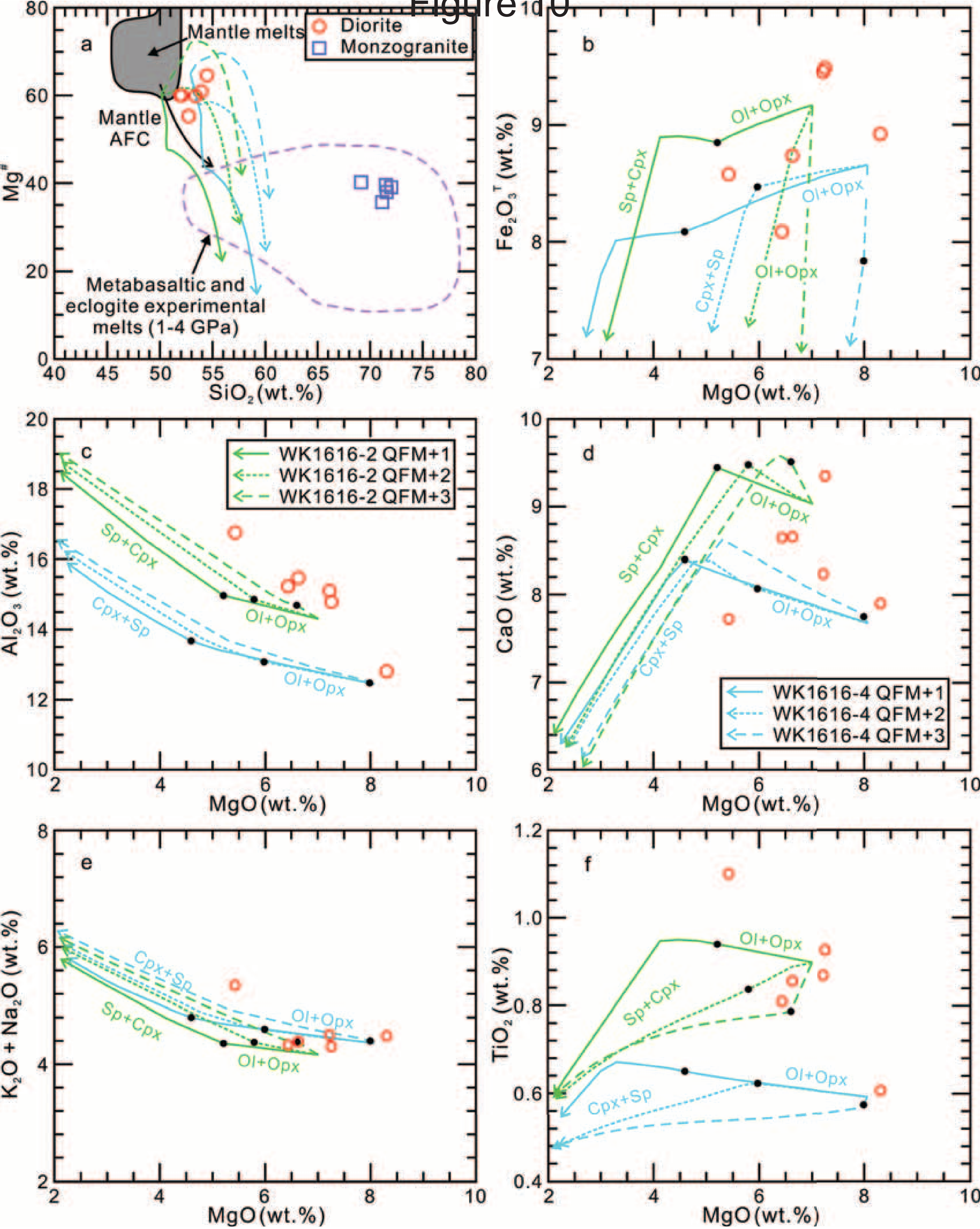

a
Mantle melts
Diorite
Monzogranite
Mantle AFC
Metabasaltic and eclogite experimental melts (1-4 GPa)
Mg#
SiO2 (wt.%)
b
Ol+Opx
Sp+Cpx
Cpx+Sp
Fe2O3T (wt.%)
MgO (wt.%)
c
WK1616-2 QFM+1
WK1616-2 QFM+2
WK1616-2 QFM+3
Al2O3 (wt.%)
d
WK1616-4 QFM+1
WK1616-4 QFM+2
WK1616-4 QFM+3
CaO (wt.%)
e
K2O + Na2O (wt.%)
f
TiO2 (wt.%)

Figure 11

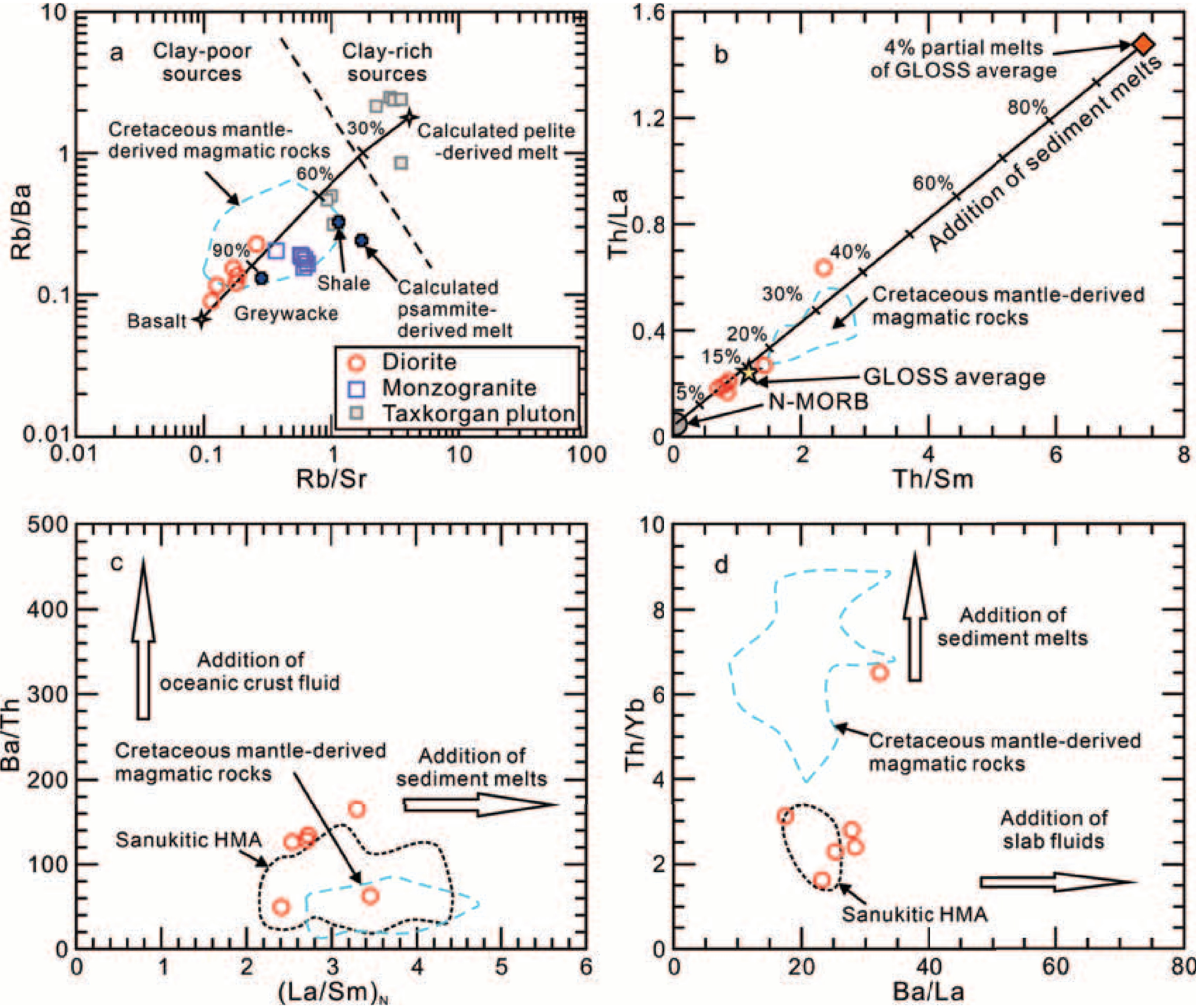

a
Clay-poor sources
Clay-rich sources
Cretaceous mantle-derived magmatic rocks
30%
60%
90%
Calculated pelite -derived melt
Shale
Calculated psammite-derived melt
Basalt
Greywacke
Diorite
Monzogranite
Taxkorgan pluton
Rb/Ba
Rb/Sr
b
4% partial melts of GLOSS average
80%
60%
40%
30%
20%
15%
5%
Addition of sediment melts
Cretaceous mantle-derived magmatic rocks
GLOSS average
N-MORB
Th/La
Th/Sm
c
Addition of oceanic crust fluid
Cretaceous mantle-derived magmatic rocks
Addition of sediment melts
Sanukitic HMA
Ba/Th
(La/Sm)N
d
Addition of sediment melts
Cretaceous mantle-derived magmatic rocks
Addition of slab fluids
Sanukitic HMA
Th/Yb
Ba/La

Figure 12

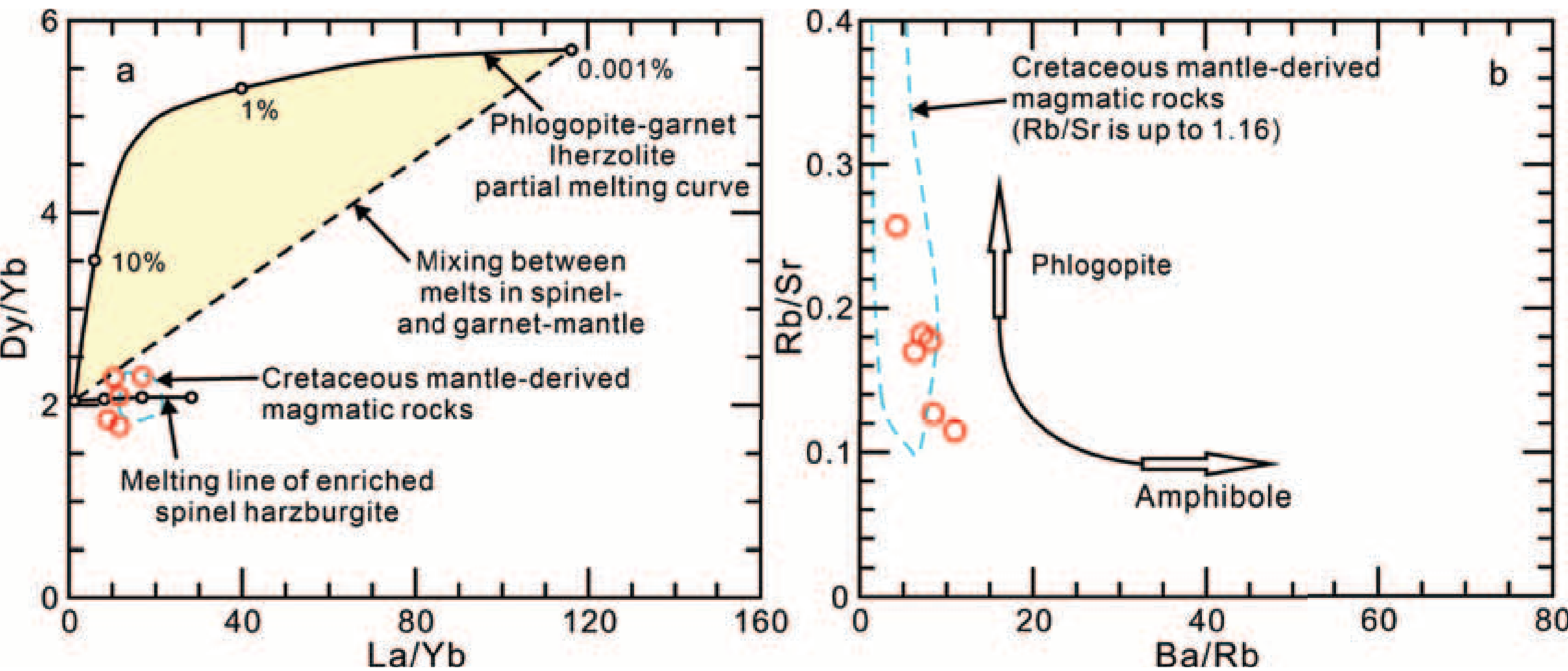

a
0.001%
1%
10%
Phlogopite-garnet lherzolite partial melting curve
Mixing between melts in spinel- and garnet-mantle
Cretaceous mantle-derived magmatic rocks
Melting line of enriched spinel harzburgite
Dy/Yb
La/Yb
0
2
4
6
0
40
80
120
160
b
Cretaceous mantle-derived magmatic rocks (Rb/Sr is up to 1.16)
Phlogopite
Amphibole
Rb/Sr
Ba/Rb
0
0.1
0.2
0.3
0.4
0
20
40
60
80

Figure 13

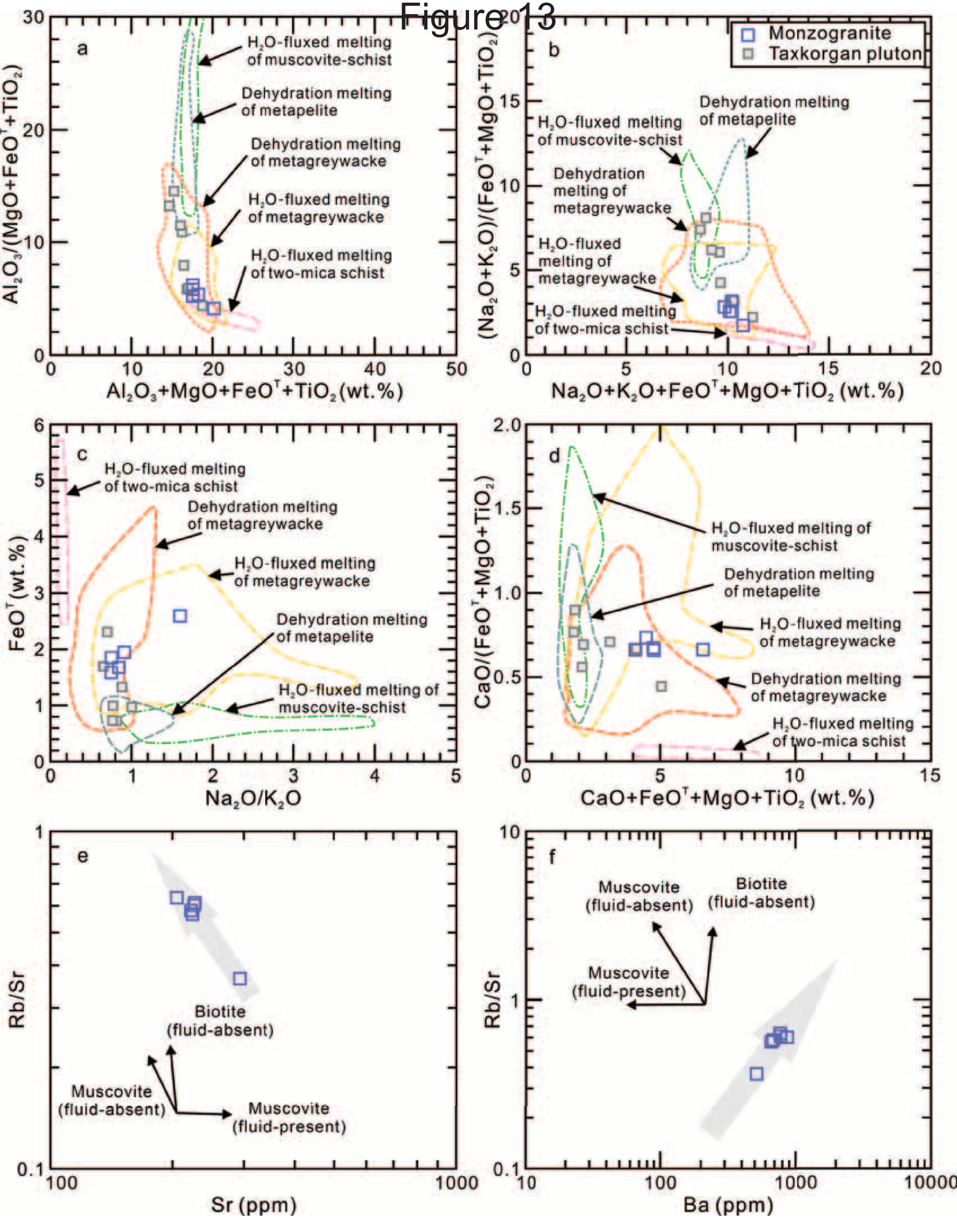

a
b
c
d
e
f
Monzogranite
Taxkorgan pluton
H2O-fluxed melting of muscovite-schist
Dehydration melting of metapelite
Dehydration melting of metagreywacke
H2O-fluxed melting of metagreywacke
H2O-fluxed melting of two-mica schist
Al2O3/(MgO+FeOT+TiO2)
Al2O3+MgO+FeOT+TiO2 (wt.%)
(Na2O+K2O)/(FeOT+MgO+TiO2)
Na2O+K2O+FeOT+MgO+TiO2 (wt.%)
FeOT (wt.%)
Na2O/K2O
CaO/(FeOT+MgO+TiO2)
CaO+FeOT+MgO+TiO2 (wt.%)
Rb/Sr
Sr (ppm)
Ba (ppm)
Biotite (fluid-absent)
Muscovite (fluid-absent)
Muscovite (fluid-present)

Figure 14

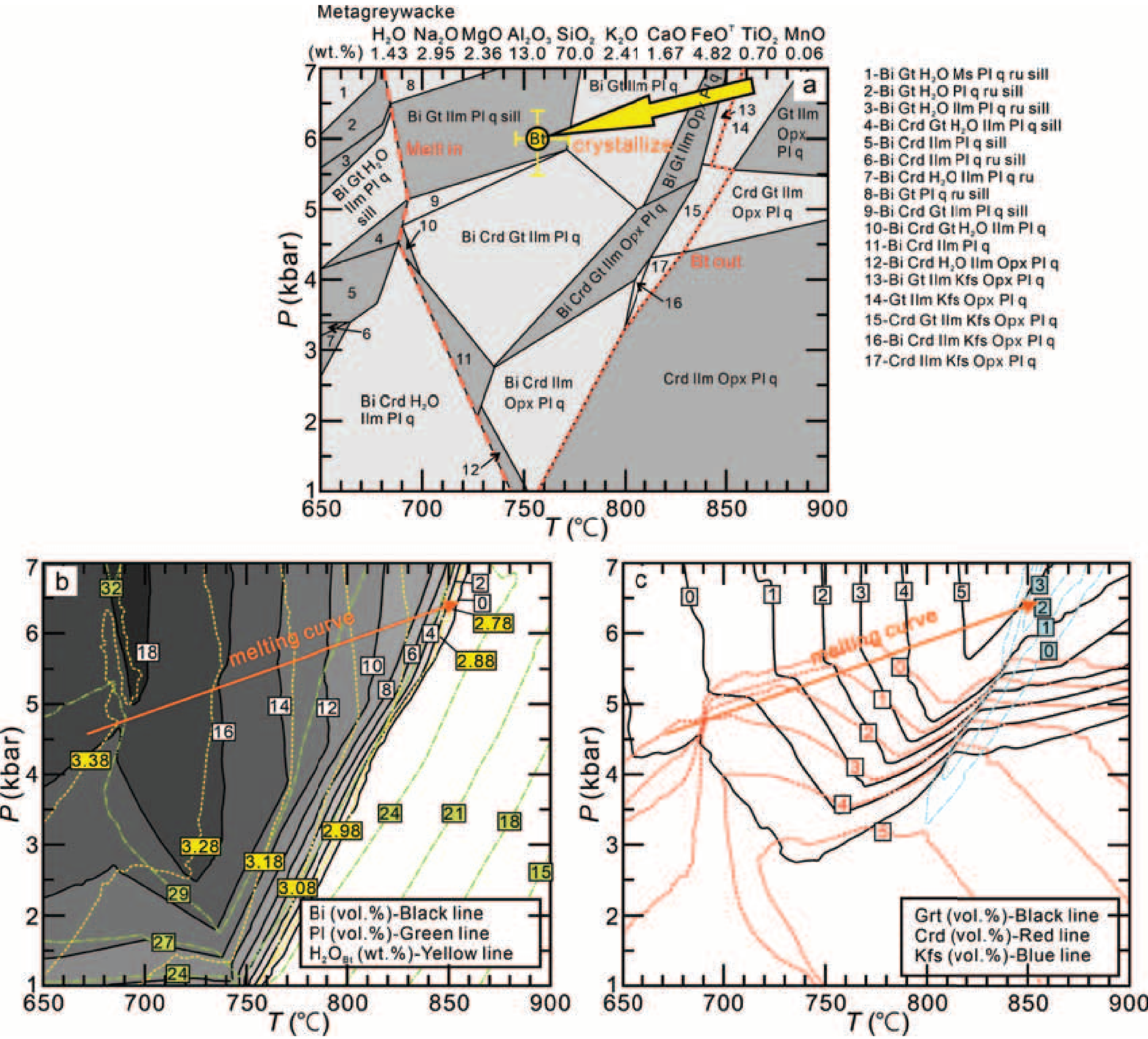

Metagreywacke
(wt.%) H2O 1.43 Na2O 2.95 MgO 2.36 Al2O3 13.0 SiO2 70.0 K2O 2.41 CaO 1.67 FeOT 4.82 TiO2 0.70 MnO 0.06
a
Bi Gt Ilm Pl q sill
Bi Gt Ilm Pl q
Melt in
crystallize
Bi Crd Gt Ilm Pl q
Bi Gt H2O Ilm Pl q sill
Bi Crd H2O Ilm Pl q
Bi Crd Ilm Opx Pl q
Crd Ilm Opx Pl q
Bi Crd Gt Ilm Opx Pl q
Bi Gt Ilm Opx Pl q
Gt Ilm Opx Pl q
Crd Gt Ilm Opx Pl q
Bt out
P (kbar)
T (°C)
1-Bi Gt H2O Ms Pl q ru sill
2-Bi Gt H2O Pl q ru sill
3-Bi Gt H2O Ilm Pl q ru sill
4-Bi Crd Gt H2O Ilm Pl q sill
5-Bi Crd Ilm Pl q sill
6-Bi Crd Ilm Pl q ru sill
7-Bi Crd H2O Ilm Pl q ru
8-Bi Gt Pl q ru sill
9-Bi Crd Gt Ilm Pl q sill
10-Bi Crd Gt H2O Ilm Pl q
11-Bi Crd Ilm Pl q
12-Bi Crd H2O Ilm Opx Pl q
13-Bi Gt Ilm Kfs Opx Pl q
14-Gt Ilm Kfs Opx Pl q
15-Crd Gt Ilm Kfs Opx Pl q
16-Bi Crd Ilm Kfs Opx Pl q
17-Crd Ilm Kfs Opx Pl q
b
melting curve
Bi (vol.%)-Black line
Pl (vol.%)-Green line
H2OBt (wt.%)-Yellow line
c
melting curve
Grt (vol.%)-Black line
Crd (vol.%)-Red line
Kfs (vol.%)-Blue line

Figure 15

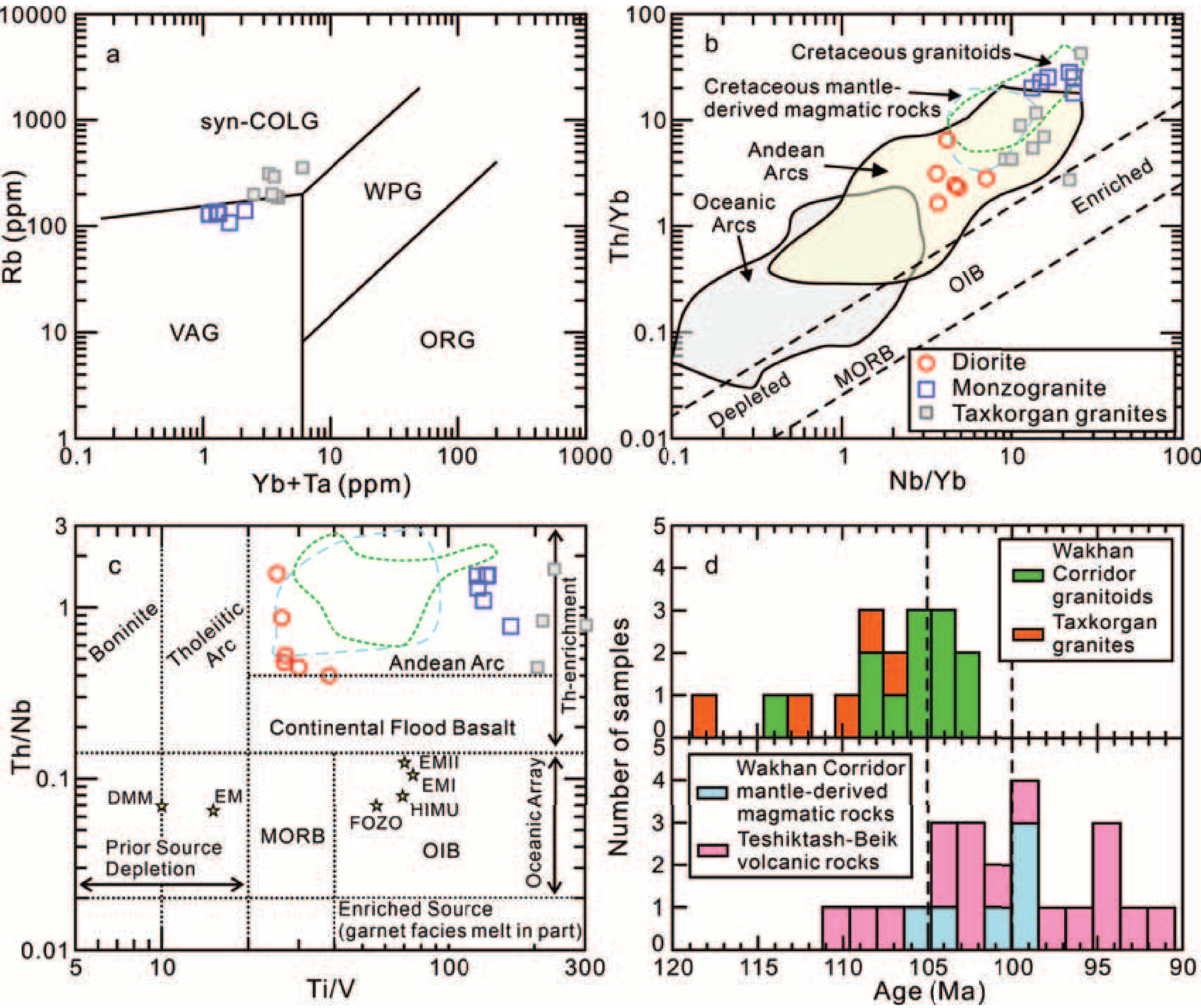
a
syn-COLG
WPG
VAG
ORG
Rb (ppm)
Yb+Ta (ppm)
b
Cretaceous granitoids
Cretaceous mantle-derived magmatic rocks
Andean Arcs
Oceanic Arcs
Enriched
OIB
MORB
Depleted
Th/Yb
Nb/Yb
Diorite
Monzogranite
Taxkorgan granites
c
Boninite
Tholeiitic Arc
Andean Arc
Continental Flood Basalt
Th-enrichment
Oceanic Array
DMM
EM
EMII
EMI
HIMU
FOZO
MORB
OIB
Prior Source Depletion
Enriched Source (garnet facies melt in part)
Th/Nb
Ti/V
d
Wakhan Corridor granitoids
Taxkorgan granites
Wakhan Corridor mantle-derived magmatic rocks
Teshiktash-Beik volcanic rocks
Number of samples
Age (Ma)

Figure 16

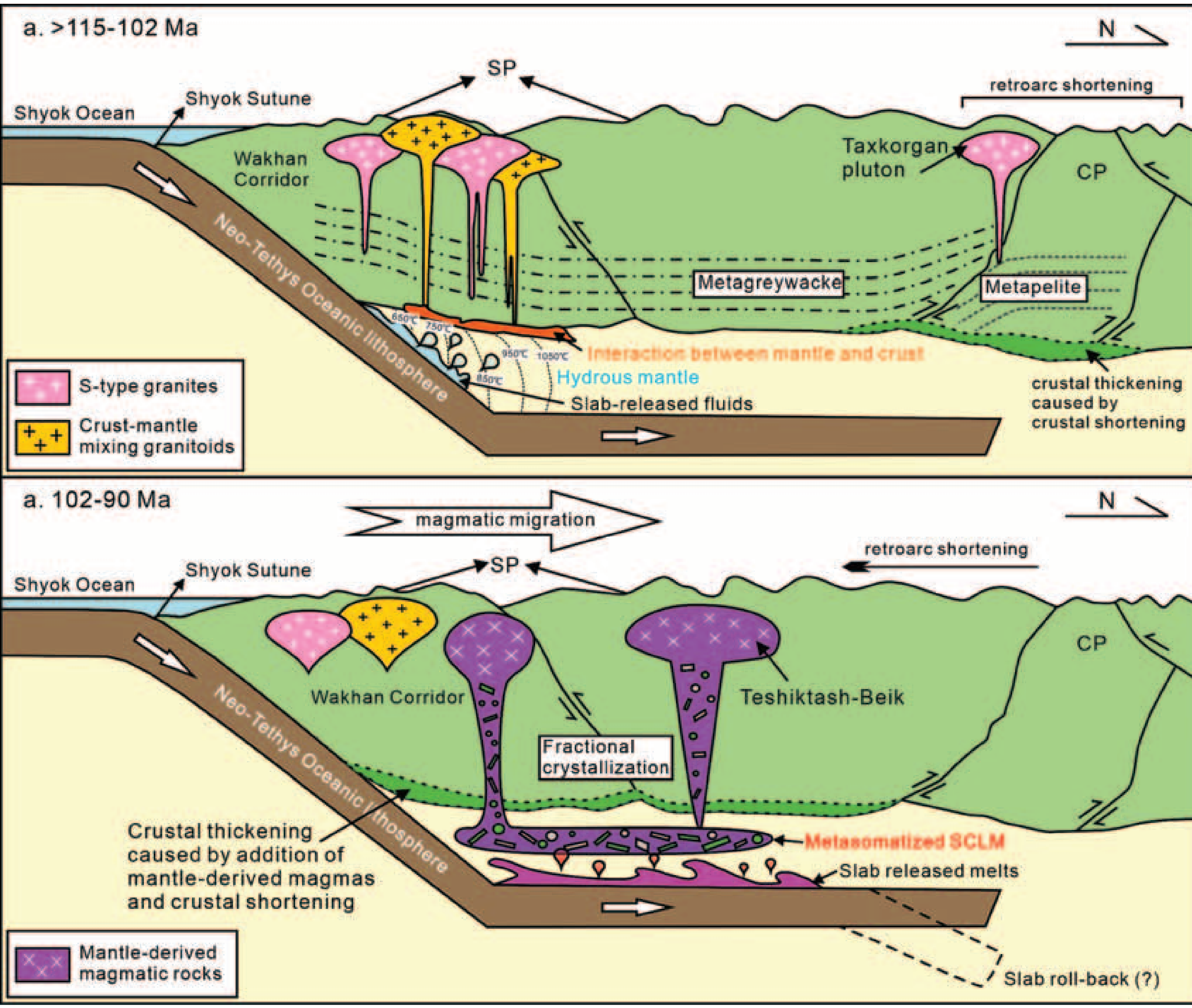

a. >115-102 Ma
N
SP
retroarc shortening
Shyok Sutune
Shyok Ocean
Wakhan Corridor
Taxkorgan pluton
CP
Neo-Tethys Oceanic lithosphere
Metagreywacke
Metapelite
650℃
750℃
850℃
950℃
1050℃
Interaction between mantle and crust
Hydrous mantle
Slab-released fluids
crustal thickening caused by crustal shortening
S-type granites
Crust-mantle mixing granitoids
a. 102-90 Ma
magmatic migration
N
retroarc shortening
SP
Shyok Sutune
Shyok Ocean
CP
Wakhan Corridor
Teshiktash-Beik
Neo-Tethys Oceanic lithosphere
Fractional crystallization
Crustal thickening caused by addition of mantle-derived magmas and crustal shortening
Metasomatized SCLM
Slab released melts
Slab roll-back (?)
Mantle-derived magmatic rocks

Supporting Information for

Early Cretaceous continental arc magmatism in the Wakhan Corridor, South Pamir: mantle evolution and geodynamic processes during flat subduction of the Neo-Tethys oceanic slab

Fang Yang[1, 2], Jiyuan Yin [2*], Wenjiao Xiao [3], Mike Fowler [4], Andrew C. Kerr [5], Zaili Tao [2], Wen Chen [2], Yuelong Chen[1]

[1] School of Earth Sciences and Resources, China University of Geosciences, Beijing, 100083, China

[2] Institute of Geology, Chinese Academy of Geological Sciences, Beijing 100037, China

[3] Xinjiang Institute of Ecology and Geography, Chinese Academy of Sciences, Urumqi, 830011, China

[4] School of the Environment, Geography and Geosciences, University of Portsmouth, Burnaby Building, Burnaby Road, Portsmouth PO1 3QL, UK

[5] School of Earth and Environmental Sciences, Cardiff University, Cardiff, Wales CF10 3AT, United Kingdom

***Corresponding authors:**

Email: yinjiyuan1983@163.com (J. Yin)

Data Repository

Supplementary File 1. Analytical methods

Supplementary Table 1. LA-ICP-MS zircon U-Pb isotopic dating data for the Kalaqigu diorite and monzogranite at the Chinese Wakhan Corridor, Southern Pamir

Supplementary Table 2. Representative electron probe analyses of amphibole, biotite and plagioclase from the Kalaqigu pluton

Supplementary Table 3. Whole-rock major (wt.%), trace (ppm) elements and Sr-Nd-Pb isotopic compositions of Kalaqigu diorite and monzogranite at the Chinese Wakhan Corridor and Taxkorgan S-type monzogranites

Supplementary Table 4. Zircon Lu-Hf isotopic compositions of Kalaqigu diorite at the Chinese Wakhan Corridor, Southern Pamir

Supplementary Table 5. Zircon O isotopic compositions of Kalaqigu diorite and monzogranite at the Chinese Wakhan Corridor, Southern Pamir

Supplementary File 1 Analytical methods

Zircon U-Pb geochronology

Zircon grains for U-Pb and Lu-Hf analysis were separated using conventional magnetic and heavy-liquid techniques, followed by hand-picking under a binocular microscope at the MC-ICPMS laboratory of the Institute of Geology and Geophysics, Chinese Academy of Sciences (IGG CAS). Photographs were taken in transmitted and reflected light, followed by cathodoluminescence (CL) imaging to reveal the internal texture of the grains and to select suitable positions for U-Pb dating and Hf isotope analysis.

Zircon U-Pb dating of two samples (WK1616 and WK1617) were carried out using LA-ICP-MS (Laser Ablation Inductively Coupled Plasma Mass Spectrometry). An Agilent 7500a ICP-MS and a Neptune multi-collector (MC-ICPMS with an attached 193 nm excimer ArF laser-ablation system (GeoLas Plus)) were used for simultaneous determination of zircon U-Pb ages. Instrumental settings and detailed analytical procedures for laser ablation system, ICP-MS instrument and data reduction have been described in Xie et al. (2008). Analyses were acquired at a beam diameter of 32 μm, an 8 Hz repetition rate, and an energy of 10–20 J/cm^2. Helium carrier gas transported the ablated sample materials from the laser-ablation cell via a mixing chamber to the ICPMS. Every spot analysis consisted of ~30 s background acquisition and 40 s sample data acquisition. The zircons 91500 and GJ-1 were used as an external standard and internal standard, respectively. The glass NIST 610 was used as an external standard for trace element compositions calibration. Off-line raw data selection, integration of background and analytical signals, time-drift correct, and quantitative calibration of U-Pb isotopes were performed using ICPMSDataCal software (Liu et al., 2009). Concordia diagrams and weighted mean calculations were made using ISOPLOT 3.00 program (Ludwig, 2003).

Zircon Lu-Hf isotope analysis

Zircons showing concordant U-Pb ages were selected for in-situ zircon Lu-Hf isotopes in the same dated domains. They were subsequently analyzed using Laser Ablation (LA)-ICPMS at the MC-ICPMS laboratory of IGG CAS, using a beam size of 60 μm (8 Hz laser pulse frequency). Details of instrumental conditions and data acquisition have been given in Wu et al. (2006). During the analytical period, a weighted $^{206}Pb/^{238}U$ age and a weighted $^{176}Hf/^{177}Hf$ ratio of the sample GJ-1 were determined at 609.7 ± 6.3 Ma (2σ, MSWD = 0.97, n = 12) and 0.282015 ± 0.000003 (2σ, MSWD = 1.12, n = 94), which are in good agreement with the recommended U-Pb age and Hf isotopic ratios (Black et al., 2003; Wu et al., 2006). The $^{176}Hf/^{177}Hf$ ratios of the standard zircon (MUD) were measured to be 0.282504 ± 0.000003 (2σ, MSWD = 0.71, n = 82), and it was used for data acquisition of Hf isotopes.

Zircon O isotope analysis

Zircon oxygen isotopes were measured using the Cameca IMS-1280 HR secondary ion mass spectrometer (SIMS) at the at State Key Laboratory of Isotope Geochemistry (SKLaBIG), Guangzhou Institute of Geochemistry, Chinese Academy of Sciences (GIG CAS). Detailed analytical procedures are described in Li et al. (2010a) and Yang et al. (2018). The measured oxygen isotopic values were corrected for instrumental mass fractionation factor (IMF) using the standard Penglai zircon with $\delta^{18}O_{VSMOW}$ = 5.3 ± 0.10 ‰ (2σ) and Qinghu standards with 5.4 ± 0.2 ‰ (2σ) (Li et al., 2010b). The internal precision of single analysis was better than 0.1‰ (1σ) for $\delta^{18}O$ values. Uncertainties of analytical $\delta^{18}O$ values are quoted at 2σ level. The external precision (0.50‰; 2SD, n = 68), measured by spot-to-spot reproducibility of repeated analyses of the PengLai standard, was adopted for data evaluation.

Mineral geochemistry analysis

Major elements analyses of amphibole, plagioclase and biotite were carried out using JEOL JXA-8100 Electron Probe Micro Analyzer (EPMA) at IGG CAS. A beam current of 20 nA at 15 kV accelerating voltage, a beam size of 5 μm and a counting time of 30 s were used to analyze minerals. The analytical precision for all elements is better than 1.5%.

Whole-rock geochemistry analysis

Representative samples selected on the basis of optical microscopy were cleaned, crushed and homogenization, and then powdered to ~200-mesh size using an agate mill. The resulting powder was used for analyses of major and trace elements, and Sr-Nd-Pb isotopes. Determination of loss on ignition (LOI) was performed at 1000 °C. Major-element oxides were analyzed using a Rigaku RIX 2000 X-ray fluorescence spectrometer (XRF) on fused glass beads at SKLaBIG, GIG CAS. Details of procedures are described by Yuan et al. (2010). Analytical uncertainty for major elements is generally < 5%

Trace element concentrations, including rare earth element (REE) concentrations, were determined using a Perkin-Elmer ELAN-DRC-e inductively coupled plasma mass spectrometer at the State Key Laboratory of Ore Deposit Geochemistry (SKLOG), with analytical uncertainty better than 10%. The analytical precision is generally better than 5% for most trace elements. The analytical procedures for the trace elements were described in detail in Liang et al. (2000).

Whole-rock Sr-Nd-Pb isotope analysis

Sr-Nd-Pb isotopic compositions of selected samples were determined using a MC-ICP-MS at SKLaBIG, GIG CAS. Sr and Nd were separated using cation columns, and Nd fractions were further separated by HDEHP-coated Kef columns. Analytical procedures are similar to those described in Wei et al. (2002) and Li et al. (2004). The $^{87}Sr/^{86}Sr$ ratio of the NBS987 standard and $^{143}Nd/^{144}Nd$ ratio of the Shin Etsu Jndi-1 standard measured are 0.710285 ± 15 (2σ) and 0.512085 ± 10 (2σ), respectively. Measured $^{87}Sr/^{86}Sr$ and $^{143}Nd/^{144}Nd$ ratios were corrected for fractionation using ratios of $^{87}Sr/^{86}Sr$ = 0.1194 and $^{143}Nd/^{144}Nd$ = 0.7219, respectively. A total of 50 mg powder was weighed into a Teflon beaker and dissolved in concentrated HF at 180 °C for 3 days to determinate Pb isotope. Lead was separated and purified by conventional cation-exchange techniques with diluted HBr as an eluant. Analytical procedures for

Pb isotopic compositions were described in Zhu et al. (2001). Pb isotope fractionations were corrected using correction factors based on replicate analyses of international standard NBS981. The results measured for NBS981 are 0.059135 ± 0.021% (2σ) for $^{204}Pb/^{206}Pb$, 0.914174 ± 0.010% (2σ) for $^{207}Pb/^{206}Pb$, and 2.161430 ± 0.016% (2σ) for $^{208}Pb/^{206}Pb$.

REFERENCES CITED

Black, L.P., Kamo, S.L., Allen, C.M., Aleinikoff, J.N., Davis, D.W., Korsch, R.J., and Foudoulis, C., 2003, TEMORA 1: a new zircon standard for Phanerozoic U-Pb geochronology: Chemical Geology, v. 200, p. 155-170,, https://doi.org/10.1016/S0009-2541(03)00165-7.

Li, X.H., Liu, D.Y., Sun, M., Li, W.X., Liang, X.R., and Liu, Y., 2004, Precise Sm–Nd and U–Pb isotopic dating of the supergiant Shizhuyuan polymetallic deposit and its host granite, SE China: Geological Magazine, v. 141, p. 225-231, https://doi.org/10.1017/S0016756803008823.

Li, X.H., Li, W.X., Li, Q.L., Wang, X.C., Liu, Y., and Yang, Y.H., 2010a, Petrogenesis and tectonic significance of the 850 Ma Gangbian alkaline complex in South China: Evidence from in situ zircon U-Pb dating, Hf-O isotopes and whole-rock geochemistry: Lithos, v. 114, p. 1-15,, https://doi.org/10.1016/j.lithos.2009.07.011.

Li, X.H., Long, W.G., Li, Q.L., Liu, Y., Zheng, Y.F., Yang, Y.H., Chamberlain, K.R., Wan, D.F., Guo, C.F., and Wang, X.C., 2010b, Penglai zircon megacrysts: a potential new working reference material for microbeam determination of Hf–O isotopes and U–Pb age: Geostandards and Geoanalytical Research, v. 34, p. 117-134, https://doi.org/10.1111/j.1751-908X.2010.00036.x.

Liang, Q., Jing, H., and Gregoire, D.C., 2000, Determination of trace elements in granites by inductively coupled plasma mass spectrometry: Talanta, v. 51, p. 507-513, https://doi.org/10.1016/S0039-9140(99)00318-5.

Liu, Y.S., Gao, S., Hu, Z.C., Gao, C.G., Zong, K.Q., and Wang, D.B., 2009, Continental and Oceanic Crust Recycling-induced Melt–Peridotite Interactions in the Trans-North China Orogen: U–Pb Dating, Hf Isotopes and Trace Elements in Zircons from Mantle Xenoliths: Journal of Petrology, v. 51, p. 537-571, https://doi.org/10.1093/petrology/egp082.

Ludwig, K.R., 2003. Isoplot 3.00: A Geochronological Toolkit for Microsoft Excel. Berkeley Geochronology Center, Berkeley, CA.

Wei, W., Zhao, D.P., Xu, J.D., Zhou, B.G., and Shi, Y.L., 2016, Depth variations of P-wave azimuthal anisotropy beneath Mainland China: Scientific Reports, v. 6, p. 29614, https://doi.org/10.1038/srep29614.

Wu, F.Y., Yang, Y.H., Xie, L.W., Yang, J.H., and Xu, P., 2006, Hf isotopic compositions of the standard zircons and baddeleyites used in U-Pb geochronology: Chemical Geology, v. 234, p. 105-126, https://doi.org/10.1016/j.chemgeo.2006.05.003.

Xie, L.W., Zhang, Y.B., Zhang, H.H., Sun, J.F., and Wu, F.Y., 2008, In situ simultaneous determination of trace elements, U-Pb and Lu-Hf isotopes in zircon and baddeleyite: Chinese Science Bulletin, v. 53, p. 1565-1573, https://doi.org/10.1007/s11434-008-0086-y.

Yang, Q., Xia, X.P., Zhang, W.F., Zhang, Y.Q., Xiong, B.Q., Xu, Y.G., Wang, Q., and Wei, G.J., 2018, An evaluation of precision and accuracy of SIMS oxygen isotope analysis: Solid Earth Sciences, v. 3, p. 81-86, https://doi.org/10.1016/j.sesci.2018.05.001.

Yuan, C., Sun, M., Wilde, S., Xiao, W.J., Xu, Y.G., Long, X.P., and Zhao, G.C., 2010, Post-collisional plutons in the Balikun area, East Chinese Tianshan: Evolving magmatism in response to extension and slab break-off: Lithos, v. 119, p. 269-288, https://doi.org/10.1016/j.lithos.2010.07.004

Supplementary Table 1 LA-ICP-MS zircon U-Pb isotopic dating data for the Kalaqigu diorite and monzogranite at the Chinese Wakhan Corridor, Southern Pamir

	Pb	Th	U	Th/U	$^{207}Pb/^{206}Pb$	$^{207}Pb/^{206}Pb$	$^{207}Pb/^{235}U$	$^{207}Pb/^{235}U$	$^{206}Pb/^{238}U$	$^{206}Pb/^{238}U$	$^{207}Pb/^{206}Pb$	$^{207}Pb/^{206}Pb$	$^{207}Pb/^{235}U$	$^{207}Pb/^{235}U$	$^{206}Pb/^{238}U$	$^{206}Pb/^{238}U$
	ppm	ppm	ppm	Ratio	Ratio	1sigma	Ratio	1sigma	Ratio	1sigma	Age (Ma)	1sigma	Age (Ma)	1sigma	Age (Ma)	1sigma
Diorite (WK1616)																
WK1616-02	45	180	788	0.23	0.04434	0.00447	0.10446	0.01042	0.01712	0.0003	-53	174	101	10	109	2
WK1616-03	53	305	626	0.49	0.04264	0.00574	0.09489	0.01268	0.01617	0.0003	-142	198	92	12	103	2
WK1616-05	77	504	763	0.66	0.05439	0.0047	0.12164	0.01037	0.01625	0.00027	387	163	117	9	104	2
WK1616-06	72	463	753	0.62	0.0416	0.00624	0.09367	0.01392	0.01636	0.00037	-199	207	91	13	105	2
WK1616-07	64	419	748	0.56	0.04897	0.00494	0.10885	0.01086	0.01615	0.00028	146	191	105	10	103	2
WK1616-08	19	114	260	0.44	0.04597	0.01294	0.10719	0.02999	0.01694	0.00056	-4	409	103	28	108	4
WK1616-09	44	340	380	0.89	0.05606	0.00903	0.12551	0.01999	0.01626	0.00042	455	307	120	18	104	3
WK1616-10	82	578	883	0.66	0.04646	0.0043	0.10506	0.00961	0.01642	0.00027	22	171	101	9	105	2
WK1616-11	65	408	822	0.50	0.0468	0.00442	0.10639	0.00994	0.01651	0.00027	39	176	103	9	106	2
WK1616-12	95	674	1021	0.66	0.04363	0.00379	0.10242	0.0088	0.01705	0.00026	-90	153	99	8	109	2
WK1616-14	50	314	601	0.52	0.04152	0.00581	0.09644	0.0134	0.01687	0.00032	-204	200	93	12	108	2
WK1616-15	71	404	954	0.42	0.0507	0.00371	0.11825	0.00854	0.01694	0.00025	227	137	113	8	108	2
WK1616-16	68	478	762	0.63	0.04633	0.00458	0.10418	0.0102	0.01633	0.00027	15	183	101	9	104	2
WK1616-18	69	466	669	0.70	0.04651	0.00525	0.10857	0.01215	0.01695	0.00031	24	207	105	11	108	2
WK1616-21	65	434	801	0.54	0.03941	0.00442	0.09018	0.01003	0.01662	0.00028	-324	193	88	9	106	2
WK1616-22	71	507	714	0.71	0.05342	0.00501	0.12039	0.01116	0.01636	0.00029	347	177	115	10	105	2
WK1616-24	53	342	667	0.51	0.05019	0.0055	0.11453	0.01241	0.01657	0.00031	204	210	110	11	106	2
WK1616-25	37	226	501	0.45	0.03683	0.00785	0.08266	0.01752	0.01629	0.00041	-1	295	81	16	104	3
Monzogranite WK1617																
WK1617-02	77	341	1396	0.24	0.04662	0.00332	0.10803	0.00755	0.01682	0.00026	30	123	104	7	108	2
WK1617-04	63	480	362	1.33	0.05401	0.00901	0.13039	0.02152	0.01753	0.00045	371	319	124	19	112	3
WK1617-05	499	605	604	1.00	0.05999	0.00148	0.83847	0.02002	0.10147	0.00111	603	33	618	11	623	6
WK1617-06	156	109	157	0.69	0.07098	0.00296	1.53662	0.06251	0.15719	0.00231	957	59	945	25	941	13
WK1617-08	300	231	338	0.68	0.07041	0.00212	1.23401	0.03609	0.12725	0.00158	940	40	816	16	772	9
WK1617-09	105	67	118	0.57	0.07361	0.00398	1.6198	0.0857	0.15978	0.00264	1031	80	978	33	956	15
WK1617-10	96	93	143	0.65	0.06346	0.00624	0.96032	0.09252	0.10988	0.00269	724	164	683	48	672	16
WK1617-11	173	189	163	1.16	0.0615	0.00546	0.79957	0.06937	0.09441	0.00222	657	147	597	39	582	13
WK1617-13	36	218	428	0.51	0.04039	0.01007	0.09209	0.02282	0.01656	0.00049	-267	328	89	21	106	3

WK1617-14	509	672	503	1.33	0.05992	0.00175	0.78631	0.0226	0.0953	0.00109	601	42	589	13	587	6
WK1617-16	72	527	383	1.38	0.0498	0.01074	0.11634	0.02487	0.01697	0.00051	186	347	112	23	108	3
WK1617-17	17	112	108	1.03	0.05251	0.04327	0.13531	0.11073	0.01872	0.00183	308	1159	129	99	120	12
WK1617-18	104	52	705	0.07	0.05515	0.00195	0.40354	0.01418	0.05315	0.00059	418	59	344	10	334	4
WK1617-19	500	987	1293	0.76	0.05734	0.00122	0.51134	0.01105	0.06477	0.00061	505	31	419	7	405	4
WK1617-20	57	396	299	1.33	0.06046	0.01558	0.13778	0.03512	0.01655	0.00065	620	457	131	31	106	4
WK1617-21	403	191	511	0.37	0.07364	0.0014	1.77078	0.03497	0.17469	0.00168	1032	25	1035	13	1038	9
WK1617-23	449	320	560	0.57	0.0687	0.00152	1.35344	0.03072	0.14312	0.00146	890	30	869	13	862	8
WK1617-24	326	424	907	0.47	0.05638	0.00187	0.55852	0.01855	0.07197	0.0008	467	54	451	12	448	5
WK1617-25	43	289	307	0.94	0.04322	0.01616	0.10257	0.03813	0.01724	0.00072	-111	514	99	35	110	5

Supplementary Table 2-1 Representative electron probe analyses of amphibole from the Kalaqigu high-Mg diorite

Sample	Locality	Lithology	Spot no.	Comment	SiO_2	TiO_2	Al_2O_3	Cr_2O_3	TFeO	MnO	MgO	CaO	Na_2O	K_2O	Ni	Total	$Mg^{\#}$
WK1616	Kalaqigu	High-Mg diorite	1	core	45.58	1.44	9.30	0.03	14.63	0.28	12.04	11.64	1.16	0.97	0.00	97.06	59
WK1616	Kalaqigu	High-Mg diorite	2	↓	43.97	1.65	10.05	0.06	16.08	0.31	11.33	11.83	1.28	1.32	0.01	97.87	56
WK1616	Kalaqigu	High-Mg diorite	3	rim	43.19	2.08	11.43	0.09	15.35	0.29	10.78	11.48	1.53	1.22	0.05	97.44	56
WK1616	Kalaqigu	High-Mg diorite	4		45.93	1.08	8.45	0.08	15.50	0.29	12.46	11.88	1.07	1.03	0.01	97.76	59
WK1616	Kalaqigu	High-Mg diorite	5	core	48.69	0.87	6.34	0.00	14.29	0.34	13.16	12.15	0.74	0.71	0.00	97.29	62
WK1616	Kalaqigu	High-Mg diorite	6	↓	43.28	1.74	10.51	0.06	16.97	0.27	10.37	11.96	1.16	1.43	0.02	97.77	52
WK1616	Kalaqigu	High-Mg diorite	7	rim	44.32	1.91	10.28	0.04	15.69	0.30	10.75	11.53	1.23	1.03	0.00	97.08	55
WK1616	Kalaqigu	High-Mg diorite	8		47.43	0.85	7.33	0.04	15.42	0.33	12.93	11.63	0.95	0.83	0.00	97.74	60

Struturale formulae is calculated for 23 oxygens with Fe^{2+}/Fe^{3+} estimation assuming ∑15 cations (Leake et al., 1997)

Sample	Si	Al^{IV}	Tsite	Al^{VI}	Ti	Cr^{3+}	Fe^{3+}	Mg	Fe^{2+}	Mn^{2+}	Csite	Fe^{2+}	Mn^{2+}	Ca	Na	Bsite	Na	K	Asite	$Mg/(Mg+Fe^{2+})$	Temperature (℃)	fO_2	△FMQ	Pressure (kbar)	H_2O_{melt} (wt.%)
WK1616	6.77	1.24	8.00	0.39	0.16	0.00	0.16	2.66	1.62	0.00	5.00	0.03	0.04	1.85	0.08	2.00	0.26	0.18	0.44	0.62	847	-12.21	1.22	6.07	6.17
WK1616	6.54	1.46	8.00	0.31	0.19	0.01	0.27	2.51	1.71	0.00	5.00	0.01	0.04	1.89	0.06	2.00	0.31	0.25	0.56	0.59	880	-11.85	0.89	4.66	5.40
WK1616	6.46	1.54	8.00	0.47	0.23	0.01	0.09	2.40	1.79	0.00	5.00	0.04	0.04	1.84	0.09	2.00	0.36	0.23	0.59	0.57	907	-11.71	0.45	7.43	6.60
WK1616	6.77	1.23	8.00	0.24	0.12	0.01	0.37	2.74	1.52	0.00	5.00	0.02	0.04	1.88	0.07	2.00	0.24	0.19	0.43	0.64	834	-12.20	1.54	3.59	5.24
WK1616	7.16	0.84	8.00	0.26	0.10	0.00	0.14	2.89	1.62	0.00	5.00	0.00	0.04	1.91	0.05	2.00	0.17	0.13	0.30	0.64	771	-13.28	1.89	3.86	5.40
WK1616	6.49	1.51	8.00	0.35	0.20	0.01	0.23	2.32	1.90	0.00	5.00	0.00	0.04	1.92	0.04	2.00	0.30	0.27	0.57	0.55	889	-12.01	0.53	5.38	5.82
WK1616	6.64	1.37	8.00	0.45	0.22	0.01	0.09	2.40	1.84	0.00	5.00	0.03	0.04	1.85	0.08	2.00	0.28	0.20	0.47	0.57	869	-12.30	0.64	7.02	6.86
WK1616	6.96	1.04	8.00	0.22	0.09	0.01	0.39	2.83	1.46	0.00	5.00	0.04	0.04	1.83	0.09	2.00	0.18	0.16	0.33	0.66	795	-12.73	1.88	3.26	5.19

TFeO = Total FeO content; $Mg^{\#} = 100*Mg^{2+}/(Mg^{2+} + TFe^{2+})$

Temperature, fO_2 and △FMQ values calculated using the formulations of Ridolfi et al. (2010).

Pressure calculated using an extended calibration of the Larocque and Canil (2010) barometer published by Krawczynski et al. (2012).

H_2O_{melt} (wt.%) calculated using the formulations of Ridolfi et al. (2010).

Supplementary Table 2-2 Representative electron probe analyses of biotite from the Kalaqigu pluton

Sample	Locality	Lithology	Spot no.	Comment	SiO_2	TiO_2	Al_2O_3	Cr_2O_3	TFeO	MnO	MgO	CaO	Na_2O	K_2O	Ni	Total	$Mg^{\#}$
WK1616	Kalaqigu	High-Mg diorite	1	core	45.58	1.44	9.30	0.03	14.63	0.28	12.04	11.64	1.16	0.97	0.00	97.06	59
WK1616	Kalaqigu	High-Mg diorite	2	↓	43.97	1.65	10.05	0.06	16.08	0.31	11.33	11.83	1.28	1.32	0.01	97.87	56
WK1616	Kalaqigu	High-Mg diorite	3	rim	43.19	2.08	11.43	0.09	15.35	0.29	10.78	11.48	1.53	1.22	0.05	97.44	56
WK1616	Kalaqigu	High-Mg diorite	4		45.93	1.08	8.45	0.08	15.50	0.29	12.46	11.88	1.07	1.03	0.01	97.76	59

WK1616	Kalaqigu	High-Mg diorite	5	core	48.69	0.87	6.34	0.00	14.29	0.34	13.16	12.15	0.74	0.71	0.00	97.29	62
WK1616	Kalaqigu	High-Mg diorite	6	↓	43.28	1.74	10.51	0.06	16.97	0.27	10.37	11.96	1.16	1.43	0.02	97.77	52
WK1616	Kalaqigu	High-Mg diorite	7	rim	44.32	1.91	10.28	0.04	15.69	0.30	10.75	11.53	1.23	1.03	0.00	97.08	55
WK1616	Kalaqigu	High-Mg diorite	8		47.43	0.85	7.33	0.04	15.42	0.33	12.93	11.63	0.95	0.83	0.00	97.74	60

Struturale formulae is calculated for 23 oxygens with Fe^{2+}/Fe^{3+} estimation assuming ∑15 cations (Leake et al, 1997)。

Sample	Si	Al^{IV}	Tsite	Al^{VI}	Ti	Cr^{3+}	Fe^{3+}	Mg	Fe^{2+}	Mn^{2+}	Csite	Fe^{2+}	Mn^{2+}	Ca	Na	Bsite	Na	K	Asite	$Mg/(Mg+Fe^{2+})$	Temperature (℃)	fO_2	△FMQ	Pressure (kbar)	H_2O_{melt} (wt.%)
WK1616	6.77	1.24	8.00	0.39	0.16	0.00	0.16	2.66	1.62	0.00	5.00	0.03	0.04	1.85	0.08	2.00	0.26	0.18	0.44	0.62	847	-12.21	1.22	6.07	6.17
WK1616	6.54	1.46	8.00	0.31	0.19	0.01	0.27	2.51	1.71	0.00	5.00	0.01	0.04	1.89	0.06	2.00	0.31	0.25	0.56	0.59	880	-11.85	0.89	4.66	5.40
WK1616	6.46	1.54	8.00	0.47	0.23	0.01	0.09	2.40	1.79	0.00	5.00	0.04	0.04	1.84	0.09	2.00	0.36	0.23	0.59	0.57	907	-11.71	0.45	7.43	6.60
WK1616	6.77	1.23	8.00	0.24	0.12	0.01	0.37	2.74	1.52	0.00	5.00	0.02	0.04	1.88	0.07	2.00	0.24	0.19	0.43	0.64	834	-12.20	1.54	3.59	5.24
WK1616	7.16	0.84	8.00	0.26	0.10	0.00	0.14	2.89	1.62	0.00	5.00	0.00	0.04	1.91	0.05	2.00	0.17	0.13	0.30	0.64	771	-13.28	1.89	3.86	5.40
WK1616	6.49	1.51	8.00	0.35	0.20	0.01	0.23	2.32	1.90	0.00	5.00	0.00	0.04	1.92	0.04	2.00	0.30	0.27	0.57	0.55	889	-12.01	0.53	5.38	5.82
WK1616	6.64	1.37	8.00	0.45	0.22	0.01	0.09	2.40	1.84	0.00	5.00	0.03	0.04	1.85	0.08	2.00	0.28	0.20	0.47	0.57	869	-12.30	0.64	7.02	6.86
WK1616	6.96	1.04	8.00	0.22	0.09	0.01	0.39	2.83	1.46	0.00	5.00	0.04	0.04	1.83	0.09	2.00	0.18	0.16	0.33	0.66	795	-12.73	1.88	3.26	5.19

The Fe^{2+} and Fe^{3+} were calculated using the software of Geokit (Lu et al., 2004).

The crystallization pressures and temperatures of the biotites were estimated using formulations of Li et al. (2022).

Supplementary Table 2-3 Representative electron probe analyses of plagioclase from the Kalaqigu pluton

Sample	Lithology	Spot no.	Comment	SiO_2	TiO_2	Al_2O_3	Cr_2O_3	TFeO	MnO	MgO	CaO	Na_2O	K_2O	Ni	Total	An (mol.%)	Ab (mol.%)	Or (mol.%)
WK1616	High-Mg diorite	1	rim	55.5	0.03	28.3	0.00	0.12	0.00	0.00	10.08	5.39	0.29	0.00	99.7	50	48	2
WK1616	High-Mg diorite	2		48.7	0.00	32.9	0.00	0.09	0.01	0.00	15.1	2.49	0.07	0.01	99.3	77	23	0
WK1616	High-Mg diorite	3	↓	47.8	0.06	33.5	0.03	0.11	0.01	0.02	15.9	2.10	0.06	0.01	99.6	80	19	0
WK1616	High-Mg diorite	4		47.7	0.00	33.4	0.00	0.14	0.00	0.01	15.8	2.18	0.04	0.00	99.4	80	20	0
WK1616	High-Mg diorite	5		48.2	0.00	33.2	0.04	0.08	0.03	0.00	15.74	2.22	0.05	0.01	99.6	79	20	0
WK1616	High-Mg diorite	6	core	47.0	0.00	33.9	0.00	0.12	0.00	0.00	16.77	1.78	0.05	0.00	99.7	84	16	0
WK1616	High-Mg diorite	7		46.9	0.00	33.7	0.00	0.12	0.01	0.00	16.60	1.78	0.05	0.09	99.2	83	16	0
WK1616	High-Mg diorite	8	↓	55.4	0.01	27.9	0.00	0.17	0.02	0.01	11.4	4.34	0.28	0.03	99.5	58	40	2
WK1616	High-Mg diorite	9		56.1	0.00	27.7	0.02	0.11	0.00	0.00	9.5	5.84	0.33	0.00	99.6	47	52	2
WK1616	High-Mg diorite	10	rim	56.3	0.00	27.7	0.03	0.12	0.02	0.02	9.5	5.90	0.33	0.03	99.9	46	52	2
WK1617	Monzogranite	11	core	62.30	0.00	23.26	0.02	0.00	0.00	0.00	5.02	8.28	0.23	0.00	99.1	25	74	1
WK1617	Monzogranite	12	↓	60.21	0.02	24.79	0.00	0.02	0.03	0.00	6.00	7.62	0.32	0.01	99.0	30	68	2
WK1617	Monzogranite	13	rim	60.25	0.00	24.47	0.01	0.00	0.01	0.00	6.93	7.23	0.30	0.02	99.2	34	64	2

WK1617	Monzogranite	14	63.58	0.00	22.35	0.00	0.02	0.00	0.00	4.47	8.51	0.26	0.05	99.2	22	76	2
WK1617	Monzogranite	15	62.59	0.01	22.69	0.00	0.04	0.00	0.00	4.96	8.62	0.25	0.00	99.2	24	75	1

REFERENCES CITED

Krawczynski, M., Grove, T.L., and Behrens, H., 2012, Amphibole stability in primitive arc magmas: effects of temperature, H2O content, and oxygen fugacity: Contributions to Mineralogy and Petrology, v. 164, p. 317-339, https://doi.org/10.1007/s00410-012-0740-x.

Larocque, J., and Canil, D., 2010, The role of amphibole in the evolution of arc magmas and crust: the case from the Jurassic Bonanza arc section, Vancouver Island, Canada: Contributions to Mineralogy and Petrology, v. 159, p. 475-492, https://doi.org/10.1007/s00410-009-0436-z.

Leake, B.E., Woolley, A.R., Arps, C.E.S., Birch, W.D., Gilbert, M.C., Grice, J.D., Hawthorne, F.C., Kato, A., Kisch, H.J., Krivovichev, V.G., Linthout, K., Laird, J., Mandarino, J.A., Maresch, W.V., Nickel, E.H., Rock, N.M.S., Schumacher, J.C., Smith, D.C., Stephenson, N.C.N., Ungaretti, L., Whittaker, E.J.W., and Youzhi, G., 1997, Nomenclature of amphiboles; Report of the Subcommittee on Amphiboles of the International Mineralogical Association, Commission on New Minerals and Mineral Names: American Mineralogist, v. 82, p. 1019-1037.

Li, X., and Zhang, C., 2022, Machine learning thermobarometry for biotite-bearing magmas: Journal of Geophysical Research: Solid Earth, v. 127, p. e2022JB024137, https://doi.org/10.1029/2022JB024137.

Lu, Y.F., 2004, Geokit-A geochemical toolkit for Microsoft Excel: Geochemistry, v. 33, p. 459-464 (in Chinese with English abstract).

Ridolfi, F., Renzulli, A., and Puerini, M., 2010, Stability and chemical equilibrium of amphibole in calc-alkaline magmas: An overview, new thermobarometric formulations and application to subduction-related volcanoes: Contributions to Mineralogy and Petrology, v. 160, p. 45-66, https://doi.org/10.1007/s00410-009-0465-7.

Supplementary Table 3 Major (wt.%), trace (ppm) element compositions and Sr-Nd-Pb isotopic compositions of Kalaqigu diorite and monzogranite at the Chinese Wakhan Corridor and Taxkorgan S-type monzogranites

Sample	WK1616-1	WK1616-2	WK1616-3	WK1616-4	WK1616-5	WK1616-6	WK1617-1	WK1617-2	WK1617-3	WK1617-4	WK1617-5	WK1617-6	AR-1*	AR-2*	AR-3*	AR-4*	PM-7-01**	PM-7-02**	PM-7-03**	PM-7-04**
Location	37°10'16"；75°12'10"						37°10'48"；75°16'09"						37°39'30"；75°08'00"				Taxkorgan pluton			
Rock type	Diorite						Monzogranite						Two-mica monzogranite				Two-mica monzogranite			
Age	105.9±0.3 Ma						108.4±2.4 Ma						110.0±2.4 Ma				118.0±0.9 Ma			
SiO_2	53.36	51.93	52.05	54.48	53.93	52.73	71.58	71.98	71.45	71.11	69.16		72.95	72.67	72.29	69.79	74.58	73.28	72.95	74.23
TiO_2	0.86	0.93	0.87	0.61	0.81	1.10	0.35	0.32	0.29	0.33	0.39		0.17	0.23	0.23	0.42	0.09	0.10	0.09	0.09
Al_2O_3	15.49	14.81	15.12	12.82	15.25	16.76	14.70	15.01	15.13	15.37	16.19		14.63	14.35	14.52	15.23	13.63	14.73	14.84	14.27
$Fe_2O_3^T$	8.74	9.49	9.45	8.92	8.09	8.58	2.06	1.86	1.75	2.16	2.88		1.47	1.88	1.88	2.56	0.81	1.07	1.10	0.80
MnO	0.13	0.15	0.16	0.15	0.11	0.13	0.03	0.02	0.02	0.03	0.04		0.06	0.05	0.05	0.05	0.06	0.05	0.03	0.03
MgO	6.63	7.26	7.22	8.31	6.44	5.43	0.64	0.60	0.58	0.61	0.98		0.35	0.55	0.55	0.78	0.21	0.22	0.28	0.17
CaO	8.66	9.35	8.24	7.91	8.65	7.73	1.91	1.90	1.63	1.90	2.63		1.31	1.61	1.65	1.55	0.79	0.89	0.76	0.88
Na_2O	2.34	2.06	2.29	1.94	2.04	2.36	3.12	3.32	3.30	3.50	4.18		3.65	3.07	3.11	3.18	3.32	3.97	3.58	3.57
K_2O	2.06	2.25	2.22	2.55	2.29	2.99	4.14	3.91	4.42	3.84	2.61		4.15	4.71	4.72	4.54	4.30	3.96	4.64	4.37
P_2O_5	0.28	0.24	0.23	0.17	0.15	0.35	0.12	0.14	0.18	0.23	0.19		0.13	0.14	0.14	0.24	0.14	0.11	0.32	0.12
LOI	1.46	1.51	1.55	1.45	1.72	1.50	0.80	0.71	0.62	0.61	0.73		0.70	0.80	0.75	1.02	1.46	1.08	0.80	0.89
Total	100.01	99.98	99.4	99.31	99.47	99.65	99.46	99.76	99.38	99.69	99.99		99.57	100.07	99.89	99.35	99.38	99.46	99.38	99.41
$Mg^{\#}$	60	60	60	65	61	56	38	39	40	36	40		32	37	37	38	34	29	34	30
A/CNK	0.73	0.67	0.73	0.64	0.72	0.82	1.15	1.17	1.19	1.20	1.16		1.16	1.13	1.13	1.23	1.22	1.21	1.29	1.20
δEu	0.80	0.85	0.77	0.79	0.81	0.88	0.67	0.67	0.78	0.83	0.75		0.40	0.52	0.48	0.50	0.53	0.44	0.62	0.46
Sample	WK1616-1	WK1616-2	WK1616-3	WK1616-4	WK1616-5	WK1616-6	WK1617-1	WK1617-2	WK1617-3	WK1617-4	WK1617-5	WK1617-6	AR-1*	AR-2*	AR-3*	AR-4*	PM-7-01**	PM-7-02**	PM-7-03**	PM-7-04**
Li	33.40	22.90	29.00	21.60	36.70	29.40	47.70	44.70	40.50	57.70	73.60	53.80								
Be	2.56	1.95	2.36	2.12	2.02	1.68	1.39	1.69	2.17	3.41	4.00	1.83								
Sc	29.45	29.37	24.49	25.03	29.66	25.37	4.21	3.90	3.75	3.74	4.22	2.86								
V	189.80	207.96	173.44	139.04	192.04	171.98	15.48	14.02	13.97	11.84	17.69	12.15	7.30	18.40	17.80	26.50				
Cr	117.20	92.14	54.65	87.06	86.43	75.50	2.61	2.53	2.17	2.15	2.87	2.91	5.00	4.40	6.50	10.80				
Co	24.92	27.39	28.98	33.70	24.16	18.58	2.14	1.78	1.68	2.09	2.87	1.93								

Ni	18.17	22.30	22.83	34.61	15.66	7.84	1.18	1.07	0.83	1.47	1.22	1.30	1.90	4.20	2.90	4.70				
Cu	15.00	16.10	11.50	16.30	12.50	14.00	2.89	1.29	1.37	1.34	1.46	1.41								
Zn	85.70	86.00	88.60	82.80	73.40	92.10	130.00	58.90	46.40	61.80	75.00	67.00								
Ga	18.40	16.80	17.70	14.40	16.40	19.40	20.10	20.10	19.30	19.80	20.40	19.70	22.00	19.00	21.00	24.00				
Ge	1.68	1.68	1.64	1.65	1.55	1.55	1.34	1.19	1.30	1.60	1.36	1.31								
Rb	66.20	70.30	82.40	94.00	89.20	108.00	129.00	127.00	136.00	139.00	107.00	130.00	200.00	193.00	192.00	184.00	354.00	291.00	199.00	311.00
Sr	574.00	554.00	485.00	365.00	490.00	607.00	222.00	224.00	226.00	227.00	293.00	205.00	88.00	207.00	190.00	178.00	100.00	99.40	56.00	100.00
Y	24.50	22.70	25.80	20.90	23.10	22.50	9.40	9.10	8.81	10.20	9.83	7.97	12.50	15.80	15.20	9.00	11.65	13.63	9.39	13.42
Zr	80.90	56.30	64.50	71.00	60.00	101.00	124.00	118.00	115.00	109.00	145.00	129.00	47.00	88.00	122.00	231.00	37.74	48.46	38.42	31.45
Nb	10.21	9.68	9.30	7.31	8.09	13.31	8.24	7.94	7.64	13.16	12.71	9.53	20.00	18.00	20.30	21.10	16.91	17.13	11.54	14.87
Cs	1.72	1.93	3.61	2.51	3.37	3.86	2.52	2.48	2.66	2.67	3.23	2.86								
Ba	726.00	602.00	530.00	413.00	648.00	886.00	689.00	662.00	870.00	778.00	518.00	772.00	93.00	412.00	384.00	583.00	147.00	118.00	232.00	130.00
La	25.50	23.70	22.80	23.70	20.00	31.80	41.20	39.90	38.30	32.80	45.30	36.90	13.00	22.00	25.00	54.00	9.59	9.90	5.91	9.57
Ce	60.10	54.60	52.50	49.10	43.40	67.60	82.90	79.70	76.20	66.90	89.20	76.50	25.00	39.00	51.00	96.00	17.44	18.09	10.85	17.79
Pr	7.33	6.67	6.36	5.55	5.38	7.78	8.93	8.50	8.30	7.37	9.70	8.17	3.10	4.80	5.90	13.40	2.17	2.26	1.37	2.23
Nd	29.40	27.40	26.40	22.10	23.50	31.00	32.90	31.20	30.60	27.50	36.50	31.00	11.00	17.00	21.00	44.00	7.51	7.93	5.62	7.70
Sm	6.06	5.66	5.80	4.44	5.37	6.23	5.79	5.37	5.32	5.13	6.45	5.69	2.29	3.61	4.20	7.59	1.99	2.17	1.91	2.16
Eu	1.51	1.48	1.39	1.11	1.35	1.65	1.06	1.01	1.13	1.20	1.36	1.07	0.29	0.57	0.59	0.95	0.31	0.28	0.37	0.29
Gd	5.41	4.99	5.31	4.11	4.86	5.30	3.97	3.87	3.66	3.79	4.78	3.80	2.16	3.08	3.43	4.46	1.58	1.74	1.77	1.72
Tb	0.81	0.79	0.81	0.63	0.83	0.81	0.53	0.55	0.47	0.57	0.61	0.50	0.38	0.51	0.51	0.45	0.34	0.39	0.42	0.40
Dy	4.63	4.28	4.71	3.62	4.47	4.35	2.19	2.12	1.98	2.22	2.35	1.90	2.37	3.03	2.87	2.18	2.10	2.25	2.11	2.26
Ho	0.89	0.80	0.92	0.71	0.85	0.81	0.32	0.31	0.25	0.34	0.33	0.26	0.43	0.58	0.53	0.33	0.40	0.47	0.34	0.47
Er	2.51	2.31	2.64	2.16	2.35	2.26	0.75	0.79	0.73	0.75	0.81	0.65	1.25	1.63	1.44	0.83	1.06	1.31	0.68	1.27
Tm	0.35	0.33	0.38	0.31	0.32	0.33	0.08	0.09	0.09	0.09	0.09	0.08	0.20	0.27	0.23	0.12	0.21	0.26	0.11	0.26
Yb	2.21	2.00	2.54	2.03	1.95	1.89	0.50	0.53	0.58	0.57	0.55	0.44	1.29	1.60	1.46	0.83	1.27	1.71	0.53	1.62
Lu	0.32	0.30	0.37	0.28	0.26	0.28	0.06	0.06	0.06	0.07	0.07	0.05	0.17	0.23	0.20	0.11	0.18	0.25	0.08	0.23
Hf	2.60	2.07	2.14	2.42	2.23	2.51	3.27	3.30	3.19	3.13	4.02	3.70	1.52	2.76	3.43	6.16	2.06	1.90	1.79	1.58
Ta	0.72	0.71	0.69	0.82	0.60	0.74	0.63	0.58	0.71	1.57	1.07	0.89	2.16	1.92	2.29	3.08	4.74	1.92	1.96	1.66
Pb	9.98	7.98	7.57	8.50	8.96	8.82	28.60	27.80	30.40	26.90	20.80	27.00	26.00	33.00	32.00	32.00	26.52	25.15	22.44	28.57
Th	5.34	4.60	4.15	6.35	12.70	5.31	12.70	12.10	11.60	10.20	13.90	12.30	8.90	14.20	17.00	35.20	6.90	7.32	1.44	6.95
U	1.23	1.25	0.98	2.78	2.08	0.87	2.32	2.29	2.37	2.52	2.70	2.54	1.80	18.10	3.20	3.60	1.63	2.77	1.41	2.89
T_{Zr} (℃)	536	489	524	512	521	581	769	767	771	761	767	824	697	741	768	829				

$^{87}Rb/^{86}Sr$	0.3334	0.3669	1.6800	1.6392	6.5660	2.6980	2.9190	2.9890
$(^{87}Sr/^{86}Sr)_i$	0.708590	0.707473	0.715400	0.715753	0.709260	0.708640	0.714350	0.707530
$^{147}Sm/^{144}Nd$	0.1245	0.1248	0.1063	0.1040	0.1288	0.1298	0.1229	0.1047
$^{143}Nd/^{144}Nd$	0.512220	0.512282	0.511936	0.511942	0.512109	0.512099	0.511901	0.512083
$\varepsilon_{Nd}(t)$	-7.18	-5.97	-12.45	-12.30	-9.40	-9.60	-13.30	-9.50
T_{Nd_DM} (Ma)	1592	1491	1724	1679				
$T^2_{Nd\_DM}$ (Ma)	1491	1393	1921	1909				
$(^{206}Pb/^{204}Pb)_i$	18.4337	18.3246	18.5056	18.4918				
$(^{207}Pb/^{204}Pb)_i$	15.6938	15.6853	15.7495	15.7481				
$(^{208}Pb/^{204}Pb)_i$	38.7664	38.6378	38.8710	38.8572				

* is from Jiang et al. (2014).

** is from Li et al. (2019).

The zircon saturation temperatures (T_{Zr}) were estimated using thermobarometers from Watson and Harrison. (1983).

REFERENCES CITED

Jiang, Y.H., Liu, Z., Jia, R.Y., Liao, S.Y., Zhao, P., and Zhou, Q., 2014, Origin of Early Cretaceous high-K calc-alkaline granitoids, western Tibet: implications for the evolution of the Tethys in NW China: International Geology Review, v. 56, p. 88-103, https://doi.org/10.1080/01431161.2013.819963.

Li, R.H., Peng, B., Zhao, C.S., Yu, M., Song, L.S., and Zhang, H., 2019, Origin of Early Creceouscalc-alkaline granite, Taxkorgan: Implications for evolution of Tethys evolution in central Pamir: Journal of Central South University, v. 26, p. 3470-3487, https://doi.org/10.1007/s11771-019-4267-4.

Watson, E.B., and Harrison, T.M., 1983, Zircon saturation revisited: temperature and composition effects in a variety of crustal magma types: Earth and Planetary Science Letters, v. 64, p. 295-304, https://doi.org/10.1016/0012-821X(83)90211-X.

Supplementary Table 4 Lu-Hf isotopic compositions of Kalaqigu diorite at the Chinese Wakhan Corridor, Southern Pamir

Sample	Age (Ma)	$^{176}Yb/^{177}Hf$	$^{176}Lu/^{177}Hf$	2σ	$^{176}Hf/^{177}Hf$	2σ	ε_{Hf}	$f_{Lu/Hf}$	T_{HfDM1}	T_{HfDM2}
Diorite (WK1616)										
WK1616-01	105.9	0.014094	0.000652	0.000003	0.282428	0.000016	-9.9	-0.98	1154	1791
WK1616-02	105.9	0.014484	0.000600	0.000003	0.282363	0.000014	-12.2	-0.98	1243	1934
WK1616-03	105.9	0.017451	0.000783	0.000003	0.282420	0.000027	-10.2	-0.98	1168	1807
WK1616-04	105.9	0.020054	0.000888	0.000024	0.282415	0.000016	-10.4	-0.97	1180	1820
WK1616-05	105.9	0.018204	0.000820	0.000005	0.282403	0.000016	-10.8	-0.98	1193	1845
WK1616-06	105.9	0.024250	0.001046	0.000008	0.282412	0.000016	-10.5	-0.97	1189	1828
WK1616-07	105.9	0.026881	0.001083	0.000003	0.282395	0.000016	-11.1	-0.97	1213	1864
WK1616-08	105.9	0.018689	0.000734	0.000012	0.282378	0.000015	-11.7	-0.98	1226	1901
WK1616-09	105.9	0.011516	0.000498	0.000008	0.282411	0.000017	-10.5	-0.99	1173	1827
WK1616-10	105.9	0.018273	0.000830	0.000004	0.282417	0.000016	-10.3	-0.98	1174	1814
WK1616-11	105.9	0.018392	0.000835	0.000006	0.282403	0.000015	-10.8	-0.97	1194	1845
WK1616-12	105.9	0.020144	0.000906	0.000004	0.282405	0.000015	-10.7	-0.97	1194	1842
WK1616-13	105.9	0.019794	0.000907	0.000006	0.282398	0.000017	-11.0	-0.97	1204	1858
WK1616-14	105.9	0.018751	0.000810	0.000006	0.282367	0.000014	-12.1	-0.98	1243	1925
WK1616-15	105.9	0.022458	0.000950	0.000015	0.282415	0.000016	-10.4	-0.97	1181	1820
WK1616-16	105.9	0.022262	0.001012	0.000007	0.282387	0.000018	-11.4	-0.97	1222	1882

Supplementary Table 5 Zircon O isotopic compositions of Kalaqigu diorite and monzogranite at the Chinese Wakhan Corridor, Southern Pamir

Analysis spot	Age (Ma)	Intensity O^{16}	O^{18}/O^{16} Mean	$\delta^{18}O$ (‰)	2σ
Diorite (WK1616)					
WK1616-01		979518000	0.002055	8.03	0.38
WK1616-03	103	986419500	0.002055	7.91	0.43
WK1616-04		975533400	0.002055	8.13	0.15
WK1616-05	104	976108100	0.002055	8.14	0.51
WK1616-06	105	983103700	0.002054	7.49	0.46
WK1616-07	103	983825500	0.002056	8.32	0.35
WK1616-09	104	967447600	0.002055	8.08	0.47
WK1616-10	105	952977200	0.002056	8.23	0.30
WK1616-11	106	987485400	0.002056	8.30	0.47
WK1616-12	109	969187100	0.002056	8.24	0.31
WK1616-14	108	962150800	0.002055	8.13	0.34
WK1616-15	108	942879200	0.002057	9.01	0.37
Monzogranite (WK1617)					
WK1617-01		1523824000	0.002032	8.85	0.25
WK1617-02	108	1543593000	0.002030	8.00	0.17
WK1617-03		1549577000	0.002031	8.47	0.25
WK1617-04	112	1554741000	0.002031	8.25	0.25
WK1617-05	623	1565975000	0.002031	8.31	0.25
WK1617-06	941	1569459000	0.002030	7.97	0.24
WK1617-07		1571741000	0.002030	7.90	0.20
WK1617-08	772	1566809000	0.002030	7.99	0.23
WK1617-09	956	1576714000	0.002031	8.49	0.27
WK1617-10	672	1578725000	0.002030	7.82	0.23